A Study of Multiscale Processes in Near-Global Aquaplanet Cloud-Resolving Models: From Shallow Cumulus Cloud Feedbacks to Tropical Cyclogenesis Predictability

Pornampai Narenpitak

A dissertation
submitted in partial fulfillment of the
requirements for the degree of

Doctor of Philosophy

University of Washington

2019

Reading Committee:

Christopher S. Bretherton, Chair

Shuyi S. Chen

Dale R. Durran

Dargan M. W. Frierson

Program Authorized to Offer Degree:
Atmospheric Sciences

University of Washington

Abstract

A Study of Multiscale Processes in Near-Global Aquaplanet Cloud-Resolving Models: From Shallow Cumulus Cloud Feedbacks to Tropical Cyclogenesis Predictability

Pornampai Narenpitak

Chair of the Supervisory Committee:
Professor Christopher S. Bretherton
Department of Atmospheric Sciences

A near-global aquaplanet cloud-resolving models (NGAqua) has been used to study the responses of clouds and circulations to 4 K sea-surface temperature (SST) warming, CO_2 quadrupling, and both combined. NGAqua spans a large tropical channel domain, with 4 km horizontal resolution, latitudinally dependent SST, and no cumulus parameterization. Prior work showed that its coarsely-resolved shallow cumulus increases with warming. It was suggested that with warmer SST, the moister boundary layer is destabilized by more clear-sky radiative cooling, driving more cumulus convection.

Limited-area cloud-resolving model (CRM) simulations are used to reproduce and understand negative subtropical shallow cumulus cloud feedbacks in NGAqua. A small doubly-periodic version of the same CRM is configured to analyze this low cloud increase in a simpler context. It is driven by steady thermodynamic and advective forcing profiles averaged over the driest subtropical column humidity quartile of NGAqua. Sensitivity studies separate effects of radiative cooling and free-tropospheric relative humidity changes from other aspects of NGAqua's warmer climate. Enhanced clear-sky radiative cooling explains most of the cloud increase due to SST warming, regardless of CRM model resolution and advection scheme. Furthermore, the analysis of the BL liquid virtual static energy suggests that if shallow cumulus clouds were deeper and rained more, warmer SST may result in increased

precipitation rather than increased cloud cover.

Topical cyclogenesis is a multiscale process that involves interactions between large-scale circulations and small-scale tropical convection. NGAqua simulations can produce tropical cyclones (TCs) when the SST distribution is shifted northward such that its maximum is off-equatorial. In this case, the TCs spin up spontaneously from the northern edge of the Intertropical Convergence Zone (ITCZ). The large-scale flows provide necessary conditions for barotropic instability and predetermine where the pre-TC vortices will be found. The predictability of this process is up to ten days. The ITCZ is also a rich source for atmospheric column-integrated moisture, which is important of the growth of tropical convection, a process that is less predictable. A Lagrangian-framework analysis shows that vertical stretching of absolute vorticity associated with moist convective updrafts contributes positively to the absolute vorticity tendency of a TC. A compositing analysis suggests that the vorticity stretching is crucial for the spin up. But pre-TC vortices do not develop into TCs if they are situated over regions of strong horizontal moisture gradients, because the vertical stretching does not align with the centers of the cyclonic vorticity anomalies.

TABLE OF CONTENTS

LIST OF FIGURES

LIST OF TABLES

GLOSSARY

LASAM: Limited-area SAM

NGAqua: Near-global aquaplanet cloud-resolving model

SAM: System of Atmospheric Modeling

TC: Tropical cyclone

TCG: Tropical cyclogenesis

s_{vl}: Liquid virtual static energy ($s_{vl} = s_l + 0.61 c_p T_{\mathrm{ref}} q_t$)

$\Delta \mathrm{R}_{\mathrm{clr}}$: Enhanced boundary-layer clear-sky radiative cooling

η_{850}: Absolute vorticity at 850 hPa

ACKNOWLEDGMENTS

I would like to express sincere appreciation to those who have supported and assisted me during the time of my graduate study at the University of Washington. First and foremost, I would like to express my deepest gratitude to my advisor, Professor Christopher S. Bretherton, for his continuous support and guidance both in atmospheric sciences and beyond. I am especially grateful for his understanding and care when I had to work at a slower pace because of hand injuries. I also would like to thank my Ph.D. Thesis Reading Committee, Professor Shuyi S. Chen, Professor Dale R. Durran, and Professor Dargan M. W. Frierson; and the Graduate School Representative (GSR), Professor Alison R. Gray.

In addition, I would like to thank Dr. Peter N. Blossey and Dr. Matthew C. Wyant for their guidance in running simulations using SAM and modifying the code for various tests. I would like to thank Professor Marat F. Khairoutdinov, our collaborator from Stony Brook University, for running and providing the outputs from the near-global aquaplanet (NGAqua) simulations. I would like to express a sincere gratitude toward Professor Stephen Warren, for his scientific writing class has been highly helpful for my thesis and paper writing.

I am truly thankful for all of the staff at the Department of Atmospheric Sciences, especially Erica Coleman, our department's Academic Advisor; Hettie Scofield, the current Administrator; and everybody else who keeps the department running. I would also like to thank Marc L. Michelsen for maintaining the Olympus Supercomputer at the Department of Atmospheric Sciences, and for his technical supports on computing and storing data on the computer cluster.

The research projects were made possible by funding from the Department of Energy

[grant DE-SC0012451] and by a scholarship from Thailand's Ministry of Science and Technology. Fundings for performing the NGAqua simulations were from the NSF Science and Technology Center for Multi-Scale Modeling of Atmospheric Processes (CMMAP) [grant ATM-0425247] and the Extreme Science and Engineering Discovery Environment (XSEDE) [grant OCI-1053575]. The NGAqua simulations were performed at the NCAR-Wyoming Supercomputer Center on the Yellowstone Supercomputer.

Finally, I would like to thank all of my family and friends in Thailand, Seattle, and elsewhere; your encouragements and confidence in me to be successful have been invaluable. I would like to express my deepest gratitudes to my parents Surapong and Aphaphan, and my younger brother Kamin, who have been supportive of my studies in the United States, and encouraged me during challenging times. Special thanks to my cohorts, especially Isabel McCoy and Kuan-Ting O. Many thanks to my Seattleite friends, especially Dhayoung Yoon, Kris Brillantes, and Tom and Linda Ackerman. I am truly grateful for everybody who has been part of my professional and personal growth during these past five years in Seattle.

Chapter 1

INTRODUCTION

A near-global tropical-channel aquaplanet cloud-resolving model (CRM) called NGAqua has been used to study atmospheric circulations, precipitation, and clouds [11, 39]. NGAqua uses the System of Atmospheric Modeling (SAM) [30] and does not rely on convective parameterizations. It has 4 km horizontal resolution and 34 vertical levels, spanning 20,480 x 10,240 km^2. The domain is zonally periodic but has northern and southern boundaries. NGAqua has latitudinally dependent Coriolis parameter and sea-surface temperature (SST). The latitudes in these simulations range from 46°S to 46°N. With a realistic SST distribution specified to be maximum at the equator, NGAqua produces realistic tropical convection and large-scale circulations, but does not produce tropical cyclones (TCs).

In my previous research, I studied cloud and circulation feedbacks to +4K SST warming and quadrupling of CO_2 (4xCO2) using NGAqua [39]. NGAqua were initially performed by Professor Marat Khairoutdinov, at Stony Brook University, under with scientific guidance of my advisor, Professor Christopher Betherton. NGAqua's low-latitude cloud response to 4xCO2 is minimal. With +4K SST warming, NGAqua produces an unexpected increase in subtropical shallow cumulus cloud fraction with warmer SST, in contrast to many global climate models, although the overall feedback of low clouds on global warming is positive due to decreased cloud fraction on the equatorward side of the midlatitude storm tracks.

This surprising result inspired the fist part of this thesis, which is adapted from a paper that I wrote with Professor Bretherton and was recently published [38]. We use the limited-area version of SAM (LASAM) with the same resolution and model configuration as NGAqua but a small doubly-periodic domain. Our goal has been to represent shallow cumulus cloud and boundary-layer (BL) turbulence in the subtropics of NGAqua by prescribing LASAM

with large-scale forcings derived from the NGAqua subtropics, where shallow cumulus is the dominant cloud regime. How LASAM simulations are configured will be discussed in Chapter 2. Further, it will be shown using additional LASAM simulations that, enhanced clear-sky radiative cooling of moister BL under dry free troposphere destabilizes the cloud layer and drives more shallow cumuli. The response of shallow cumulus to enhanced BL clear-sky radiative cooling is robust across all model configurations.

In Chapter 3, NGAqua is used to study tropical cyclogenesis and its predictability. The NGAqua simulations used were also performed by Professor Khairoutdinov. TC predictability has long been challenging in terms of genesis, intensification, and track prediction. The nonlinearity of the system, involving vortex merging, BL moisture sensitivity and tropical convection adds to the forecast complexity. NGAqua is a perfect tool for this because, unlike rotating radiative-convective equilibrium simulations that use limited- or square-domain CRMs with a fixed SST, NGAqua provides a global framework for which the SST and planetary vorticity vary realistically. Furthermore, unlike conventional general circulation models, NGAqua has sufficiently fine resolution to explicitly resolve the tropical convective cloud systems without having to rely on any cumulus parameterizations. With suitable environmental conditions, TCs form spontaneously in NGAqua and are allowed to interact with an Earth-like climate. A Japanese global cloud resolving model, Nonhydrostatic ICosahedral Atmospheric Model (NICAM), with realistic geography, has also been used to simulate specific tropical cyclones [24]. However, the aquaplanet idealization in NGAqua helps focus attention on the genesis problem rather than complicated interactions between TCs and the continental landmasses which often occur during the later stages of the storms and are less relevant to the genesis problem.

This study explores the role of humidity, convective instability and vorticity in the development of TCs using NGAqua. We use a 20-day NGAqua simulation with the domain centered at 15°N, from 31°S to 61°N, and the similar SST pattern but shifted northward, as in the autumn equinox of the East Pacific. Numerous TCs develop spontaneously out of a positive vorticity band north of the Intertropical Convergence Zone (ITCZ). Two sen-

sitivity simulations add small-amplitude white noise perturbations to the moisture field at a single model level, allowing a crude assessment of the intrinsic predictability of tropical cyclogenesis.

Chapter 2

UNDERSTANDING NEGATIVE SUBTROPICAL SHALLOW CUMULUS CLOUD FEEDBACKS IN A NEAR-GLOBAL AQUAPLANET MODEL USING LIMITED-AREA CLOUD-RESOLVING SIMULATIONS

2.1 Introduction

Shallow cumulus cloud response to global warming continues to be a leading source of uncertainty in estimating climate sensitivity. Even though the majority of state-of-the-art global climate models (GCMs) simulate a reduction in cloud fraction of shallow cumuli in a warmer climate, resulting in a positive shortwave feedback, they still disagree on the magnitude of this effect, reflecting the challenge in representing marine boundary-layer low cloud in a coarse-resolution GCM [4, 5, 64, 65]. Studies using limited-area cloud-resolving model (CRM) simulations of marine shallow cumulus also give a range of results, depending on the idealizations made. Large-eddy simulations (LES) of marine shallow cumulus mostly support the GCM consensus that in this cloud regime, increased sea surface temperature (SST) leads to a slight reduction in low cloud fraction [47, 48, 3, 7, 55, 56]. The response was consistent across different LES models that participated in the CFMIP-GASS Intercomparison of Large eddy models and Single column models (CGILS), for which the large-scale control and perturbed-climate forcings were identical between the models [3]. A further study on the relative importance of the difference climate change forcings for this low cloud reduction was examined [9]. In the CGILS shallow cumulus case S6, the warming of the atmosphere-ocean column was found to be the most important driver of the shallow cumulus reduction, compensated by increased estimated inversion stability (EIS) [61], with the direct radiative effect of CO_2 increase being negligible.

However, some studies using global or near-global frameworks based on coarse-grid cloud-resolving models (CRMs) have simulated a slight increase of low cloud cover over the subtropical oceans. In these CRM studies, the subtropical-mean forcings can freely respond to the large-scale dynamics as the SST warms. Wyant et al. (2009) used superparameterization with 4 km horizontal resolution and 32 vertical levels [62], and Narenpitak et al. (2017) used a near-global aquaplanet CRM called NGAqua with similar grid resolution [39]. Both studies hypothesized that in a warmer climate, increased clear-sky radiative cooling can destabilize the subtropical shallow cumulus boundary layer and stir up more cloud. Parishani et al. (2017, 2018) used ultraparameterization (a limited-area fine-resolution CRM of $250\times250\times20$ m grid spacing in each grid column of a GCM) in place of standard superparameterization, whose CRMs use 4 km horizontal grid spacing and 100-200 m grid spacing in the lowest 2 km of the atmosphere [44, 43]. Like superparameterization, ultraparameterization predicts slight increases in cloud cover in a warmer climate in pure trade cumulus regimes such as over the central Pacific Ocean just south of the Equator. However, the cloud increase is smaller with ultraparameterization.

The CRM used in all of these studies (the System for Atmospheric Modeling or SAM) also simulated shallow cumulus decreases in the aforementioned LES studies. This is not a contradiction, since the LES studies used different large-scale forcings as well as a much finer grid. Nevertheless, it does bring up a key issue with limited-area simulations to be addressed in this chapter: How representative of shallow cumulus feedbacks over the entire subtropical ocean are they? With one or a few carefully configured limited-area simulations, could the subtropical marine low cloud feedbacks of a global cloud-resolving model be accurately predicted and the dominant physical mechanisms understood? And if so, how robust are the cloud responses to model configuration and grid resolution?

This problem was tackled by Blossey et al. (2009), who used a limited-area CRM to study the negative subtropical low cloud feedbacks in the superparameterized GCM analyzed by Wyant et al. (2009) [2, 62]. Wyant et al. (2009) sorted the ocean regions of the low latitudes into climate regimes using binning by percentiles of monthly-mean lower tropospheric sta-

bility [62]. Steady large-scale forcings were derived by bin-averaging for two representative climate regimes in the subsiding branch of the Hadley circulation in which shallow cumulus is prevalent. Applying these forcing to a CRM configured identically to those embedded in its parent superparameterized GCM, Blossey et al. (2009) were able to approximately replicate the vertical profiles of boundary-layer cloud in a control climate and its increase in response to a globally uniform 2 K SST warming seen within these two regimes in the superparameterized GCM [2]. They further showed that similarly-forced simulations with finer LES-like grid resolution produced less cloud in the control climate and correspondingly less cloud increase in the warmer climate.

This part of the thesis is adapted from Narenpitak and Bretherton (2019), a recently published paper written my advisor and me [38]. We use a similar approach with some novel twists to study why subtropical shallow cumulus increases in a warmer climate in NGAqua, which covers a large tropical channel extending from 46°S to 46°N with a 4 km horizontal grid spacing [11, 39]. The channel has a zonally-symmetric SST maximum at the equator. NGAqua simulates clouds and circulations from the grid scale to global scale without a cumulus parameterization that might unintentionally build in assumptions that could affect its cloud feedbacks. The grid spacing used in the NGAqua simulations is too coarse to properly resolve shallow cumulus convection. However, it is representative of global cloud-resolving models that are now becoming more popular for examining cloud feedbacks [35, 52]. So it is of interest to understand shallow cumulus convection in NGAqua and its response to climate perturbations in a limited-area modeling framework that also allows sensitivity studies to finer grids and perturbed physics.

2.2 Mechanisms That Might Affect the Shallow Cumulus Cloud Responses

For context, we summarize some mechanisms proposed in past studies through which shallow oceanic cumuli could respond to a warming climate. One negative feedback mechanism is liquid water adiabatic lapse rate or optical depth feedback, which derives from a larger moist-adiabatic rate of liquid water increase with height at a warmer temperature. This makes an

adiabatic cloud of a given thickness have a higher liquid water path and be more reflective in a warmer climate [42, 51]; however, due to lateral entrainment mixing and precipitation processes, shallow cumulus clouds tend to be far from adiabatic [57].

A proposed positive feedback mechanism that can offset the negative feedback discussed above is the surface-flux desiccation feedback [47, 56]. As the climate warms, latent heat flux increases, bringing more moisture to the boundary layer, but at the same time causes more vigorous cumuli that deepen and dry the boundary layer through penetrative entrainment. A counterargument is that GCMs don't tend to deepen low-latitude shallow cumulus-capped marine boundary-layers in a warmer climate [15] despite weakened mean subsidence [34], suggesting reduced, not enhanced, penetrative entrainment. In low latitudes, the moist-adiabatically induced increase in free-tropospheric dry static stability in a warmer climate may also oppose boundary layer deepening.

Another factor that controls the cloud amount and the boundary-layer depth is free-tropospheric relative humidity (RH) [32, 6, 31, 9, 22]. Given the same penetrative entrainment rate, drier air at the level immediately above the inversion causes more entrainment drying, depleting the boundary-layer cloud water. On the other hand, drying of the free-tropospheric column also increases boundary-layer radiative cooling. The enhanced radiative cooling destabilizes the boundary layer and increases cumulus convection, which entrains free-tropospheric air and deepens the boundary layer.

Precipitation may also affect shallow cumulus response to SST warming. This effect is allowed in NGAqua, but the bulk of the simulated subtropical cumuli are too shallow to form much rain. LES studies suggest that for slightly deeper or more aerosol-depleted cumuli which precipitate more efficiently, a warmer climate favors increased precipitation from shallow cumuli that depletes updraft liquid water; mesoscale aggregation of the cumuli can enhance this process by accelerating rain onset [56, 8]. This limits penetrative entrainment and boundary-layer depth, resulting in a slight decrease in low cloud fraction, both with a fixed radiative cooling rate [56] and even with interactive radiative cooling [3].

Our control and increased-SST model configurations and large-scale forcings are like

NGAqua but on much smaller domains: They are described in section 2.3. Section 2.4 presents the results, including sensitivity to SST warming and imposed changes in clear-sky radiative cooling profile and free-tropospheric RH that correspond to the climate perturbation. Section 2.5 presents sensitivity studies to domain size (which can affect self-aggregation of shallow cumulus), advection scheme, and grid resolution. Section 2.6 uses a boundary-layer heat budget to compare the impacts of radiative cooling and SST warming on the cloud properties, and to discuss different measures of shallow cumulus inversion stability and their sensitivity to SST warming. Section 2.7 presents conclusions.

2.3 Model Configurations

The near-global aquaplanet cloud-resolving model (NGAqua) and the limited area CRM with which we are comparing (which we call LASAM) are based on the System of Atmospheric Modeling (SAM) [30].

NGAqua was first described by Bretherton and Khairoutdinov (2015) and Narenpitak et al. (2017). [11, 39]. It uses 4-km horizontal resolution spanning a 20,480 km x 10,240 km zonally-symmetric tropical channel with free slip rigid walls at meridional boundaries at 46°S/N. NGAqua has 34 vertical levels variably spaced up to 27 km; there are 11 levels below 2 km, shown using short horizontal black lines in Figure 2.1e. The model has latitudinally dependent Coriolis parameter and a hemispherically-symmetric SST with a maximum on the equator. For the simulations referred to in this chapter, the CO_2 concentration is 350 ppm, as in the APE experiments. NGAqua uses a 1-moment microphysics scheme [30], the Community Atmospheric Model 3 (CAM3) radiation scheme [17], the multidimensional positive definite advection transport algorithm (MPDATA) scalar advection scheme [50], and a prognostic subgrid turbulent kinetic energy scheme. Narenpitak et al. (2017) assessed low cloud feedbacks in NGAqua by comparing a control simulation with a '4K' simulation in which SST is uniformly increased by 4 K [39].

LASAM uses version 6.10 of the System of Atmospheric Modeling (SAM) [30] configured (including all physics parameterizations) as for NGAqua. Unless otherwise noted, the ver-

tical and horizontal grid resolution and the advection scheme are identical to NGAqua. By default, LASAM is run on a small 64 km × 64 km (16 × 16 grid columns) doubly-periodic domain, using large-scale horizontal advective forcing, large-scale vertical velocity, and other boundary conditions from the control or 4K NGAqua simulations averaged over selected parts of the NGAqua subtropics (11.5-23°N/S).

We originally ran LASAM on a 256 km × 256 km domain. As discussed in detail in Section 2.5.1, with this larger domain size the simulated shallow cumuli often self-aggregate into bands within 10–50 days. While NGAqua also shows some mesoscale organization of shallow cumulus, it does not look all that similar to these simulations and does not have the same sensitivity to SST. This makes a comparison of aggregated LASAM cloud statistics and low cloud feedbacks with NGAqua less compelling. Before aggregation, the cloud properties of the shallow cumuli in LASAM are not sensitive to the domain size. Hence, we base this paper on the 64 km × 64 km simulations, which are too small to aggregate.

Using outputs saved from the NGAqua simulations, we compute time-dependent vertical profiles of horizontal advective forcings and vertical motion for all mesoscale (160 km × 160 km) blocks for each 3-hour segment of our 80 day simulations, and average them into daily means. LASAM can be configured to use time-varying advective forcing derived from a particular mesoscale block of NGAqua. We have checked that, in that case, LASAM can approximately replicate the evolution of the time-varying block-average statistics from NGAqua, including the diurnal cycle. However, the 80-day mean cloud statistics, even when averaged across ten or more randomly-chosen mesoscale blocks, contain too much sampling noise to be fully representative of the subtropical mean and hence to be useful for assessing subtropical-mean low cloud feedbacks. In this chapter, we instead focus on LASAM simulations with steady forcings and diurnally-averaged insolation and their sensitivity to imposed climate changes.

2.3.1 Subtropical CRH-quartile binned NGAqua results

Figure 12 of Narenpitak et al. (2017) showed that with 4 K SST warming, NGAqua's shallow cumulus cloud fraction robustly increases across the entire subtropics, despite occasional high clouds associated with the Intertropical Convergence Zone (ITCZ) and mid-latitude cyclones [39]. Thus we originally ran LASAM using steady forcings derived from the 80-day subtropical mean of the NGAqua control and 4K simulations. However, these simulations produced deep cumulus instead of shallow cumulus, because even the relatively small amount of subtropical-mean latent heating associated with deep clouds substantially perturbs the balance between large-scale advection and radiative cooling, which LASAM would have to maintain to simulate only shallow cumulus convection.

To avoid this problem, we categorize the NGAqua subtropics into four weather regimes which are separately simulated with steadily-forced LASAM simulations. This is analogous to Blossey et al. (2009)'s percentile binning by monthly-mean lower tropospheric stability, but the zonal symmetry of SST in NGAqua means that there is little variability in monthly-mean lower tropospheric stability across its subtropics [2]. Indeed, lower tropospheric stability is not the most effective parameter for discriminating precipitating weather regimes with some deeper cumulus convection from largely nonprecipitating shallow cumulus regimes, even on daily time scales. Instead, following Bretherton et al. (2004), we calculate the daily-mean column relative humidity (CRH), the ratio of precipitable water to saturated water vapor path, averaged over mesoscale blocks of 160 km $\times$ 160 km [12]. We bin the daily block-averages into four quartiles of CRH, which prove sufficient to separate deep convection into the moistest quartile, and nearly nonprecipitating shallow cumulus convection in the driest quartiles. Each day, the mesoscale blocks comprising each quartile are in different locations, responding to passing weather systems. We find that CRH is a better discriminator than 500-hPa vertical velocity (W500) of regions of mid- and upper-tropospheric cloud and precipitation. Compared to W500 quartiles, the CRH quartiles support more consistent cloud regimes with less intra-quartile variability in precipitation and cloud condensate (not

shown).

The two lowest CRH quartiles isolate the 'pure' shallow cumulus regime that we wish to characterize, and these quartiles are where the NGAqua-simulated increase of low-cloud fraction with SST warming is the strongest. The top CRH quartile isolates most deep convection that we wish to exclude from our analysis.

Figure 2.1 shows vertical profiles of selected variables averaged across the four NGAqua CRH quartiles. Figure 2.1a shows cloud condensate QN. The first and second CRH quartiles (Q1 and Q2) contain mostly low-level clouds with the tops at approximately 2 km. The third quartile (Q3) has a slight amount of deeper cumulus with tops deeper than 3 km, and the fourth quartile (Q4) has substantial condensate in deeper cloud. Figures 2.1c (relative humidity) and 2.1e (total non-precipitating water mixing ratio (q_t) show that the lower CRH in Q1 and Q2 is associated with a drier boundary layer but mostly a drier free troposphere. The s_{li} profiles in Figure 2.1f show the drier quartiles also have a better mixed sub-cloud layer and more pronounced inversion. Figure 2.1d shows the they also have much stronger subsidence. Figure 2.1f shows the full-sky radiative heating rate (R_{full}). The driest quartile Q1 has the strongest full-sky radiative cooling near the cloud top, since an dry overlying free troposphere allows efficient longwave cooling of the moist boundary layer.

The grid layer nearest the surface has higher QT and RH and a small peak in QN that indicates an occasional fog layer in the subtropics. This is likely because the large aspect ratio of NGAqua's grid cells near the surface (4 km horizontally and 37 m vertically) causes turbulent eddies to be too flat and their vertical velocities to be too weak to allow efficient resolved-scale ventilation of near-surface moisture. NGAqua's parameterized subgrid vertical diffusion of humidity is too weak to compensate for this bias.

Figure 2.3 shows quartile-binned column-integrated statistics such as cloud cover, precipitation, and top-of-atmosphere cloud radiative effects, for the NGAqua control and 4K simulations. Cloud between the surface and 700 hPa is called low, and cloud above 700 hPa is categorized as mid+high. In both simulations, the CRH varies from 40% in the driest quartile to 65% in the moistest quartile, and increases by 1-2% with the warmer SST in

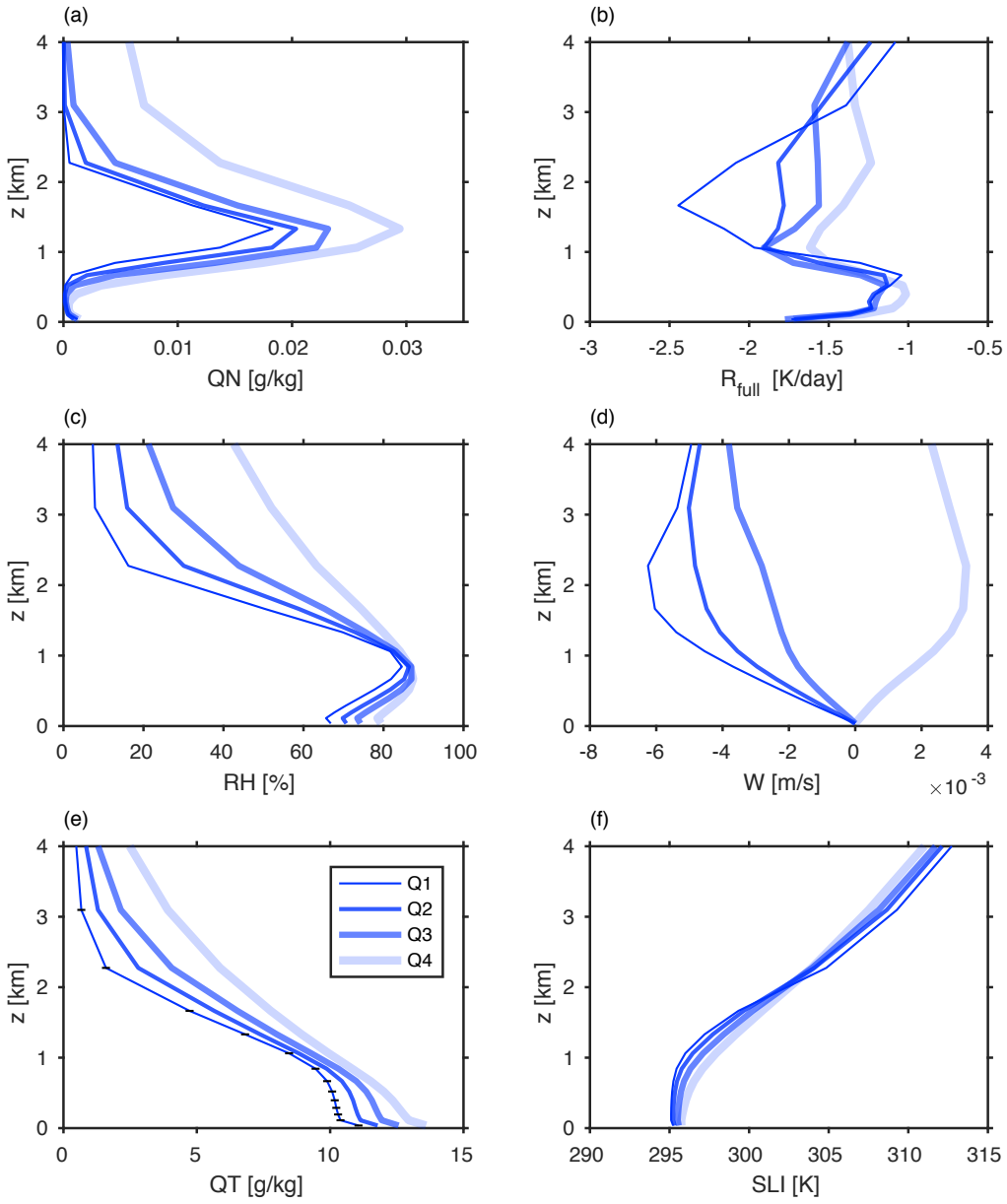

Figure 2.1: Vertical profiles of different weather regimes in the subtropics of NGAqua control simulation

Vertical profiles of: (a) cloud liquid water and ice mixing ratio (QN),
(b) full-sky (both cloudy and clear) radiative heating rate (R_{full}),
(c) relative humidity (RH), (d) vertical velocity (W),
(e) total non-precipitating water mixing ratio (QT), and
(f) liquid-ice water static energy in temperature units (SLI/c_p)
of the CTL NGAqua subtropics binned by quartiles of column relative humidity.
The lowest quartile (Q1) isolates a shallow cumulus regime with the strongest large-scale subsidence and the least amount of deep precipitating cloud. In Panel (e), the short horizontal black lines on the QT profile from Q1 indicate the vertical grid spacing of NGAqua.

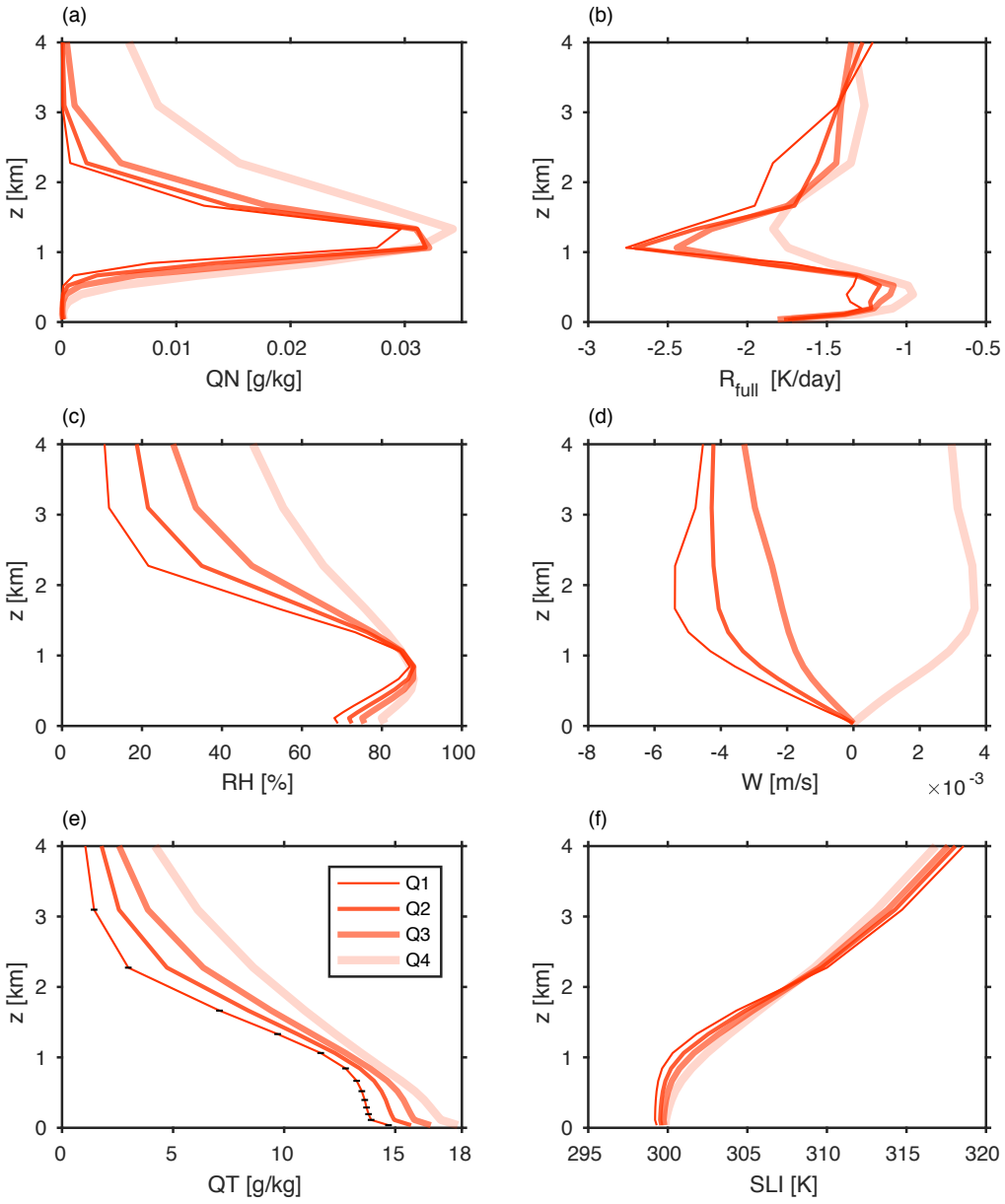

Figure 2.2: Vertical profiles of different weather regimes in the subtropics of NGAqua 4K simulation.

As in Figure 2.1, but for the 4K NGAqua simulation.

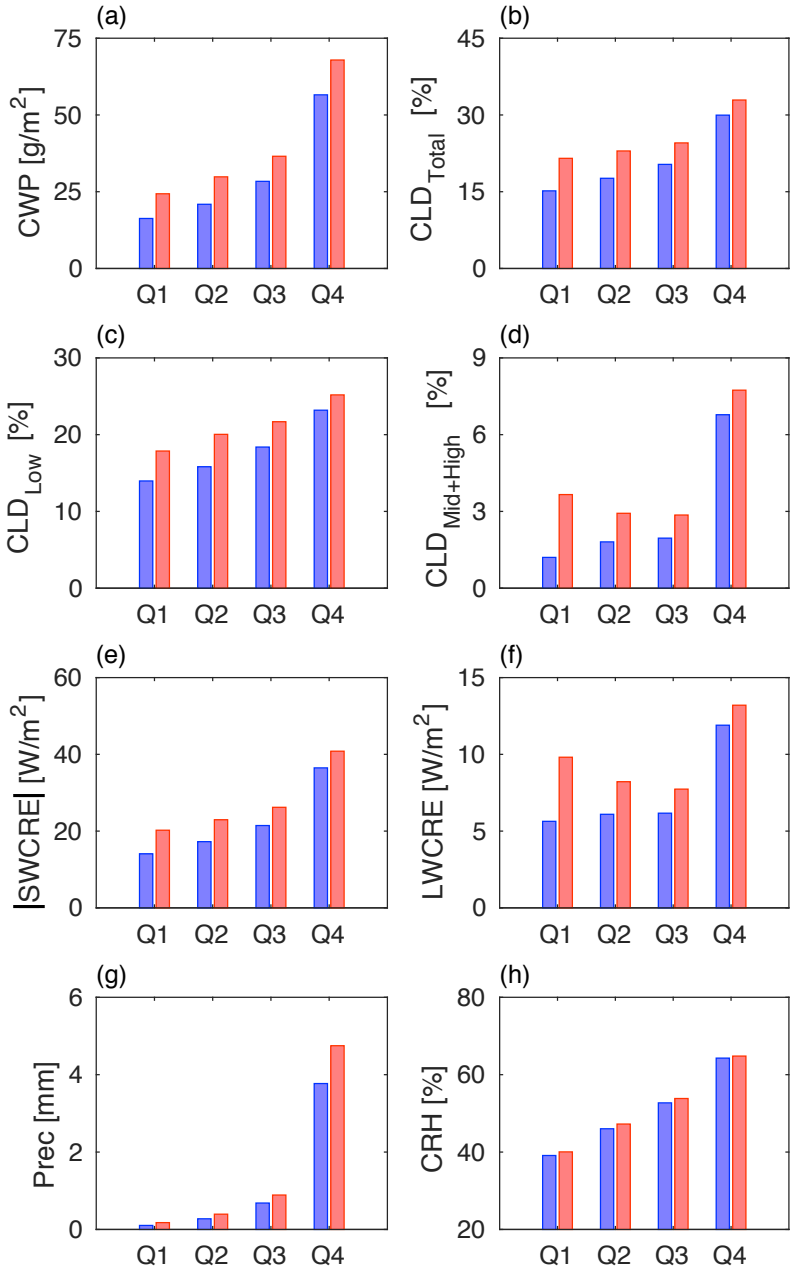

Figure 2.3: Results of other variable fields from the subtropics of NGAqua CTL and 4K simulations

Averages of (a) liquid cloud water path, (b) total cloud fraction, (c) low-level cloud fraction, (d) mid- and high-level cloud fraction, (e) the magnitude of shortwave cloud radiative effect, (f) longwave cloud radiative effect, (g) precipitation, (h) and column relative humidity from the CTL (blue) and +4K SST (red) simulations in Q1 through Q4 of the NGAqua subtropics.

all quartiles (Fig. 2.3h). Q1, Q2, and to a lesser extent Q3 have very little precipitation (Fig. 2.3g) and exhibit strong low cloud cover and cloud water path increases (Fig. 2.3a, c) that drive stronger shortwave cloud radiative effect (SWCRE) with warmer SST (Fig. 2.3e). These quartiles all have a small amount of middle and high cloud (Figure 2.3d) and associated longwave cloud radiative effect (LWCRE)(Fig. 2.3f), which is not strongly correlated with the CRH and which increases in a warmer climate. Q4 shows weaker negative SWCRE feedbacks and includes considerable high cloud and precipitation associated with the ITCZ and mid-latitude cyclones.

2.3.2 Subtropical CRH-quartile binned LASAM forcings

To focus on the shallow cumulus regime in which the negative shortwave feedback is strongest, we used the advective forcings averaged over Q1, the quartile of blocks with lowest CRH, for our primary set of LASAM simulations. We also did similar sets of LASAM simulations using Q2 and Q3 forcings and boundary conditions. Figures 2.1 and 2.3, along with Figures 4, 9 and 12 of Narenpitak et al. (2017), show that many of the Q3 statistics such as vertical velocity, cloud condensate, s_{li}, low-level cloud fraction and the magnitude of SWCRE, match the NGAqua subtropical averages quite well [39],. However, when used in LASAM, the Q3 forcings produce a deeper cumulus-topped boundary layer compared to NGAqua and produce only a marginal sensitivity of cloud fraction and cloud water path to warmer SST. Thus, we focus on the Q1 and Q2 simulations.

The forcings derived from the NGAqua control and 4K simulations differ not only in SST but also in their vertical profiles of large-scale vertical motion, horizontal wind, free-tropospheric temperature and RH, as shown for Q1 in Figure 2.4c-f. In particular, both Q1 and Q2 of the 4K simulation have weaker subsidence and higher free-tropospheric RH than in the control simulation. For all simulations, the zenith angle and insolation are set to the corresponding NGAqua value at the central latitude of the northern subtropics, 17.3°N, and the SSTs are set to the corresponding quartile-means from NGAqua, as summarized in Table 2.1.

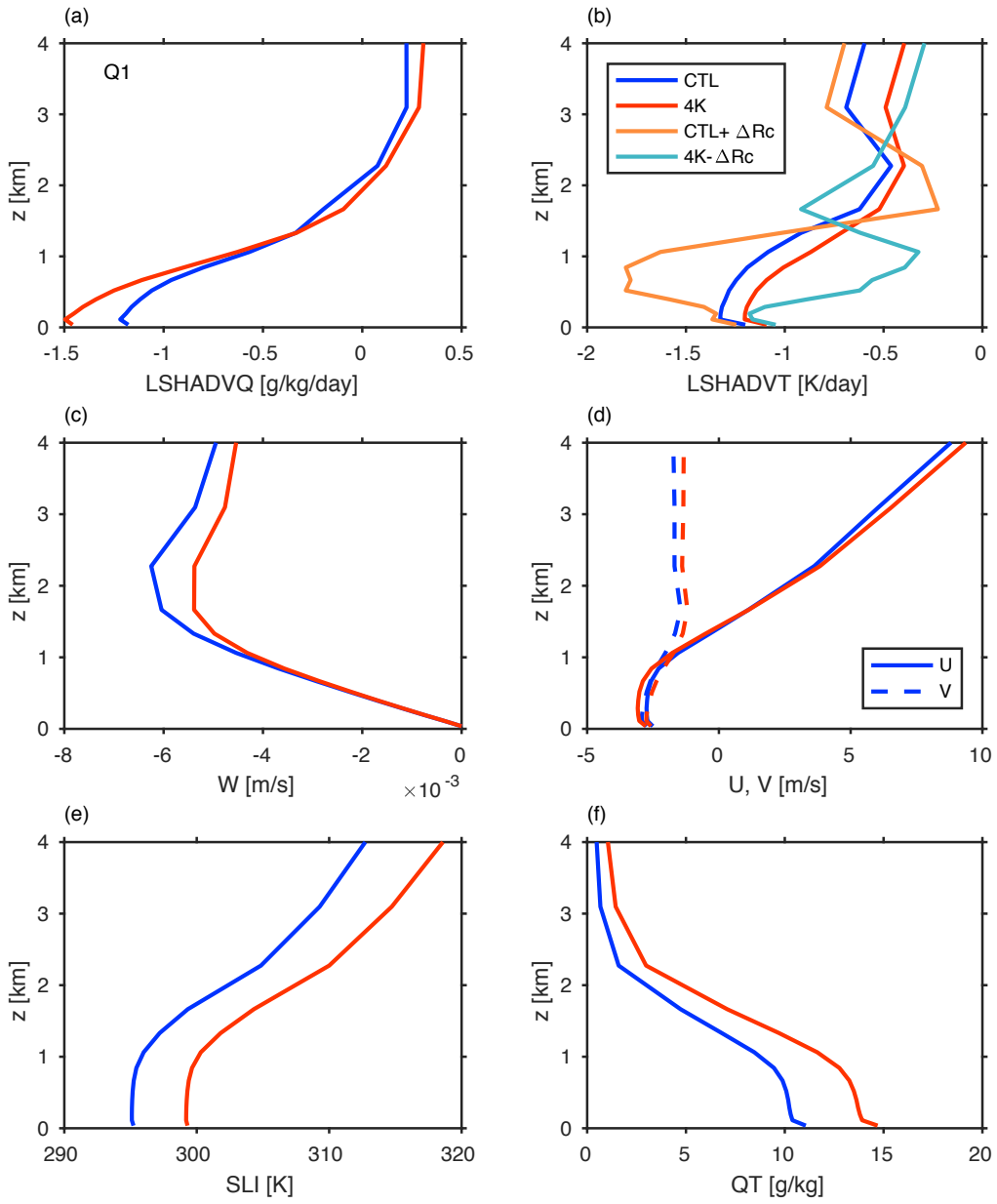

Figure 2.4: Forcings for LASAM 'Q1' simulations

Vertical profiles of

(a-b) large-scale horizontal advective tendencies of moisture and temperature,

(c) W, (d) zonal and meridional wind (U and V, respectively),

(e) SLI, and (f) QT

averaged over the lowest CRH quartile or 'Q1.' The boundary-layer clear-sky radiative cooling changes are accounted for in the temperature tendencies of the CTL+ΔRc and 4K-ΔRc simulations.

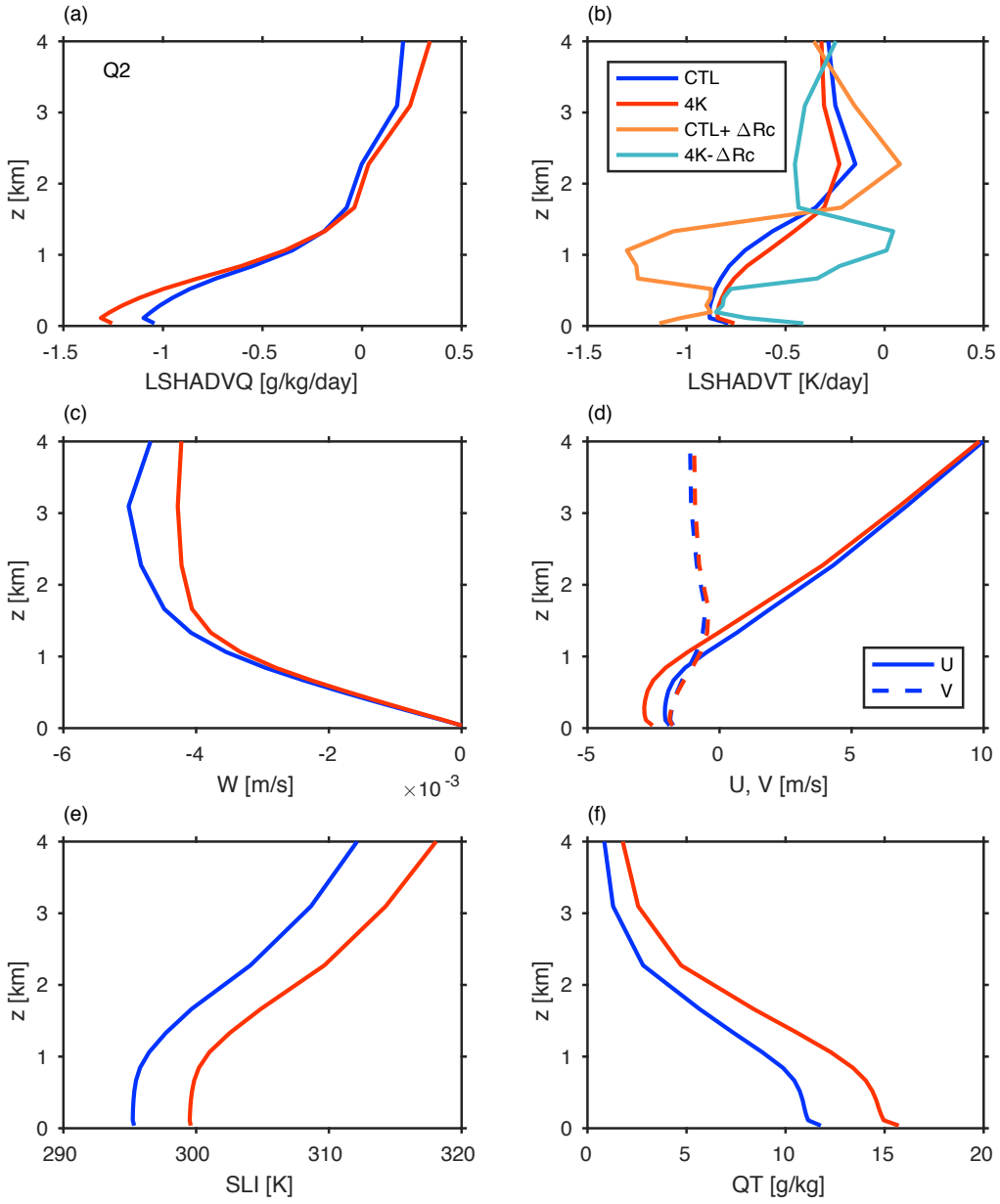

Figure 2.5: Forcings for LASAM 'Q2' simulations

As in Figure 2.4, but for the second CRH quartile of the NGAqua subtropics or 'Q2.'

Table 2.1: Parameter settings for LASAM control (CTL) simulations. The 4K simulations use the same parameters but with SST increased by 4 K.

Parameter	Value
Latitude [° N]	17.28
Q1 SST [K]	297.09
Q2 SST [K]	296.94
Insolation [W/m^2]	418.10
Zenith angle [°]	41.47

Large-scale horizontal moisture and temperature advection tendencies (LSHADVQ and LSHADVT) are also prescribed, based on the tendencies derived from NGAqua Q1 and Q2. The Q1 control and 4K advective forcings are shown in Figure 2.4a-b. They are:

$$\text{LSHADVQ}(z) = -\overline{u(x,y,z,t)\frac{\partial q_t}{\partial x}(x,y,z,t)} - \overline{v(x,y,z,t)\frac{\partial q_t}{\partial y}(x,y,z,t)}, \tag{2.1}$$

and

$$\text{LSHADVT}(z) = -\overline{u(x,y,z,t)\frac{\partial s_{li}}{\partial x}(x,y,z,t)} - \overline{v(x,y,z,t)\frac{\partial s_{li}}{\partial y}(x,y,z,t)}. \tag{2.2}$$

Here, u and v represent the mesoscale-block, daily-averaged zonal and meridional wind of NGAqua, and the partial derivatives are centered differences across the 160 km $\times$160 km blocks of the corresponding fields. The overlines indicate averaging within a CRH quartile. Finally, vertical advective tendencies of horizontally-averaged q_t and s_{li} are computed using the large-scale W (Fig. 2.4d).

2.3.3 Temperature, moisture and wind relaxation

To ensure LASAM does not slowly drift from the atmospheric states of NGAqua CTL and 4K simulations, we use Newtonian relaxation to nudge the horizontal-mean temperature and moisture profiles in LASAM toward the corresponding NGAqua quartile-averaged s_{li} and q_t profiles. We use a relaxation time scale of 1 day throughout the entire atmosphere. We

arrived at this choice after trying other relaxation time scales, e.g. 2 and 5 days, and different nudging layers, e.g. mid and upper troposphere only (above 4 km) or free troposphere only (above 2.5 km). LASAM's cloud layer deepens slightly and precipitates more when a longer nudging time scale is used, making LASAM a less good analogue to NGAqua. Even with a 1-day relaxation time scale, the nudging tendencies remain fairly small compared to the other budget terms, i.e. no larger than 1.5 g/kg/day or K/day in magnitude, while the LASAM s_{li}, q_t and RH profiles still match those from NGAqua well. In Section 4.4 we show that the cumulus cloud increase with 4 K SST warming is not very sensitive to the thermodynamic nudging.

The zonal and meridional domain-mean winds are tightly nudged throughout the entire atmosphere, based on NGAqua subtropical-mean $\overline{u(x,y,z,t)}$ and $\overline{v(x,y,z,t)}$ wind profiles, with a relaxation time scale of 10 minutes but without Coriolis or pressure-gradient forcing.

2.3.4 Surface fluxes

In the LASAM simulations presented in this chapter, surface latent and sensible heat fluxes (LHF and SHF, respectively) are calculated using SAM's default Monin-Obukhov scheme, but with prescribed effective surface wind speeds c_0 separately computed for each corresponding NGAqua CRH quartile and simulation. This approach is chosen instead of using fixed surface fluxes to allow the LASAM simulations to have realistic surface flux feedbacks on the boundary layer, while maintaining similar LHF and SHF as the corresponding NGAqua quartiles. Customizing the wind speeds for each simulation accounts for climate-dependent influences on surface wind speed in NGAqua.

We set $c_0 = c_s + 0.5\sigma_{cs}$, where $c_s = (u_s^2 + v_s^2)^{1/2}$ is the NGAqua CRH-quartile average of the surface wind speed (around 5 m/s in all cases) and σ_{cs} is the standard deviation of c_s within that quartile (around 2 m/s in all cases). When the adjustment term $0.5\sigma_{cs}$ is added to the quartile-average c_s, the LASAM-simulated LHF and SHF approximately match the values from NGAqua of the corresponding CRH quartiles. This adjustment term accounts for (1) covariability within NGAqua quartiles between periods of cool, dry air near the surface

and stronger surface winds that enhance the surface fluxes, and (2) the zonal and meridional surface winds in LASAM being a few percent weaker than in NGAqua due to the surface drag at the lowest model level acting over the finite wind-nudging timescale. The values of c_0 are 6.5 and 6.1 m/s for the CTL and 4K LASAM Q1 simulations, respectively, and are 6.1 and 5.7 m/s, respectively, for Q2.

2.3.5 Simulations to be presented

Table 2.2 summarizes the eight main LASAM simulations to be presented in Section 2.4. In addition to the control (CTL) and 4K simulations, we discuss three pairs of sensitivity studies that aim to quantify the importance of possible mechanisms for the simulated increase in subtropical shallow cumulus cloud cover associated with warmer SSTs.

The first pair of sensitivity studies, discussed in Section 2.4.1, investigates the role of the increased boundary-layer clear-sky radiative cooling (R_{clr}) in the 4K climate. For the CTL+ΔRc simulation, the profile of clear-sky radiative cooling difference between the LASAM CTL and 4K simulations (ΔR_{clr}) is added to the CTL large-scale horizontal temperature advection tendency (blue curve) to get the orange curve, as shown in Figure 2.4b. This essentially applies to the CTL simulation the horizontal-mean clear-sky radiative cooling from the 4K simulation. Comparing the orange and blue curves, the 4K simulation has stronger clear-sky cooling within the moist layer below 1.4 km and weaker clear-sky cooling between 1.4–2.5 km, the trade inversion layer. To check for linearity of the response, we perform a reversed test 4K-ΔRc in which ΔR_{clr} is subtracted from the horizontal advective forcing of the 4K simulation, i.e. we apply the CTL clear-sky radiative cooling to the 4K simulation.

The second pair of sensitivity studies, discussed in Section 2.4.2, investigates the role of the slight increase in subtropical free-tropospheric relative humidity (RH_{FT}) seen with warmer SST. In the 4K-ΔRH simulation (Table 2.2), the q_t profile of the 4K simulation is modified to reduce RH_{FT} to match the CTL simulation, while the RH in the boundary layer remains the same. To check for linearity, we perform a reversed test, increasing the

Table 2.2: Principal LASAM simulations

Cases	SST and forcings	R_{clr}	RH_{FT}	CO_2 [ppm]
Control (CTL)	CTL	CTL	CTL	350
+4K SST (4K)	4K	4K	4K	350
CTL+ΔRc	CTL	**4K**	CTL	350
4K-ΔRc	4K	**CTL**	4K	350
CTL+ΔRH	CTL	CTL	**4K**	350
4K-ΔRH	4K	4K	**CTL**	350
CTL+4×CO2	CTL	CTL	CTL	**1400**
4K+4×CO2	4K	4K	4K	**1400**

free-tropospheric q_t of the CTL simulation to match the RH_{FT} of the 4K simulation.

The third pair of sensitivity studies, discussed in Section 2.4.3, investigates the role of CO_2 quadrupling in the CTL and 4K climates in changing the radiative cooling of the cloudy boundary layer. For the CTL+4×CO2 simulation, the CTL thermodynamic profiles and large-scale forcings are used, except with quadrupled CO_2 concentration (1400 ppm). The 4K+4×CO2 simulation similarly uses the large-scale profiles and forcings of the 4K simulation but with quadrupled CO_2. If the subtropical shallow cumuli cloud fraction increase is caused by enhanced boundary-layer clear-sky radiative cooling, and if this is affected by changed CO_2, we might also anticipate an impact on the cumulus cloud cover.

2.4 Results

The first goal of the LASAM simulations is to approximately reproduce the NGAqua mean cloud cover and vertical structure of the corresponding CRH quartile, as well as NGAqua's response to a 4 K SST warming.

Figure 2.6a shows a perspective plot of the clouds from the LASAM Q1 control simu-

lation after 60 days. By this time, the simulation is in a statistical steady state. As in NGAqua, the shallow cumuli are only coarsely resolved and barely precipitate. With this small LASAM domain size, there is no obvious mesoscale aggregation of the convection or the surface relative humidity (RH, color shading) in this simulation. This makes for a meaningful comparison with the full NGAqua simulation, which also shows little aggregation in the simulated clouds or surface RH from the driest quartile (Fig. 2.6b).

The left column of Figure 2.7 shows the time series of LASAM low cloud fraction, liquid cloud water path, and $\left|\text{SWCRE}\right|$ of the Q1 simulations. The short horizontal bars on the right hand side indicate the $\pm 1\sigma$ uncertainty range of the day 11-60 time-mean values of the time series (the vertical width of the bars is often too narrow to discern). If these error bars do not overlap for two simulations, their true underlying means are different with more than 95% statistical confidence. The sampling variability of the mean is estimated from the number of daily samples and lag-1 autocorrelation of the analyzed time series [13].

Despite our best efforts to maintain consistency between the advective forcings and thermodynamic profiles of the LASAM and NGAqua simulations, the low cloud fraction of the CTL (blue) and 4K (red) LASAM simulations tend to lie below the NGAqua Q1 averages (dashed lines). The cloud water path from LASAM is comparable with NGAqua, while the SWCRE is stronger. Such differences are to be expected when using simplified steady-state LASAM simulations to mimic complicated, transient conditions in NGAqua. For example, use of diurnally-averaged insolation is likely to cause a stronger SWCRE in LASAM Blossey et al. (2009), because in NGAqua, like in reality, boundary-layer clouds tend to decrease during the day [2].

Encouragingly, the LASAM simulations qualitatively capture the low-cloud increase due to 4 K SST warming produced in the subtropics of NGAqua [39]. Although LASAM simulates a smaller change in all three cloud metrics than NGAqua, the mean changes are highly statistically significant. The right column of Figure 2.7 shows that similar results are obtained for Q2. The top four rows of Table 2.5 gives the corresponding numerical results averaged over Q1 of the NGAqua subtropics and Days 11-60 of the LASAM Q1 simulations, respectively.

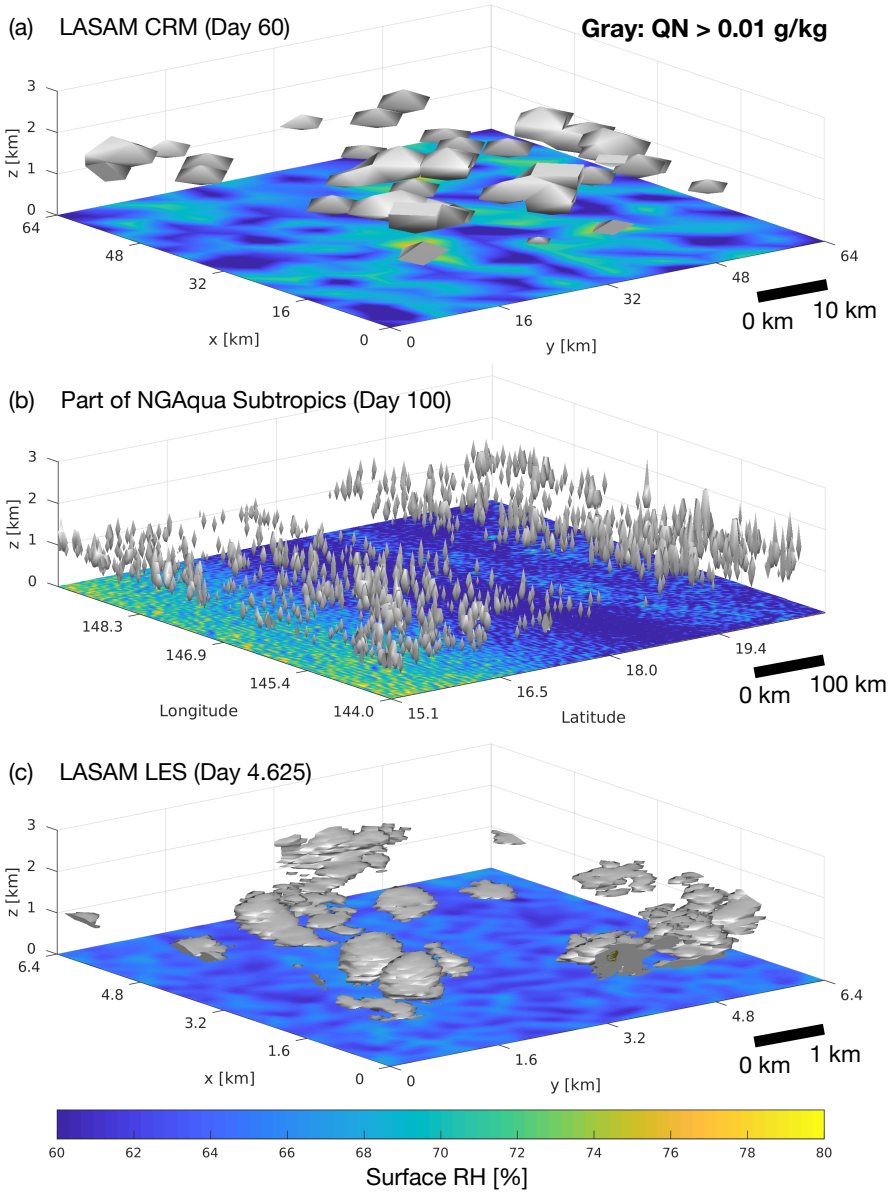

Figure 2.6: Examples of shallow cumuli in the lowest CRH quartile (Q1) from LASAM and NGAqua CTL simulations.

(a) Isosurfaces of the cloud condensate (QN, gray) at the last hour of Day 60 from the CTL LASAM Q1 simulation, with 4 km horizontal resolution and 16×16×34 gridpoints. The domain size is 64 km × 64 km. (b) Isosurfaces of QN taken from a 640 km × 640 km block (10 times larger than LASAM) in the subtropics of a CTL NGAqua simulation at the last hour of Day 100. The block-averaged cloud fraction and RH profile are representative of the NGAqua Q1 quartile mean. (c) Isosurfaces of QN at Day 4.625 from the LES version of CTL LASAM Q1 simulation, with 100×100×40 m resolution and 64×64×115 gridpoints. The domain size is 6.4 km × 6.4 km. The horizontal axes of the panels have different scales. The color shading shows the surface relative humidity.

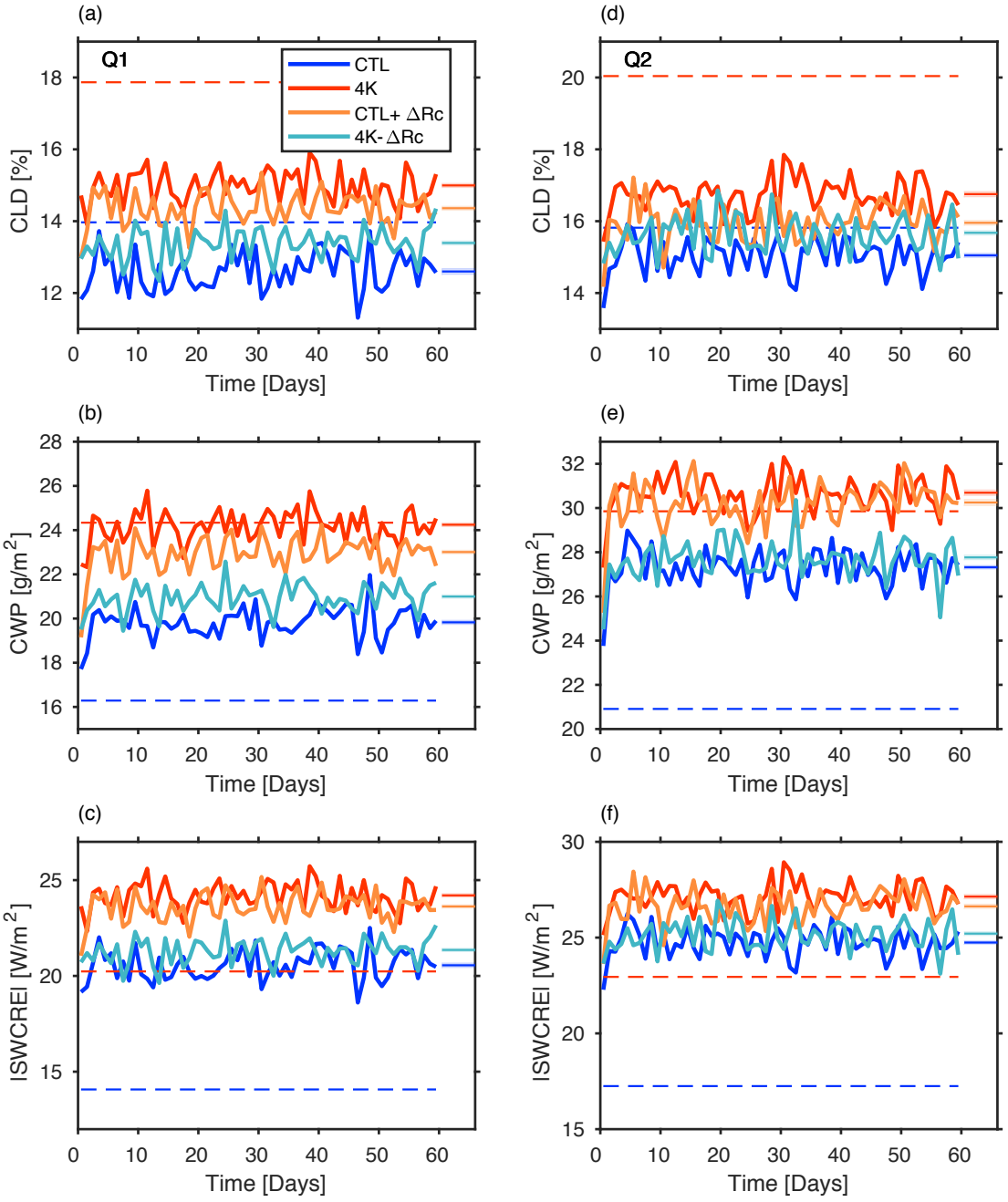

Figure 2.7: Time series from LASAM Q1 and Q2 simulations

Time series of (a) low cloud fraction, (b) cloud water path, and (c) magnitude of shortwave cloud radiative effect of LASAM Q1 simulations. The short horizontal lines on the right hand side indicate the time-means, and the shaded bars $\pm 1\sigma$ uncertainty ranges from the time-means of the time series during Days 11-60. The dashed lines indicate the NGAqua Q1 averages. Q2 results are shown in (d)-(f).

By design, the LASAM Q1 surface latent and sensible heat fluxes closely match the Q1 fluxes from NGAqua. Both the LASAM Q1 CTL and 4K simulations have negligible precipitation, only 0.05-0.06 mm/day.

2.4.1 Could clear-sky radiative cooling explain the warming-induced shallow cumulus increase?

Figure 2.7 and Table 2.5 also show CTL+ΔRc and 4K-ΔRc simulations, which test whether the stronger boundary-layer clear-sky radiative cooling in 4K compared to CTL could explain the warming-induced shallow cumulus cloud cover increase. Indeed, the low cloud cover increase from CTL to CTL+ΔRc is approximately 75% of the increase due to 4 K SST warming in Q1 simulations and 50% in Q2 simulations. The radiatively-driven increases in cloud water path and the magnitude of SWCRE are almost as large as those from the 4K simulations. The change from the 4K-ΔRc to the 4K simulations shows similar results.

Figure 2.8a-b shows mean vertical profiles of cloud fraction and cloud liquid water from Days 11 - 60 of the LASAM Q1 simulations. Peak cloud fraction and liquid water increase from the CTL to the 4K simulations, but the thickness of the cloud layer is nearly unchanged for the warmer SST. This is not merely an artifact of a coarse vertical grid; Section 4.2 shows that comparable results are obtained with a similarly-nudged fine resolution large-eddy simulation. The CTL+ΔRc simulation approximately matches the cloud fraction and liquid water profiles of the 4K simulation. Likewise, the 4K-ΔRc simulation has similar cloud vertical structure to the CTL simulation.

The full-sky radiative heating and clear-sky radiative heating rates (R_{clr}) are shown in Figure 2.8c-d. The changes below 2.5 km in the 4K cases are mostly driven by longwave radiation; +4K changes in shortwave heating are less than 0.1 K/day throughout the atmospheric column. The 4K cases have stronger clear-sky radiative cooling below 1.5 km, a result of higher emissivity due to more water vapor held by the warmer atmospheric column. In contrast, in the warmer climate the longwave clear-sky cooling is weaker at the top of the moist boundary layer, between 1.7 and 2.3 km. The overlying free troposphere is also

Table 2.3: Auxiliary statistics for the NGAqua and the default LASAM Q1 simulations

For LASAM, the statistics are time-averaged after the simulations have equilibrated, i.e., Days 11-60. For NGAqua, the 4-km resolution outputs from Days 21-100 are first block-averaged to 160-km resolution, and then binned into four quartiles based on CRH. The statistics of the lowest CRH quartile are presented here.

Simulations		CLD [%]	CWP [g/m^2]	|SWCRE| [W/m^2]	Prec [mm/d]	LHF [W/m^2]	SHF [W/m^2]	EIS [K]	$\delta^d s_{vl}$ [K]	$\delta^m s_{vl}$ [K]
NGAqua	CTL	14.0	16.3	14.1	0.10	170.0	14.9	0.6	6.0	1.7
	4K	17.9	24.3	20.2	0.18	189.9	12.6	1.0	6.1	2.0
4 km	CTL	12.6	19.8	20.6	0.05	172.1	14.4	0.5	6.3	1.7
MPDATA	4K	15.0	24.2	24.2	0.06	194.8	12.6	0.9	6.6	2.1
Nudged	CTL+ΔRc	14.4	23.0	23.6	0.06	174.5	15.3	0.5	6.4	1.9
(Default)	4K-ΔRc	13.4	21.0	21.4	0.06	192.0	11.9	0.9	6.5	1.9
	CTL+ΔRH	13.3	20.7	21.5	0.05	170.1	14.3	0.4	6.3	1.8
	4K-ΔRH	14.4	23.4	23.4	0.07	196.9	12.9	1.0	6.6	2.0
	CTL+4$\times$CO2	12.3	18.0	19.7	0.03	169.7	13.7	0.4	6.2	1.8
	4K+4$\times$CO2	15.1	23.0	24.1	0.03	192.2	11.9	0.9	6.5	2.1

Table 2.4: Auxiliary statistics for the other 4-km resolution LASAM Q1 simulations

The statistics are time-averaged after the simulations have equilibrated, i.e., Days 6-30 for 4 km nudged UM5, and Days 11-60 for 4 km un-nudged MPDATA.

Simulations		CLD [%]	CWP [g/m^2]	|SWCRE| [W/m^2]	Prec [mm/d]	LHF [W/m^2]	SHF [W/m^2]	EIS [K]	$\delta^d s_{vl}$ [K]	$\delta^m s_{vl}$ [K]
4 km	CTL	7.0	8.4	10.6	0.00	161.3	15.0	0.7	7.2	1.8
UM5	4K	8.6	11.2	13.0	0.01	183.2	13.4	1.2	7.6	2.1
Nudged	CTL+ΔRc	8.4	10.2	12.8	0.00	163.9	16.0	0.7	7.3	2.0
	4K-ΔRc	7.3	9.1	10.9	0.01	179.4	12.7	1.1	7.6	2.1
4 km	CTL	15.2	27.8	25.1	0.16	156.5	13.4	0.1	5.8	0.4
MPDATA	4K	16.7	30.8	27.2	0.21	176.4	11.4	0.6	6.5	1.2
Un-nudged	CTL+ΔRc	17.6	33.9	29.6	0.23	158.8	14.8	0.2	5.9	0.6
below 2.5 km	4K-ΔRc	14.7	25.0	23.4	0.14	174.3	10.3	0.6	6.4	1.2

Table 2.5: Auxiliary statistics for the other 100-m resolution LASAM Q1 simulations

The statistics are time-averaged after the simulations have equilibrated, i.e., Days 2-6 for 100×100×40 m nudged MPDATA, and Days 6-10 for 100×100×40 m un-nudged MPDATA.

Simulations		CLD [%]	CWP [g/m^2]	|SWCRE| [W/m^2]	Prec [mm/d]	LHF [W/m^2]	SHF [W/m^2]	EIS [K]	$\delta^d s_{vl}$ [K]	$\delta^m s_{vl}$ [K]
100×100×40 m	CTL	6.9	6.6	8.3	0.00	180.7	14.7	0.7	7.8	2.7
MPDATA	4K	7.7	7.9	9.2	0.01	202.1	13.3	1.1	8.3	3.1
Nudged	CTL+ΔRc	8.0	7.9	9.8	0.00	182.2	15.8	0.8	8.0	2.9
	4K-ΔRc	6.4	6.4	7.5	0.01	199.7	12.5	1.1	8.1	3.0
	CTL+4×CO2	6.4	5.8	7.4	0.00	177.4	14.2	0.6	7.9	2.7
	4K+4×CO2	7.2	7.0	8.4	0.00	198.3	12.9	1.1	8.3	3.1
100×100×40 m	CTL	7.7	7.5	7.9	0.00	172.8	13.6	0.6	8.1	2.9
MPDATA	4K	7.9	8.2	7.9	0.01	194.3	12.4	1.1	8.8	3.5
Un-nudged	CTL+ΔRc	8.9	9.0	9.9	0.01	173.5	15.5	0.7	8.2	3.1
below 2.5 km	4K-ΔRc	6.7	6.7	5.8	0.01	193.0	10.7	1.0	8.8	3.2

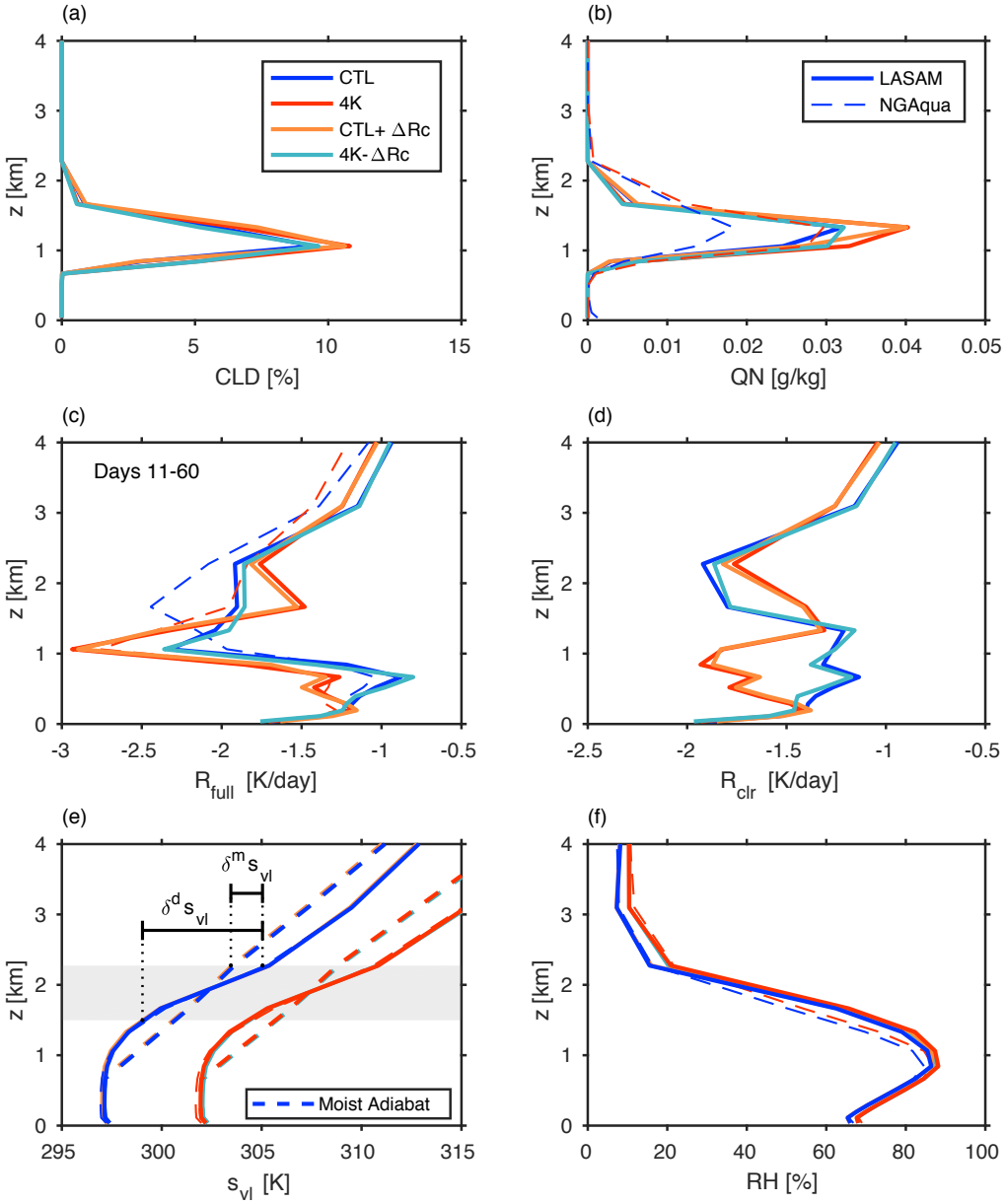

Figure 2.8: Vertical profiles from LASAM Q1 simulations

Vertical profiles of (a) cloud fraction, (b) cloud liquid water and ice mixing ratio, (c) full-sky (cloudy and clear) radiative heating rate, (d) clear-sky radiative heating rate, (e) liquid virtual static energy together with the moist pseudo-adiabats (thick dashed lines), and (f) relative humidity from Days 11-60 of LASAM Q1 simulations. The thin dashed lines indicate the NGAqua Q1 averages of the available fields. The definitions of the two inversion stability measures, $\delta^d s_{vl}$ and $\delta^m s_{vl}$ are also shown in Panel (e); see text for detail.

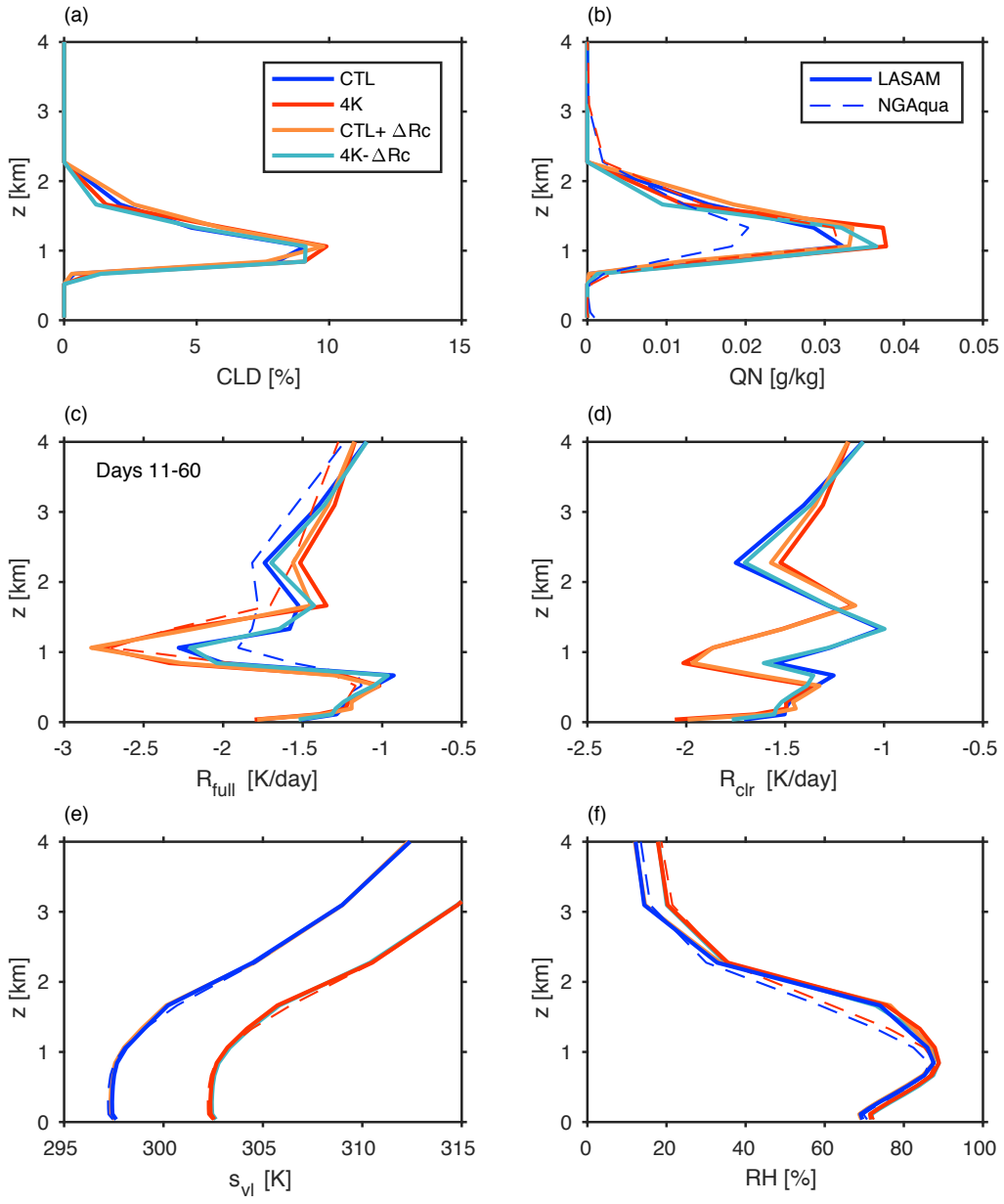

Figure 2.9: Vertical profiles from LASAM Q2 simulations

As in Figure 2.8 but for the Q2 simulations.

moister and more emissive, producing more downwelling longwave radiation that is absorbed near the boundary-layer top, counteracting the upwelling black-body emission in that region to reduce its overall clear-sky longwave cooling. An offline radiation test shows that these radiative cooling responses below 2.5 km are mainly due to the increased humidity, not the warmer temperature (not shown), and that similar conclusions hold if the temperature and humidity changes are scaled down to a 2 K SST increase or an 8 K SST increase. The magnitude of R_{full} is stronger than R_{clr} at the level of maximum cloud cover because of longwave cooling from the clouds. However, even in the cumulus layer, the +4K difference in R_{full} is similar to the difference in R_{clr} because the cloud cover is small and doesn't change enough with warming to be radiatively important.

Figure 2.8e shows the corresponding profile of liquid virtual static energy, a moist-conserved variable that in unsaturated air reduces to the virtual static energy $s_v = c_p T_v + gz$ and hence is a measure of unsaturated air parcel buoyancy convenient for diagnosing boundary-layer dynamics:

$$s_{vl} = s_l + 0.61 c_p T_{\rm ref} q_t, \tag{2.3}$$

Here $s_l = c_p T + gz - L_v q_l$ is the liquid static energy and L_v is the latent heat of vaporization. The reference temperature $T_{\rm ref}$ is chosen as the mass-weighted average temperature below 700 hPa. Moist pseudo-adiabats originating from the cumulus base at 700 m altitude for CTL and 4K are shown as thick dashed lines. The cumulus layer has the expected structure of a well-mixed subcloud layer, a conditionally unstable layer, and an absolutely stable inversion layer with a s_{vl} stratification exceeding moist-adiabatic. Figure 2.8f shows the RH profile. The s_{vl} and RH profiles are nearly identical between the CTL and CTL+ΔRc simulations, and similarly for 4K and 4K-ΔRc.

A corollary is that any changes in inversion strength between CTL/CTL+ΔRc and 4K/4K-ΔRc are not controlling the cloud fraction. This argues against the hypothesis of Narenpitak et al (2017) [39], who suggested the subtropical shallow cumulus increase in a warmer climate might partly be due to a stronger trade inversion that traps moisture and cloud below it, using estimated inversion strength or EIS [61] as a bulk proxy for inver-

sion strength. Table 2.5 shows this and two other more direct measures of inversion strength based on the LASAM s_{vl} profiles, shown in Figure 2.8e. The first measure is the dry stability from the base to the top of the inversion layer:

$$\delta^d s_{vl} = s_{vl}(z_{it}) - s_{vl}(z_{ib}).$$

The second is the moist stability relative to a cumulus updraft rising pseudoadiabatically from the cumulus cloud base to the inversion top:

$$\delta^m s_{vl} = s_{vl}(z_{it}) - s^m_{vl}(z_{it}),$$

As in NGAqua, all of these measures show a slight increase in inversion strength in the warmer climate, mostly not due to the changed radiative cooling. Yet despite such inversion strength changes, CTL+ΔRc has almost the same cumulus cloud fraction as 4K.

The nearly unchanged steady-state vertical structure in the warmer climate occurs despite reduced mean subsidence. We infer that the penetrative entrainment rate, which maintains the depth of the cumulus layer against the mean subsidence, is similarly reduced in the warmer climate. That is, the stronger LHF in the warmer SST does not result in increased penetrative entrainment rate that deepens the cumulus layer and dries out the boundary layer, evidence against the surface flux desiccation mechanism of Rieck et al. (2012) [47]. Because of the shallowness of the simulated cumulus layer, the CTL precipitation and its warming-induced increase are small compared to Vogal et al. (2016) [56], and the CGILS S6 intercomparison study [3]. This is important for our simulated 4K cumulus cloud increase. Blossey et al (2013) noted that in their warmer-SST simulation, clear-sky radiative cooling increased, but the latent heating due to the additional precipitation balanced that cooling with little change in cumulus cloud cover [3]. Section 2.6 presents further analysis of the boundary-layer heat budget for our simulations.

A similar figure for the Q2 simulations is shown in Figure 2.9. For that case the cloud profile changes driven by radiative cooling explain about half the difference between the CTL and 4K simulations. From now on, we will focus on simulations of CRH quartile Q1,

for which the NGAqua low cloud fraction changes are the strongest and there is minimal precipitation.

2.4.2 Could increased free-tropospheric relative humidity explain the warming-induced shallow cumulus increase?

In NGAqua, the RH at the 2.3 km high top of the subtropical trade inversion increases from approximately 15% in the control simulation to 20% in the 4K simulation (Fig. 2.8b). If cumuli are penetratively entraining higher RH air from above, this might support a moister boundary layer with more cloud in the warmer climate, as suggested by prior studies of subtropical stratocumulus cloud [32, 6, 31, 9, 22]. On the other hand, higher free-tropospheric RH in 4K also decreases the clear-sky radiative cooling of the boundary layer compared to 4K-ΔRH, perhaps radiatively counteracting some of the low cloud increase induced by the entrainment of moister air. We test how these effects play out using the LASAM simulation 4K-ΔRH, in which the profile of $\mathrm{RH_{FT}}$ of the 4K simulation is reduced to match the $\mathrm{RH_{FT}}$ of the CTL simulation.

Figure 2.10 shows quasi-steady state mean low-cloud fraction, cloud water path and $\left|\mathrm{SWCRE}\right|$ for all the simulations discussed so far, as well as many to be discussed later. The 4K-ΔRH simulation (purple triangle) produces slightly less cloud and $\left|\mathrm{SWCRE}\right|$ than the 4K simulation, suggesting that the effect of entraining drier air is stronger than that of increased boundary-layer radiative cooling. A complementary CTL+ΔRH simulation (green triangle) shows similar increases in these metrics compared to CTL, demonstrating that the cloud response to $\mathrm{RH_{FT}}$ is linear. Overall, the changes in $\mathrm{RH_{FT}}$ explain a quarter of the CTL-to-4K cloud fraction and $\left|\mathrm{SWCRE}\right|$ increase. Since this is a much lesser fraction than the radiatively-induced cloud changes, we return in the next sections to a more detailed analysis of the radiative mechanism for shallow cumulus cloud increase in a warmer climate.

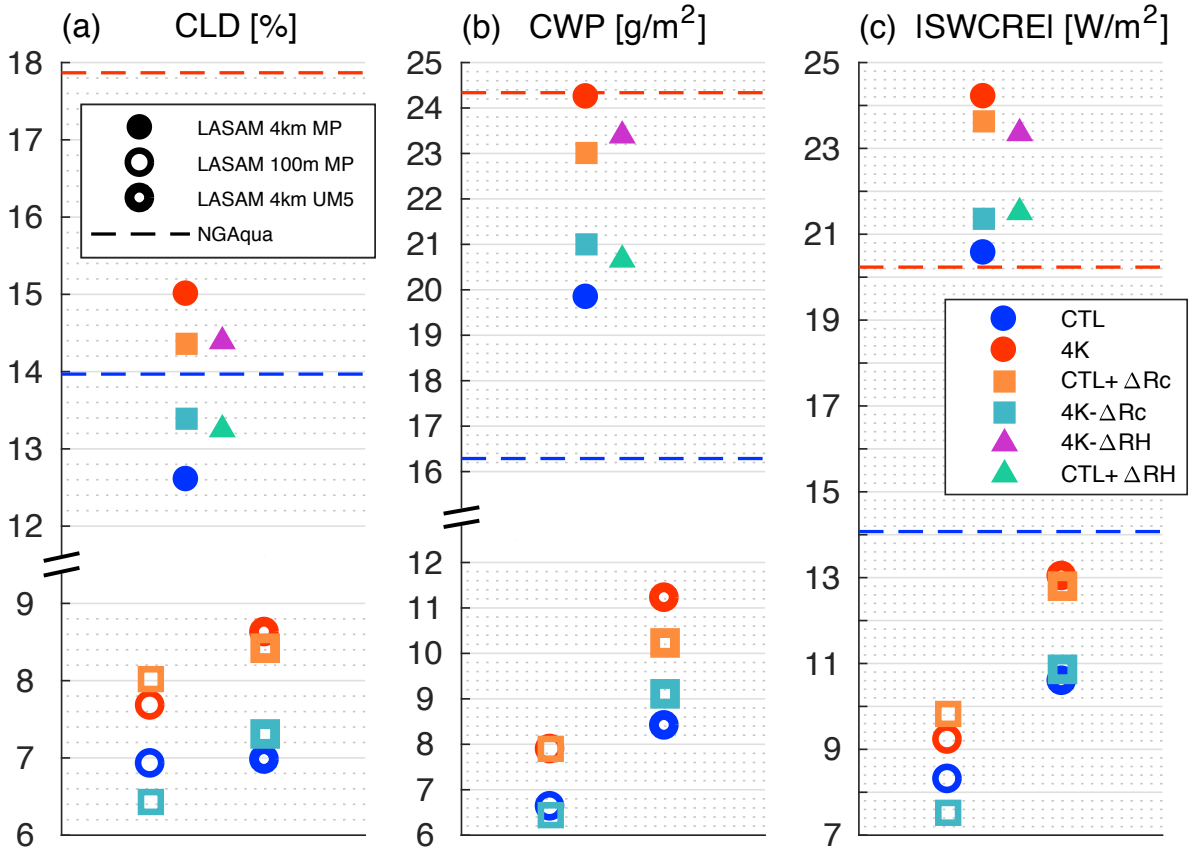

Figure 2.10: Auxiliary statistics from the NGAqua and LASAM Q1 simulations

Averages of (a) low-cloud fraction, (b) cloud water path, and (c) shortwave cloud radiative effect from the LASAM simulations over the period after they have reached statistical equilibrium, as indicated in Table 2.5. The the LASAM Q1 simulations with 4-km horizontal resolution and MPDATA advection scheme are shown in filled symbols. Those with 100-m horizontal resolution and MPDATA advection scheme are shown in open symbols with thinner outlines (left side of each panel), and those with 4-km resolution and UM5 advection scheme are shown in open symbols with thicker outlines (right side of each panel). The CTL and 4K simulations are shown in circles, and the sensitivity tests to enhanced clear-sky boundary-layer radiative cooling are shown in squares. The sensitivity tests to $\mathrm{RH_{FT}}$ (only for those with 4-km resolution and MPDATA advection scheme) are shown in triangles. The dashed lines represent the NGAqua Q1 CTL and 4K results.

2.4.3 What happens when CO_2 concentration increases?

Although the dynamic and thermodynamic changes in NGAqua are mainly driven by 4 K SST warming, what causes greenhouse warming in the real world is primarily CO_2 increase. Thus we made two additional sets of simulations, with CO_2 quadrupled while the forcings of the CTL Q1 and 4K Q1 simulations are otherwise fixed. These are run at both the 4-km and $100 \times 100 \times 40$-m resolutions. They are referred to as CTL+4×CO2 and 4K+4×CO2, respectively.

In general, with quadrupled CO_2 alone, there is more clear-sky radiative warming below 3 km. The enhanced radiative warming reduces the cloud fraction and water path (Table 2.5). The cloud layer shallows with CO_2 quadrupling even though the inversion becomes slightly weaker with respect to dry stability.

When both 4 K SST warming and CO_2 quadrupling are combined, the cloud fraction and water path in the 4K+4×CO2 simulation are less than those in 4K, but still greater than those in CTL. This is because the SST warming increases the boundary-layer humidity from the CTL simulation, causing an overall stronger radiative cooling below 1.2 km and more cloud cover near the cloud base. Although the stronger radiative warming in the inversion layer shallows the cloud, there is still enhanced clear-sky radiative cooling below 1.2 km and the shaded cloud fraction increases. Although the direct effect of CO_2 on the clouds and boundary layer is significant, we find it is not the dominant control on low cloud cover. Thus, we focus on the cloud responses to 4 K SST warming and the governing radiative mechanism in the rest of the paper.

2.5 Sensitivity Tests

The LASAM simulations discussed so far use a 4-km horizontal resolution to be consistent with NGAqua. As this resolution is too coarse to realistically resolve marine boundary-layer clouds, the representation of clouds may be sensitive to the discretization of the governing equations and, in particular, to the choice of scalar advection scheme. There are also tradeoffs

in the choice of LASAM domain size: A larger domain may produce more robust statistics but also may lead to self-aggregation unrepresentative of NGAqua simulations.

In this section we explore the sensitivity of LASAM, and by implication NGAqua, to these choices. The Q1 large-scale forcings are used to force all simulations in this section. In simulations with enhanced radiative cooling (Sections 2.5.2-2.5.4), ΔR_{clr} is found by subtracting the CTL R_{clr} from the 4K R_{clr} of the corresponding simulations.

2.5.1 Sensitivity to domain size

A larger LASAM domain size that samples more grid cells would reduce the statistical noisiness of the domain-mean cloud properties. We explored LASAM simulations with two larger domains, 128 km $\times$ 128 km and 256 km $\times$ 256 km. The complication is that these tend to self-aggregate after approximately 10 days into bands parallel to the cumulus-layer wind shear, after which approximately half of the LASAM domain is covered with shallow cumuli while the other half is dry. This slightly influences the domain-mean cloud fraction, radiative properties and cloud feedbacks. The majority of them reach a new equilibrium after 30 days, except for the CTL 256 km $\times$ 256 km simulation, which keeps self-aggregating.

We quantify the degree of self-aggregation using a measure of the mesoscale precipitable water (PW) variability, because we observe a strong correlation between mesoscale variations of shallow cumulus cloud cover and PW [11]. We first average the instantaneous PW fields to 16 km $\times$ 16 km blocks (4$\times$4 horizontal grid columns) in order to remove the small-scale noise. The self-aggregation index is defined as the ratio between the standard deviation of PW (σ_{PW}) to the domain-mean PW at every time step ($\overline{PW}$). It is computed every 3 hours then daily-averaged for plotting. For NGAqua, the PW distributions are computed over non-overlapping 256 km $\times$ 256 km blocks sampled over the entire subtropics, both northern and southern hemispheres, during the first and last three hours for which we have model outputs.

In NGAqua, the self-aggregation index varies over a fairly wide range between blocks, even within the same CRH quartile. In part this is because a single block may include

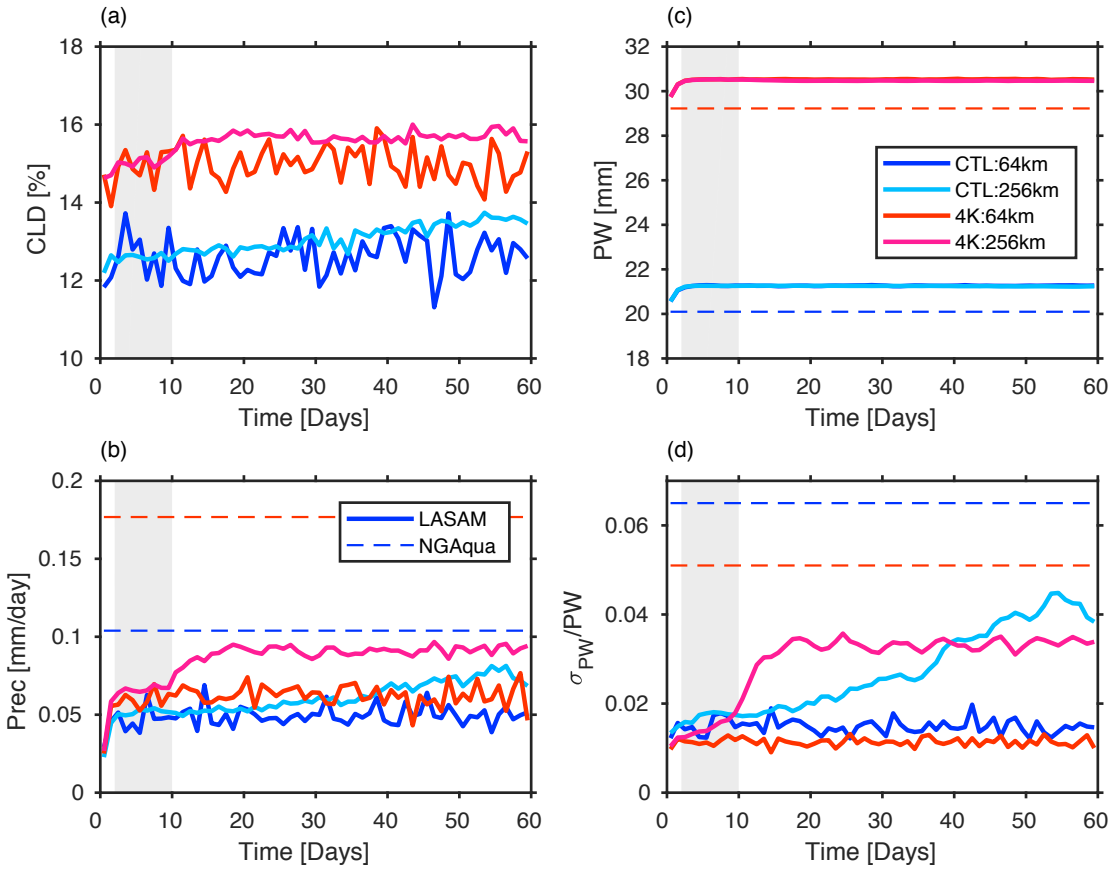

Figure 2.11: Sensitivity to domain size

The sensitivity to domain size for the LASAM Q1 simulations, using 4 km resolution with the control and +4K SST. The domain sizes are 64 km × 64 km (i.e. the CTL and 4K simulations in Figure 2.7) and 256 km × 256 km. The time series shown are (a) low-cloud fraction, (b) precipitation, (c) precipitable water (PW), and (d) the self-aggregation index ($\sigma_{\mathrm{PW}}/\overline{PW}$). The dashed lines in Panels (b)-(d) are values from the NGAqua simulations from the corresponding CRH quartiles. The shaded areas, Days 2-10, indicate the time in which the large-domain simulations have already spun up but do not yet self-aggregate.

large-scale moisture gradients due to features like fronts, as well as internally generated PW variability. As LASAM lacks the synoptic variability present in NGAqua, we should not expect self-aggregation in LASAM to be fully representative of NGAqua, and it is not. It is for that reason as well as conceptual simplicity that we base other parts of this paper on small-domain LASAM simulations that do not self-aggregate.

Turning to LASAM, the left column of Figure 2.11 compares Q1 cloud properties (cloud fraction, precipitation, and precipitable water) of the small-domain (64 km $\times$ 64 km) and large-domain (256 km $\times$ 256 km) simulations. The domain-mean vertical structures of the cloud fraction and condensates are quite insensitive to the domains size. Enlarging the domain size results in a slightly larger QN near the cloud base and slightly smaller QN near the cloud top, but it does not affect the other thermodynamic properties such as s_{li} and RH (not shown). Precipitation, PW and the self-aggregation index are shown on the right. Compared to NGAqua, LASAM underestimates the precipitation (Fig. 2.11b) but can represent the PW well (Fig. 2.11c). After a day of spin-up, all cloud statistics initially closely agree between the two domain sizes. However, the large-domain simulations start to self-aggregate after Day 10. The self-aggregation index increases from less than 0.02 to approximately twice this value (Fig. 2.11d). The large-domain CTL simulation self-aggregates more strongly than the 4K simulation, consistent with NGAqua, but takes much longer to reach this new equilibrium. The degree to which large-domain LASAM simulations self-aggregate and the timescales over which this happens vary greatly, depending on the SST, horizontal wind profile and advection scheme. For instance, just changing from the Q1 wind profile to a NGAqua subtropical-mean horizontal wind profile, which has weaker meridional winds, prevents aggregation with the control SST but not with the warmer SST, regardless of the clear-sky radiative heating rate and the choice of advection scheme.

Self-aggregation of the shallow cumuli in LASAM is accompanied by a slight increase of cloud fraction (Fig. 2.11a), increased cloud water path and hence a more negative SWCRE. The precipitation increases as the clouds self-aggregate (Fig. 2.11b). However, the domain-mean PW remains constant throughout the entire simulation (Fig. 2.11c), unlike in simula-

tions of deep convection for which domain-mean PW decreases once self-aggregation develops [10, 59].

2.5.2 Sensitivity to grid resolution

In addition to the cloud-system-resolving resolution used in NGAqua, we also run LASAM simulations with finer grid spacing typically used for LES studies of shallow cumuli. We ran a six-day high-resolution CTL simulation with 100×100×40 m grid resolution over a 6.4 km × 6.4 km domain with 115 vertical levels. This grid resolution is sufficient to adequately resolve shallow cumulus convection, based on past intercomparison studies [49]. Other LASAM simulations with coarser horizontal resolution (250 × 250 × 40 m with 115 vertical levels), and finer vertical resolution (100 × 100 × 20 m with 146 vertical levels) gave similar results. Figure 2.12 shows that the low cloud fraction is reduced 50% and the domain-mean cloud water path is reduced 75% compared to the 4 km control simulation (blue and green lines). The vertical structures of the cloud fraction and liquid water fields are also substantially different. This demonstrates that NGAqua's shallow cumulus population is considerably distorted by its coarse grid.

2.5.2.1 Sensitivity to SST and ΔR_{clr} in LES

We ran three additional high-resolution simulations, 4K, CTL+ΔRc and 4K-ΔRc, at 100×100×40 m using Q1 forcings with the MPDATA advection scheme to test the sensitivity of the LES to SST and R_{clr}. The sensitivities are similar to those with 4 km grid spacing. Figure 2.13a-c shows that their boundary-layer depth hardly changes with SST warming. The inversion strength increases by the same amount as in the coarser-resolution simulations (Table 2.5). The cloud fraction at cloud base increases (Fig. 2.13a), causing the shaded cloud fraction of the 4K simulation to be larger than the CTL (Fig. 2.10a). Increases in cloud water path and $\left|\text{SWCRE}\right|$ are small but statistically significant. Radiative cooling increases throughout the lower two-thirds of the boundary layer. In the the CTL+ΔRc simulation, cloud fraction and cloud water increase throughout the entire boundary layer relative to

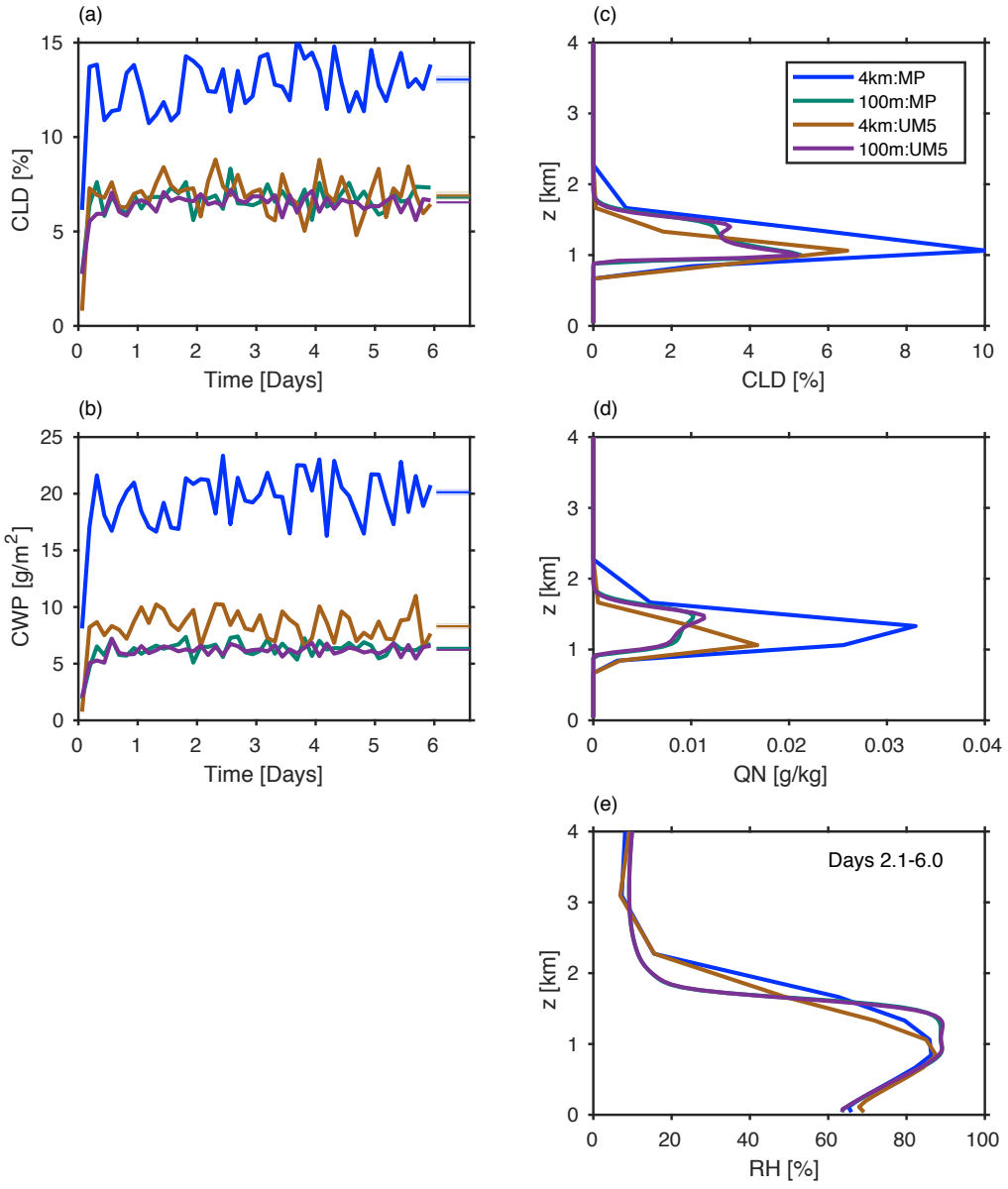

Figure 2.12: Sensitivity to grid resolution

The sensitivity to grid resolutions (4 km with 34 vertical layers and 100x10x40 m with 115 vertical layers) and advection schemes (MPDATA and UM5) of the LASAM Q1 control climate. The left column shows time series of (a) low-cloud fraction and (b) cloud water path of the four CTL simulations. The short horizontal lines and the shaded regions represent the time means and the $\pm 1\sigma$ error bars, as in Figure 2.7, but only for Days 2.1-6.0. The right column shows vertical profiles of (c) cloud fraction, (d) cloud liquid water and ice mixing ratio and (e) relative humidity averaged over these four days.

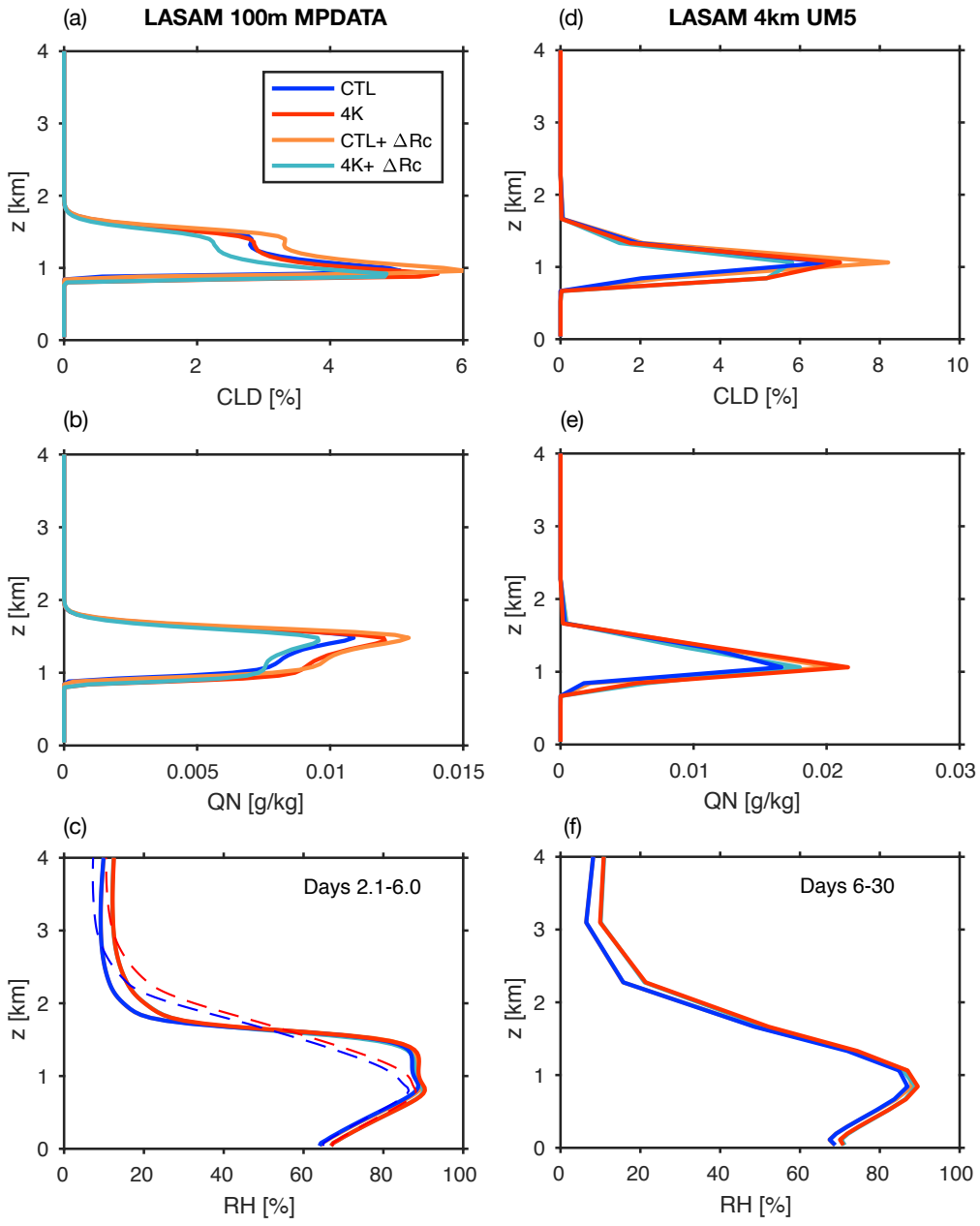

Figure 2.13: Sensitivity to SST and clear-sky radiative cooling using different resolution and advection scheme

The sensitivity to 4 K SST warming and enhanced boundary-layer clear-sky radiative cooling of the LASAM Q1 simulations with (a-c) $100\times100\times40$ m resolution and MPDATA advection scheme and (d-f) 4-km horizontal resolution and UM5 advection scheme. Vertical profiles of (a,d) cloud fraction, (b,e) cloud liquid water and ice mixing ratio and (c,f) relative humidity averaged over Days 2.1-6 and Days 6-30, respectively.

CTL; the 4K-ΔRc simulation shows the opposite response relative to 4K. The change in shaded cloud fraction due to clear-sky radiative cooling alone is even stronger than that caused by 4 K SST warming (Fig. 2.10a-c). Section 2.6 explores this response further.

2.5.2.2 Sensitivity to CO_2 and ΔR_{clr} in LES

We ran the CTL+4×CO2 and 4K+4×CO2 simulations at 100×100×40 m using Q1 forcings with the MPDATA advection scheme to test the sensitivity of the LES to the direct radiative effects of CO_2 quadrupling. The clear-sky radiative cooling change has the same sign and similar vertical structure as those with 4 km grid spacing, but the cloud reduction in response to quadrupled CO_2 alone is much stronger in the LES. (Table 2.5). The shaded cloud fraction and $\left|\text{SWCRE}\right|$ increase from CTL to 4K+4×CO2 is smaller in the finer-resolution simulations.

2.5.3 Sensitivity to advection scheme

We conducted CTL simulations using UM5 [63], a high-order scalar advection scheme available in SAM, using both the 4 km and 100×100×40 m grid resolutions. Figure 2.12 shows that the results are insensitive to the choice of advection scheme at high resolution, but highly sensitive at the 4 km resolution. At 4 km resolution, the UM5 scheme simulates cloud fraction and cloud water path that are much closer to the fine-resolution simulations than with MPDATA.

Similar to the experiments in Section 2.4, we also ran 4K, CTL+ΔRc and 4K-ΔRc simulations using 4 km resolution and the UM5 advection scheme. The results are shown in Figures 2.10 and 2.13d-f. Despite having much smaller cloud fraction and water path in the CTL simulation, the responses to SST and R_{clr} changes are qualitatively similar to those using the MPDATA advection scheme. Both schemes at 4 km resolution suggest an increase in shallow cumulus cloud in a warmer climate, while with fine resolution both schemes show smaller cloud fraction and water path increases in a warmer climate, similar to the results of Blossey et al. (2009) and Parishani et al. (2018) [2, 43]. This mandates

caution in assuming that low cloud feedbacks from a 4 km resolution global simulation will be quantitatively similar to those from a fine-resolution simulation which fully resolves the eddies that generate the boundary-layer clouds.

2.5.4 Sensitivity to nudging in the cloud layer

We conducted two additional sets of simulations in which the temperature and humidity profiles are not nudged below 2.5 km, using both 4 km and 100×100×40 m resolutions. The 4-km un-nudged simulations were run until Day 60 like their nudged counterparts. The un-nudged 100-m simulations were run until Day 10 and the results from Days 6-10 are used in the analysis. Although the cloud fraction and the other radiative properties of the un-nudged 100×100×40 m simulations reach a steady state by Day 5, the cloud water path still continues to slowly decrease thereafter.

The vertical profiles of the cloud fraction, ΔR_{clr} and RH from the un-nudged simulations are shown as solid lines in Figure 2.14. As expected, the vertical structures in the un-nudged simulations drift away from those in NGAqua, but the simulations still predict similar responses to warmer SST, including the clear-sky radiative cooling change. They have a shaded cloud fraction increase with warming, but smaller than their nudged counterparts (Table 2.5). The cloud layer shallows slightly with SST warming. In contrast, when forced by enhanced boundary-layer clear-sky radiative cooling alone, the cloud-top height of both un-nudged simulations increases slightly compared to their control cases (not shown), deepening the cumulus layer and causing the shaded cloud fraction of CTL+ΔRc to be greater than 4K. The shaded cloud fraction and cloud water path increases are just as strong or stronger than the nudged simulations. Finally, the cumulus layer in an un-nudged 4K-ΔRc simulation shallows even more than for 4K and has the least cloud fraction among all of these four un-nudged cases. The cloud layer shallows when both the 4-km and 100-m resolutions are used. This implies that although the grid resolution used in NGAqua and the default LASAM simulations is not ideal for resolving shallow convection, it can still qualitatively capture vertical structure changes.

In summary, the fractional increases in shallow cumulus cloud in response to 4 K SST warming and ΔR_{clr} observed in LASAM simulations are not an artifact of nudging the temperature and moisture profiles. By constraining the inversion height, nudging does affect the cloud layer depth and the magnitude of the cloudiness changes. We stick to analyzing the nudged runs since by design they maintain an inversion height and vertical cloud structure that compare more closely to NGAqua.

2.6 Discussion

So far, we have shown that the shallow cumulus cloud increase with ΔR_{clr} in LASAM is robust and independent of the choice of model grid resolutions, nudging and advection schemes, and that enhanced boundary-layer ΔR_{clr} in isolation can explain most, if not all, of the cloud fraction and water path increase observed in the 4K simulation. This section uses a boundary-layer heat (more precisely, s_{vl}) budget to further illuminate how enhanced ΔR_{clr} increases cloud cover. It also compares the effects of ΔR_{clr} alone with other competing effects of the SST warming on the cloudy boundary-layer energetics and structure.

We consider the boundary-layer s_{vl} budget. Here, s_{vl} is a good variable to use not only because of its connection to buoyancy, but because (as we will see below) its surface flux happens to be insensitive to warming of the climate system. Thus its boundary-layer budget is mostly sensitive to other source terms like radiation, entrainment and advection.

Recall from Figure 2.8e-f, the base of the inversion layer or z_{ib} is located where the RH reduces sharply with height. In LASAM, this is the same level as where the stratification of s_{vl} is the strongest and the domain-mean turbulent 'entrainment' flux of s_{vl} is most negative. Let $\langle f(z)\rangle = \int_0^{z_{ib}} \overline{\rho}(z) f(z)\, dz$ denote a mass-weighted integral of any function $f(z)$ evaluated between the surface and z_{ib}. The boundary-layer s_{vl} budget is balanced by the following terms:

$$\underbrace{\frac{\partial \langle s_{vl}\rangle}{\partial t}}_{\text{Storage}} = \underbrace{F^{\downarrow}_{s_{vl}}}_{\text{Cloud-top flux}} + \underbrace{F^{\uparrow}_{s_{vl}}}_{\text{Surf. flux}} + \underbrace{\langle R\rangle}_{\text{Rad.}} + \underbrace{\langle A_H\rangle + \langle A_V\rangle}_{\text{Large-scale advec.}} + \underbrace{\langle L_{vl}\Delta P\rangle}_{\text{Prec. warm.}} + \underbrace{\langle N\rangle}_{\text{Nudging}} . \tag{2.4}$$

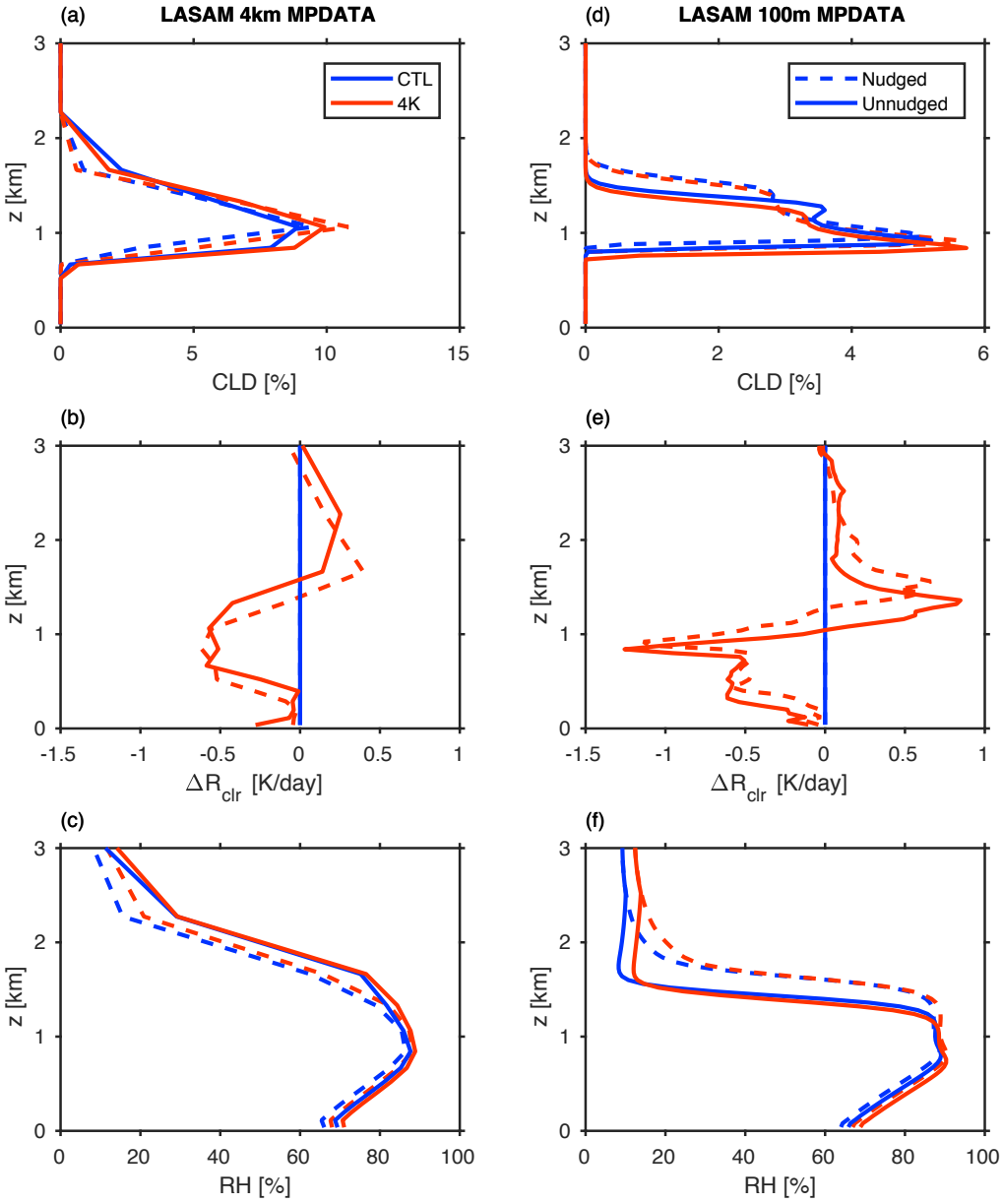

Figure 2.14: Sensitivity to nudging of heat and moisture in the cloud layer

The sensitivity to s_{li} and q_t nudging. The left column shows the profiles of (a) cloud fraction, (b) the change in clear-sky radiative heating rate with respect to CTL (ΔR_{clr}), and (c) relative humidity of the 4-km resolution simulations, averaged from Days 11-60 for both with and without nudging. The results for 100x10x40-m resolution are shown in (d)-(f), averaged from Days 2.1-6.0 for the nudged simulations and Days 6.1-10 for the un-nudged simulations. The solid lines show the simulations un-nudged below 2.5 km, while the dashed lines represent the nudged simulations shown in Figures 2.8 and 2.13a-c.

In a steady state, the storage term $\partial\langle s_{vl}\rangle/\partial t$ is approximately zero. The downward entrainment flux at the inversion base is $F^{\downarrow}_{s_{vl}} = -\overline{\rho}\overline{w's'_{vl}}(z_{ib})$, while the upward surface flux is $F^{\uparrow}_{s_{vl}}$. The boundary-layer full-sky radiative flux convergence is $\langle R\rangle$. The large-scale horizontal advective tendency is $\langle A_H\rangle = -\langle\overline{\mathbf{u}_h \cdot \nabla_h s_{vl}}\rangle$, and the large-scale vertical advective tendency is $\langle A_V\rangle = -\langle\overline{w}\partial\overline{s}_{vl}/\partial z\rangle$. The precipitation warming is $\langle L_{vl}\Delta P\rangle$, where $\Delta P = P(z_{ib}) - P(0)$ is the difference in precipitation between z_{ib} and the surface and $L_{vl} = L_v - 0.61c_pT_{ref}$. Finally, $\langle N\rangle$ is the s_{vl} nudging tendency which is zero in the boundary layer for the un-nudged simulations discussed in Section 2.5.4.

The terms on the right hand side of Equation 2.4 for the CTL simulations are shown in Figure 2.15a; upward bars show s_{vl} sources and downward bars show sinks. Their responses to the enhanced boundary-layer $R_{\rm clr}$ alone and the additional thermodynamic changes associated with 4 K SST warming are presented in the subsequent panels. Figure 2.15d-f shows corresponding plots for low cloud fraction. In LASAM, the boundary-layer s_{vl} budget is kept in balance by compensating changes in three main terms: $\langle R\rangle$, $\langle A_H\rangle$, and the downward entrainment flux $F^{\downarrow}_{s_{vl}}$.

Figure 2.15b shows that the perturbed-radiation simulation CTL+ΔRc has stronger $\langle R\rangle$ by $\sim$6 W/m^2 than in CTL. At least half of this is balanced by more warming due to stronger entrainment flux $F^{\downarrow}_{s_{vl}}$ associated with increased cumulus cloud amount (Fig. 2.15e). The nudging tendency is not trivial for the CTL+ΔRc simulations and plays a role in the sensitivities of the nudged simulations to radiative cooling by suppressing inversion height changes. However, because the nudging tendency change is positive like the entrainment flux change, we can deduce that nudging does not artificially drive the entrainment flux increase in LASAM. Indeed, entrainment flux increases more in the un-nudged simulations than in their nudged counterparts. The changes from 4K-ΔRc to 4K are similar (not shown). The changes from CTL+ΔRc to 4K encompass the rest of the thermodynamic effects of 4 K SST warming (Fig. 2.15b-c). By construction, $\langle R\rangle$ does not change much, but the large-scale horizontal advective cooling $\langle A_H\rangle$ becomes less negative by $\sim$3 W/m^2 because the mean wind weakens in the warmer climate. The 4K entrainment flux $F^{\downarrow}_{s_{vl}}$ becomes weaker than in

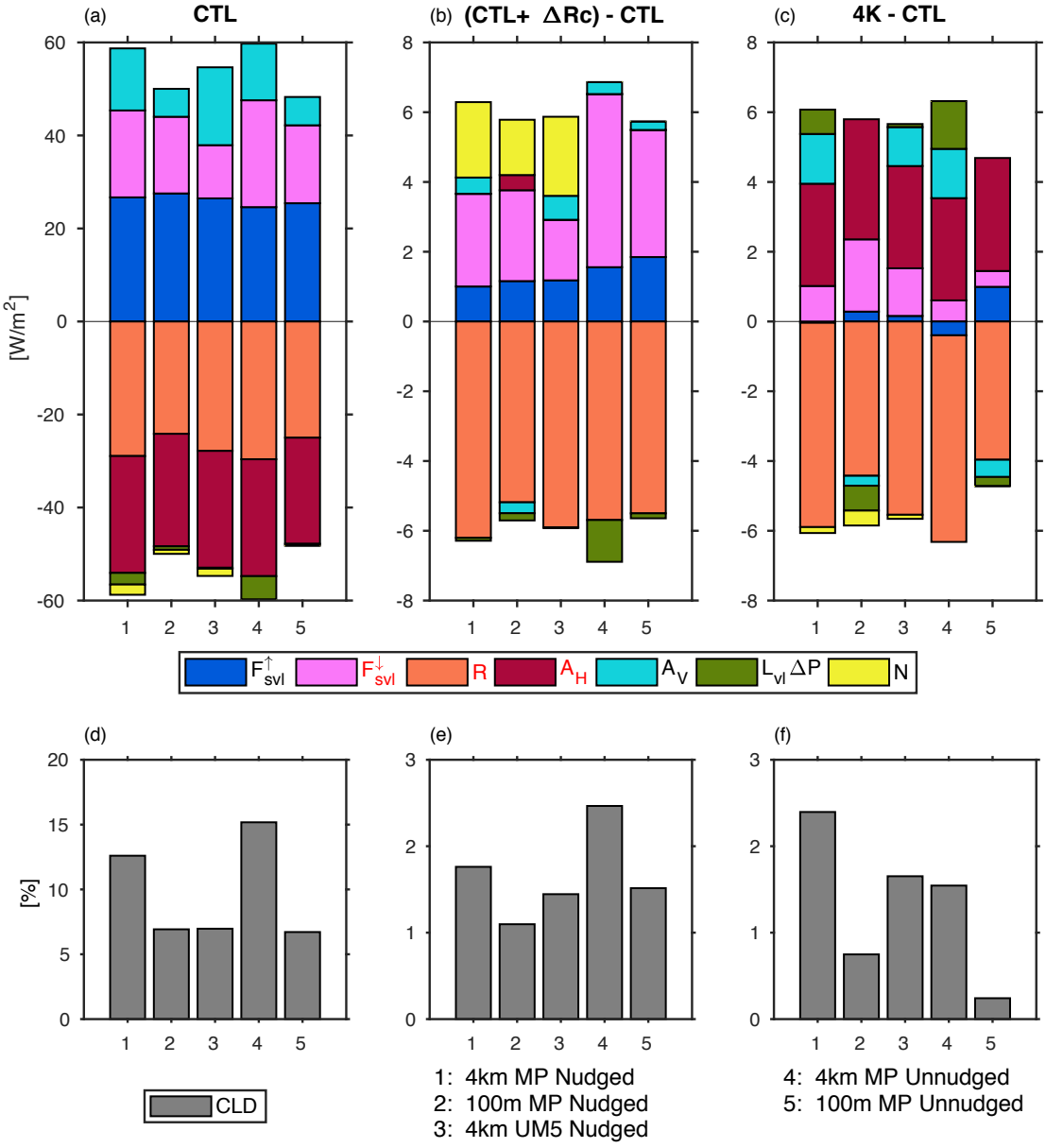

Figure 2.15: Boundary-layer-integrated s_{vl} budget analysis

The terms on the right hand side of the boundary-layer-integrated s_{vl} budget (Equation 2.4) during the quasi-steady state period of (a) the CTL simulations, (b) the responses to the radiation-only perturbation, and (c) the additional responses to the rest of the thermodynamic changes associated with 4 K SST warming. The corresponding plots for low-cloud fraction are shown in panels (d-f). The dominant processes balancing the cumulus-topped boundary-layer s_{vl} budget of the 4 km nudged (default) simulations are highlighted in red in the legend. The five LASAM cases are indicated on the bottom of the figure.

CTL+ΔRc in compensation for the reduced advective cooling.

Figure 2.16 shows relationships between $\langle R \rangle$, $F^{\downarrow}_{s_{vl}}$ and shallow cumulus cloud fraction. The cloud fraction, which is well correlated with the updraft cloud mass flux (Fig. 2.17b), increases with enhanced boundary-layer radiative cooling (solid lines) and the associated increase in entrainment flux $F^{\downarrow}_{s_{vl}}$, regardless of the choice of advection scheme and grid resolution. In response to the rest of the thermodynamic changes associated with SST warming (dotted lines), entrainment flux and (with two exceptions) cloud fraction are reduced. Figure 2.17a-b shows the vertical velocity variance and the updraft cloud mass flux also weaken. Finally, the response from CTL to 4K is approximately a linear superposition of the responses to the radiation and thermodynamic perturbations. Because the 4K cloud increase compared with CTL is not seen in 4K-ΔRc, it is reasonable to attribute that cloud increase to the 4 K radiative cooling increase.

Similar results are seen in the high-resolution simulations, except the thermodynamically driven reductions of the vertical velocity variance and updraft cloud mass flux are as strong as the radiatively driven increases (Fig. 2.17c-d).

Changes in radiative cooling rate in the lower boundary layer affect shallow cumulus clouds not only when the SST warms, but also when the direct radiative effects of quadrupled CO_2 are added. This weakens radiative cooling throughout the cloud layer, reducing the entrainment heat flux and vertical velocity variance and shallowing the boundary layer. However, the CO_2 quadrupling has less radiative impact at and below cloud base than the humidity increase due to 4 K SST warming, so the latter dominates the overall low cloud fraction change in LASAM.

We summarize the results of enhanced radiative cooling associated with 4 K SST warming in Figure 2.18. The three dominant processes balancing the boundary-layer s_{vl} budgets, $\langle R \rangle$, $\langle A_H \rangle$ and $F^{\downarrow}_{s_{vl}}$, are represented by wavy, horizontal and circular arrows shown in blue for the CTL simulation (Fig. 2.18a). As the SST warms (Fig. 2.18d), the penetrative entrainment flux strengthens (larger red circular arrows) to balance stronger boundary-layer radiative cooling (larger red wavy arrow) partly countered by weaker horizontal advective cooling

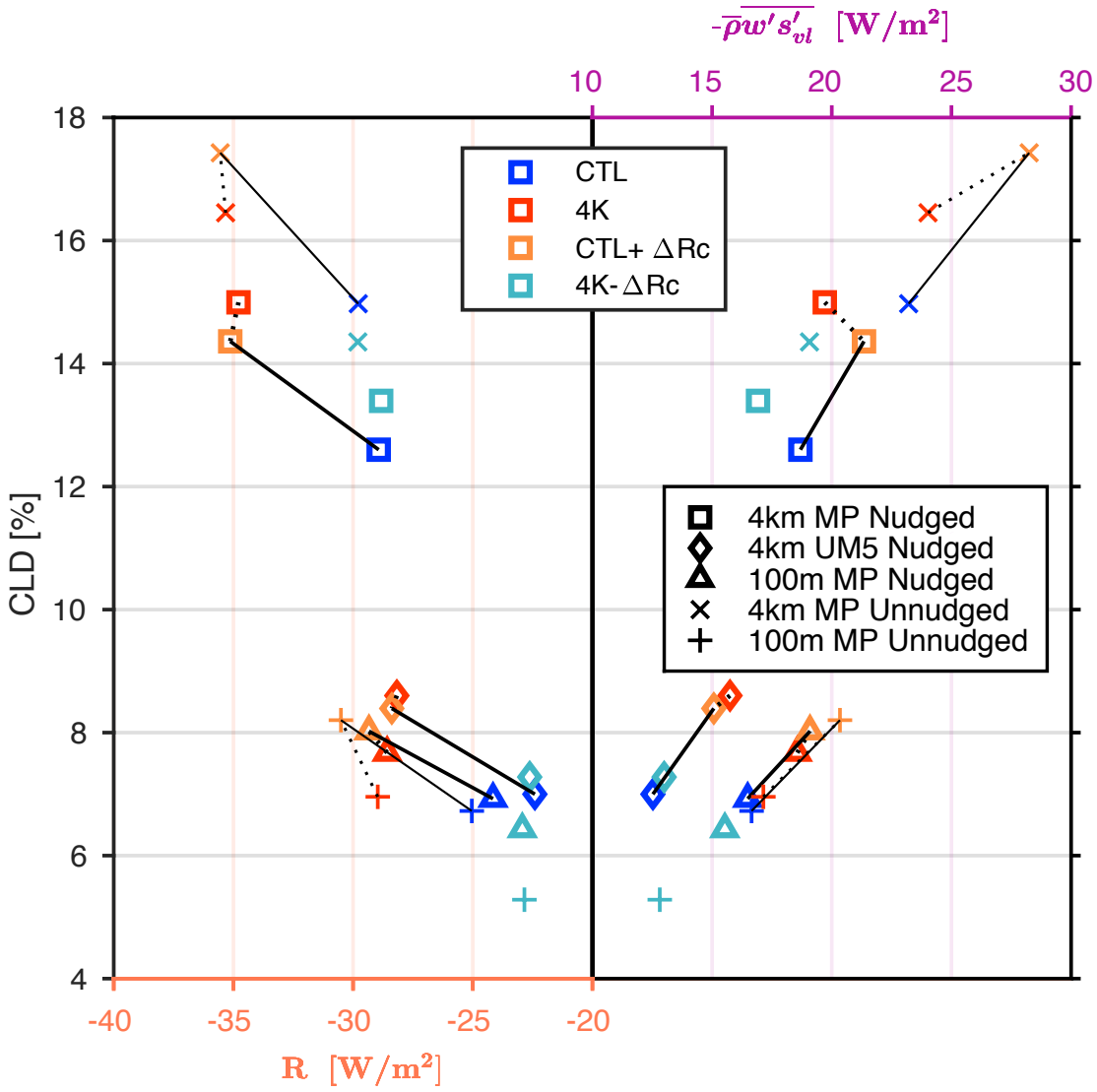

Figure 2.16: Cloud fraction vs. boundary-layer-integrated radiative cooling and cloud-top s_{vl} flux

Scatterplots of low-level cloud fraction vs. $\langle R \rangle$ (left axis, bottom panel) and $F^{\downarrow}_{s_{vl}}$ (right axis, upper panel) of the simulations shown in Figure 2.15. The solid lines connecting between the CTL to CTL+ΔRc simulations indicate changes from enhanced boundary-layer radiative cooling alone. The dotted lines connecting between the CTL+ΔRc to 4K simulations indicate the rest of the thermodynamic changes associated with 4 K SST warming including weaker advective cooling.

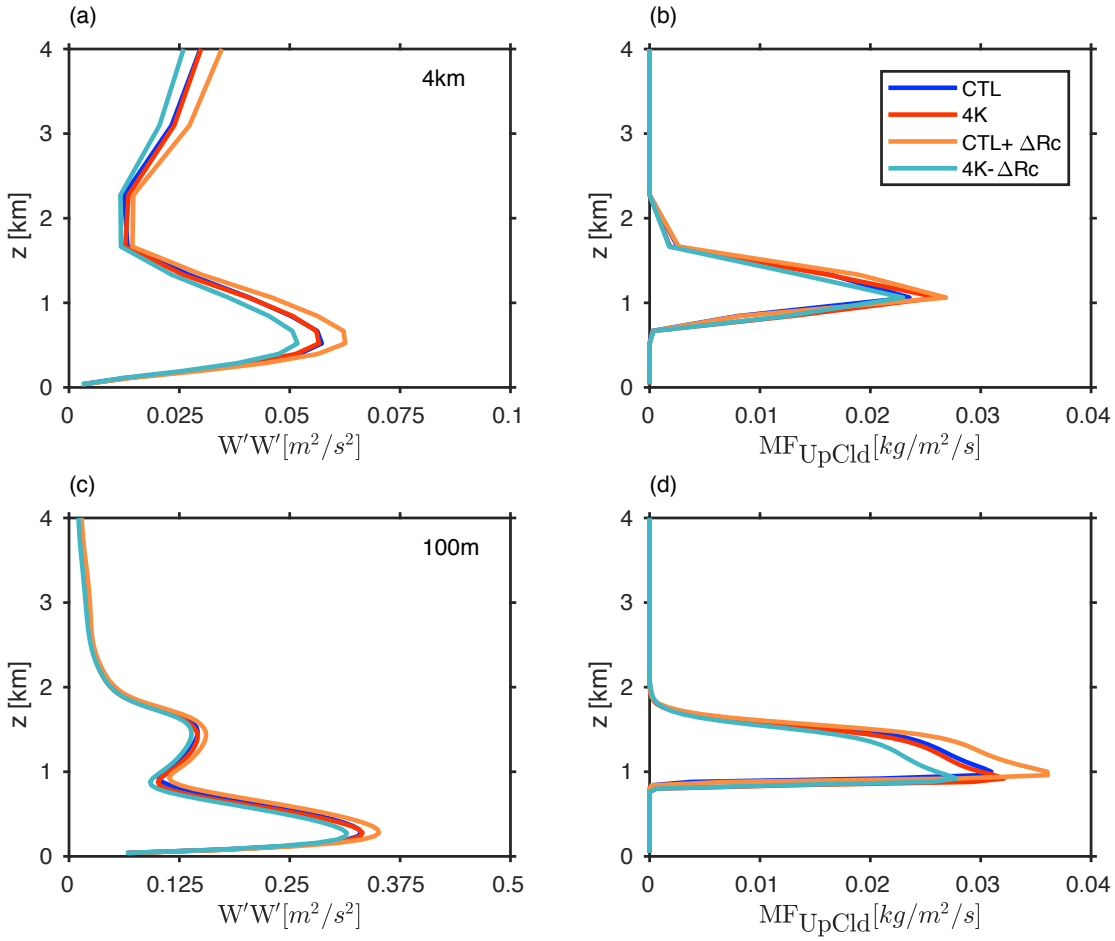

Figure 2.17: Vertical profiles of updraft cloud mass flux (MF_{UpCld}) and vertical velocity variance ($w'w'$) from LASAM 4-km and 100 × 100 × 40-m simulations

Vertical profiles of (a) vertical velocity variance ($w'w'$) and (b) updraft cloud mass flux (MF_{UpCld}) of the LASAM 4-km MPDATA nudged simulations (default) from Days 11 to 60. Panels (c-d) are as in Panels (a-b) but for the LASAM 100 × 100 × 40-m MPDATA nudged simulations, from Days 2 to 6.

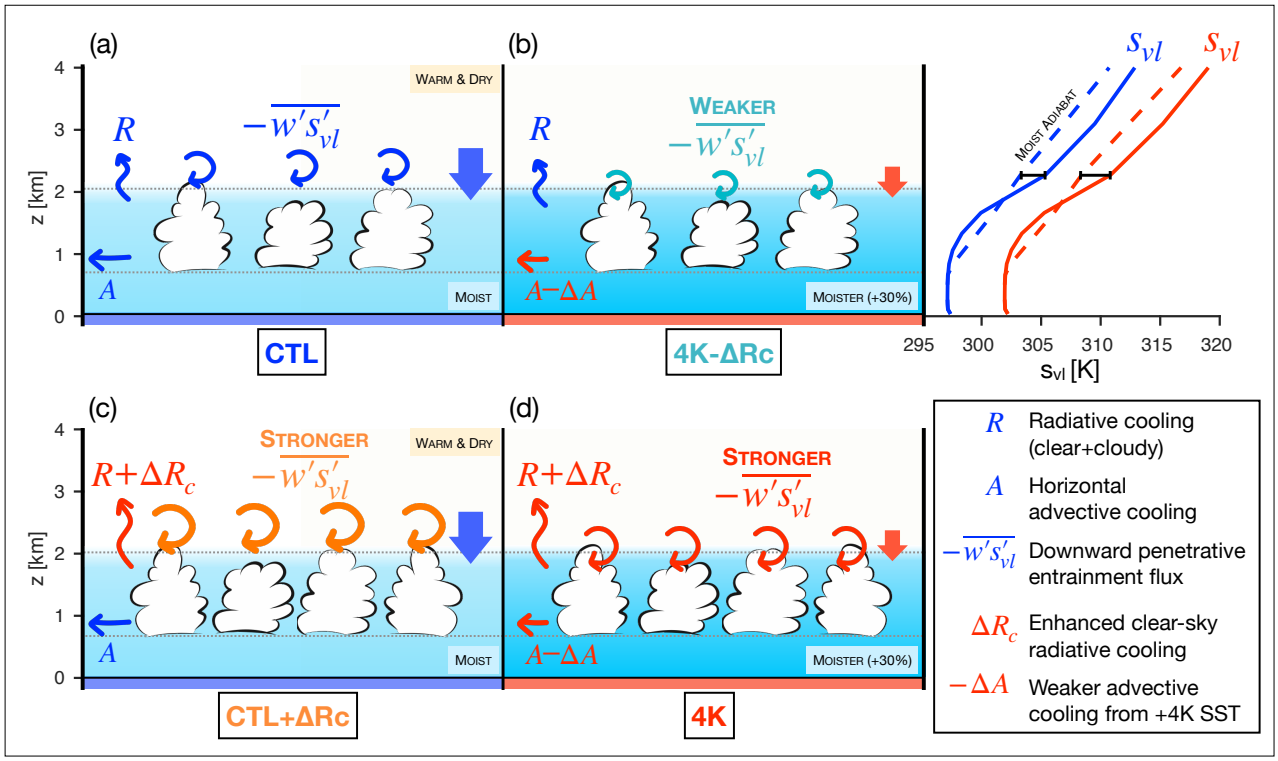

Figure 2.18: A schematic of the dominant processes that balance the cumulus-topped boundary layer s_{vl} budget in LASAM simulations

Dominant processes balancing the cumulus-topped boundary layer s_{vl} budget in the (a) CTL, (b) 4K-ΔRc, (c) CTL+ΔRc, and (d) 4K simulations. Changes in the full-sky boundary-layer radiative cooling (R) are mainly balanced by changes in cumulus penetrative entrainment flux ($-\overline{\rho}\overline{w's'_{vl}}$) and (for SST change) horizontal advective cooling (A). More radiative cooling drives more cumulus cloud. The s_{vl} profiles of the CTL and 4K simulations are shown on the upper right (solid), together with the moist adiabats (dashed) and horizontal black lines showing the inversion strength relative to a moist adiabat, which is stronger for warmer SST. The subsidence rate, represented by a stubby arrow, is weaker for warmer SST. See text for details.

(smaller red horizontal arrow). The perturbed-thermodynamics simulation 4K-ΔRc (Fig. 2.18b) has the same boundary-layer radiative cooling but weaker net advective cooling than the CTL, balanced by a weaker entrainment s_{vl} flux. The perturbed-radiation simulation CTL+ΔRc (Fig. 2.18c) has stronger radiative cooling than CTL, and similarly for the 4K vs. 4K-ΔRc simulations. In both of these cases the increased radiative cooling leads to more cumulus cloud and stronger entrainment s_{vl} flux. Figure 2.18 also shows the CTL and 4K s_{vl} profiles at the upper right, showing their similar inversion depths but slightly larger 4K inversion stability. The warmer cases also have a weaker subsidence rate (stubby downward-pointing arrows).

While the enhanced ΔR_{clr} destabilizes the boundary-layer, driving stronger cloud-top entrainment flux and causing low-cloud fraction increase in our simulations, other factors associated with 4 K SST warming including the weaker large-scale horizontal advective cooling can partly counteract the radiative cooling increase without increasing cloud fraction. An important effect that does not enter our simulations is stronger precipitation warming, which is found to be important in simulations of deeper shallow cumuli that precipitate [3, 56].

2.7 Conclusions

The response of subtropical marine shallow cumulus clouds to greenhouse warming is a major contributor to uncertainty in climate sensitivity. Cloud-resolving simulations of a near-global tropical channel on an aquaplanet (NGAqua) show an unexpected increase in subtropical shallow cumulus cloud fraction in response to 4 K SST warming [39]. Here, we used a limited-area version of SAM, LASAM, to reproduce this negative subtropical cloud feedback. LASAM is carefully configured to accurately represent the shallow cumulus cloud regime in the large-scale subsidence region of NGAqua. It uses the same cloud-resolving model with the same grid spacing, model physics and advection scheme as NGAqua. To obtain a pure shallow cumulus regime with minimal precipitation and deeper convection, we select the driest quartile of daily-mean mesoscale blocks in NGAqua. Steady advective forcings, SST, temperature and wind profiles input to LASAM are averages over this regime.

Strong wind nudging and weak temperature and humidity nudging keep LASAM close to the target NGAqua atmospheric state. This methodology broadly follows Blossey et a. (2009) [2], adapted for the use with NGAqua instead of a superparameterized real-geography climate model. So configured, LASAM captures much of the cloud fraction and cloud water increase in NGAqua due to 4 K SST warming.

LASAM sensitivity studies suggest that the cumulus cloud increase is primarily driven by stronger clear-sky boundary-layer radiative cooling caused by higher absolute boundary-layer humidity in the warmer SST scenario, partly counteracted by the direct radiative effects of increased CO_2. The enhanced clear-sky boundary-layer radiative cooling destabilizes the boundary layer and drives stronger entrainment heat flux, accomplished by more cumulus clouds. Increased free-tropospheric RH right above the inversion also drives about a quarter of the cloud fraction increase. Increased CO_2 shallows the boundary layer with little net impact on cumulus cloud cover. SST warming has numerous other important effects on the simulated shallow cumulus layer, including weaker large-scale horizontal advective cooling tendency in the boundary layer, weaker subsidence and surface wind speed, stronger dry static stability in and above the cumulus layer, a larger vertical humidity gradient and more latent heat flux.

This response contrasts with the radiative response of stratocumulus clouds to a warmer, moister (and/or more CO_2-rich) overlying free troposphere. In that case, the boundary layer already has a high infrared optical thickness due to the stratocumulus layer, and the more emissive free troposphere reduces radiative cooling of the boundary layer, which all occurs from the cloud top. Our simulations suggest that this difference in physics can reverse the sign of the local low cloud feedback from positive in a stratocumulus regime to negative in a nearly non-precipitating shallow cumulus regime. For cumulus layers deep enough to precipitate significantly (1 mm/day or more), the results of Blossey et al. (2013) [3] suggest that in a warmer climate, the radiative cooling increase can instead be balanced by the latent heating from a precipitation increase rather than destabilizing the cumulus layer and leading to more cloud, resulting in nearly neutral or slightly positive low cloud feedback.

These LASAM analyses were performed using a small 64×64 km domain, to inhibit mesoscale organization of shallow cumulus convection. In a larger domain, e.g. 256×256 km, the shallow cumuli typically self-aggregate after 10 days or more, after which the cloud fraction and water path increase slightly. Although these changes are smaller than the impacts of SST, clear-sky radiative cooling or free-tropospheric RH, they quantitatively affect LASAM's simulated cloud response to changed forcings. The extent to which shallow cumuli self-aggregate in LASAM is sensitive to the domain size, the horizontal wind profiles and the SST, and bears no obvious relationship to the degree of mesoscale aggregation seen in this cloud regime in NGAqua.

These simulations are also sensitive to the grid resolution and the scalar advection scheme. Switching from the MPDATA to the UM5 scalar advection scheme, or use of a finer grid appropriate for shallow cumulus simulations, i.e. $100 \times 100 \times 40$ m, halves cumulus cloud cover and modifies its vertical structure. However, like the default LASAM and NGAqua, all of these simulations show increased subtropical shallow cumulus cloud with 4 K SST warming (lessened when the finer LES-like resolution is used), and clear-sky radiative cooling change explains most or all of their cloud fraction increase.

Our results point to the need for further studies with high-resolution models of shallow cumulus cloud feedback that more fully elucidate its sensitivity to cloud-layer depth, microphysical assumptions, mesoscale organization, wind shear, and the structure and dynamics of the overlying free troposphere. These studies need to be backed up with careful observational testing of such models, for which recent and upcoming field programs sampling shallow subtropical cumulus convection should be an invaluable resource.

Chapter 3

THE ROLE OF MULTISCALE INTERACTION IN TROPICAL CYCLOGENESIS AND ITS PREDICTABILITY IN NEAR-GLOBAL AQUAPLANET CLOUD-RESOLVING SIMULATIONS

3.1 Introduction

Tropical cyclogenesis (TCG) is a multiscale process that has long been challenging to predict. In the past decades, the track predictability has improved but the challenges in genesis and intensity forecasts still remain. Tropical cyclones (TCs) are systems of rotating storms that form over warm tropical oceans, spanning over hundreds of kilometers yet consisting of numerous small-scale deep convection. TCs draw their energy from various sources. Gray (1968, 1979) summarized six necessary conditions for TCG: warm sea surface temperature (above 26.5°C), atmospheric instability, high lower-to-mid-tropospheric humidity, sufficient planetary vorticity (or Coriolis parameter or f), pre-existing low-level disturbances, and little vertical wind shear [26, 27]. However, having all these conditions met does not guarantee that TCG will occur. This explains why not every tropical moist convection becomes a TC despite being in an environment with favorable conditions.

Raymond et al. (2015) discusses two environmental factors that help modulate tropical oceanic convection and are crucial for TCG [45]. First, deep convection and hence precipitation tend to favor regions of high column relative humidity (CRH), the ratio between precipitable water (PW) and the PW the atmosphere would have if it is saturated. With higher CRH, deep convective updrafts do not have to fight as much entrainment drying and evaporative cooling as in the low-CRH environment. Second, vertical vorticity has a strong interaction with convection and precipitation. A cyclonic vortex in gradient wind and hydro-

static balances has low pressure at the center, requiring an anomalously stable lapse rate with warm air above. This may affect the vertical structure of cumulus convection. Convection in turn releases latent heat that can drive mid-level upward motion and lower-tropospheric vortex stretching. These factors all affect the early development of a TC.

We contrast two scales of atmospheric interactions that lead to TCG: The convective scale vs. the planetary scale. The convective-scale process, sometimes referred to as a 'top-down' TCG pathway, focuses on a convective precursor, such as a pre-existing mesoscale convective system (MCS) that spins up a mid-level cyclonic vortex (MCV) in the stratiform region. The latent heating in the upper troposphere where stratiform clouds are present and evaporative cooling in the lower troposphere where precipitation is present result in the adjustment of pressure surfaces above and below the MCV. The resultant low-level convergence drives vertical motion and creates vortex stretching [16], which eventually leads to TCG. Surface fluxes can also destabilize the lower troposphere and help convection develops upward into the MCV [1]. The resultant vortex stretching and the redevelopment of convection helps generate vorticity that extends upward to the MCV.

The term 'vortical hot tower' (VHT) was introduced by Hendricks et al. (2004) to describe this narrow area of cumulonimbus with strong positive vorticity anomaly which now has a warm core due to convective latent heating [29]. The strong tangential wind associated with the VHT serves as a protection for the inner area of high convective instability from lateral entrainment of the outer, drier air, enhancing the latent heating in the center of the vortex, which spins it up faster [36]. VHTs can further superimpose with one another and grow into TCs [36, 54]. In addition, recent studies have shown that a broad circulation that leads to a spontaneous TCG goes through similar processes as self-aggregation and radiative feedback is crucial for the organization of the convection [41, 58]. As the system spins up, the surface-wind can induce stronger surface heat fluxes that feed moisture to the vortex system and help it intensify in a shorter period of time [37, 19]. In other words, the feedback between surface wind and surface heat flux helps a TC reach its maximum intensity.

The planetary-scale process, or the 'bottom-up' TCG pathway, emphasizes the role of

pre-existing large-scale lower-tropospheric vorticity disturbances that organize and then are amplified by convection. For example, in the northern hemisphere, an easterly flow in the subtropics and a westerly flow associated with the Intertropical Convergence Zone (ITCZ) provides a region of strong meridional wind shear in the lower troposphere that is favorable for cyclonic motions in the southern part of the easterly jet maximum. The ITCZ convection feeds back to the meridional wind shear of zonal flows, and helps stretch the positive vorticity in the area where convection is present. A reversal of meridional absolute vorticity gradient and the convection feedback altogether satisfy a necessary condition for barotropic instability, helping a tropical disturbance draws energy directly from the mean flow [14, 23]. As a result, strips of low-level absolute vorticity maxima form north of the ITCZ. They break down into cyclonic vortices, which are initially zonally elongated and later axisymmetrize. One or multiple vortices can intensify into TCs given suitable environmental conditions.

A schematic of the barotropic instability associated with off-equatorial ITCZ and an easterly jet is shown in Figure 2 of Dunkerton et al. (2009) [21]. At the critical layer, where the speed of the zonal mean flow equals the wave speed, the air is trapped inside a "Kelvin cat's eye," a region of cyclonic flow that acts as a "pouch" containing the moisture and preventing the air inside from exchanging with the drier environmental air [21, 53]. Dunkerton et al. (2009) called this the "marsupial paradigm" because the pouch acts as a protection for the moist air inside the vortex.

Although the planetary-scale pathway emphasizes the importance of the ITCZ and subtropical easterly flows in creating cyclonic vortices, it recognizes that deep convection energizes the vortices further, leading to vertical stretching of absolute vorticity, just as the convective-scale pathway does. These theories have different emphases but are not entirely mutually exclusive, as both involve positive feedbacks between vorticity and convection. As Gjorgjievska and Raymond (2014) point out, these two pathways might be two pieces of the same puzzle. Processes leading TCG involve multiscale interactions between both large-scale circulations and small-scale tropical convection [25].

Therefore, high-resolution simulations that can be run over a global or near-global domain

allow both processes to be studied at the same time. A near-global cloud-resolving simulation (NGAqua), which is a cloud-resolving model based on the System of Atmospheric Modeling or SAM [30], was configured and can simulate tropical convection and large-scale circulations realistically. NGAqua has 4-km horizontal grid spacing with sea-surface temperature (SST) and planetary vorticity that vary with latitudes. The NGAqua simulations analyzed by Bretherton and Khairoutdinov (2015) and Narenpitak et al. (2017) have the SST maximum at the equator [11, 39]. They produce realistic tropical cloud and circulation, but do not produce TCs.

The NGAqua simulations presented in this chapter uses the same SST distribution but shifted northward such that the SST maximum is at 15°N. The sufficient SST and planetary vorticity as well as barotropic instability north of the ITCZ allow TCs to spontaneously spin up in NGAqua. In this chapter, we define a cyclonic vortex with minimum surface pressure (PSFC) below 1000 hPa but above 990 hPa as a tropical depression. A cyclonic vortex with PSFC between 980 hPa and 990 hPa is referred as a tropical storm. Finally, a cyclonic vortex with PSFC below 980 hPa is considered a TC. Hence, the TCG and vorticity spin-up process discussed for the rest of this chapter refer to the period which the PSFC of a cyclonic vortex or a tropical depression deepens below 980 hPa.

Section 3.2 discusses the simulation setup further and introduces the ensemble of three NGAqua simulations for a predictability study. Section 3.3 provides a brief discussion of the general circulation of these simulations, which resemble the autumn equinox of the Eastern Pacific Ocean. Section 3.4 discusses large-scale processes associated with the ITCZ breakdown and introduces a tracking algorithm that is developed for examining the genesis and the intensification of the TCs in NGAqua. Section 3.5 analyzes the vorticity budget associated with a cyclonic vortex and focuses on the small-scale convective processes relevant to TCG. Section 3.6.1 discusses the predictability of the TCG in NGAqua and provides two case studies. Finally, Section 3.7 presents the conclusions.

3.2 Simulation Setup

3.2.1 NGAqua Tropical Cyclone or 'TC1' Simulation

The NGAqua modeling framework is based on version 6.10.6 of the System of Atmospheric Modeling (SAM) CRM [30] and was first described by Bretherton and Khairoutdinov (2015) [11]. It is a near-global tropical-channel aquaplanet CRM with 4-km horizontal resolution and 32 vertical layers (with 12 vertical levels below 3 km), spanning a 20,480 km x 10,240 km domain that is zonally periodic, with walls on the northern and southern boundaries. The Coriolis parameter and SST are dependent on the latitude. Perpetual-equinox diurnal variation of insolation is applied synchronously at all longitudes, such that it is noon at the same time over the entire domain. NGAqua does not depend on any convective parameterization. It uses the original SAM single-moment bulk microphysics scheme [30], the Community Atmospheric Model 3 (CAM3) radiation scheme [17] with interactive radiation, multidimensional positive definite advection transport algorithm (MPDATA) monotonic advection scheme [50], and a Smagorinsky-type turbulent kinetic energy scheme. Readers are referred to Bretherton and Khairoutdinov (2015) and Narenpitak et al. (2017) for further details of NGAqua's model configuration and spin-up process [11, 39].

The control NGAqua simulation (CTL) described in previous studies assumes a CO_2 concentration of 355 ppm and the zonally and hemispherically symmetric QOBS SST specification of the Aqua-Planet Experiment (APE) intercomparison [40], which ranges from 27°C (or 300 K) at the equator to approximately 5°C (or 278 K) at the poleward boundaries:

$$\mathrm{SST}(^\circ\mathrm{C}) = 27 \times \frac{\cos^2(\mathrm{lat}/60^\circ) + (\cos^4(\mathrm{lat}/60^\circ)}{2}.$$

The latitudes of the CTL simulation extend from 46°S to 46°N. It produces a zonally symmetric Hadley-Cell-like meridional circulations with the ITCZ centered at the equator, but does not produce TCs or any TC-like disturbances.

NGAqua can produce TCs when this same SST distribution is shifted northward 15°, as shown in Figure 3.1a. The so-called 'TC1' simulation's latitudes extend from 31°S to

61°N. The warm SST latitudinal bands coincide with regions of sufficiently strong positive planetary vorticity, permitting vortex formation that could lead to TCs. In this chapter, we will follow the evolution of convection and vorticity in and around pre-TC disturbances in TC1. After the TC1 simulation has reached an approximate statistical equilibrium (referred to as Day 0), it is run further for 20 days and the outputs are used for analyses in this chapter.

3.2.2 Perturbed 'TC2' and 'TC3' Simulations

To study the predictability of TCG during the first ten days of the simulations, two other 20-day simulations 'TC2' and 'TC3' are branched off the TC1 simulation after it has reached an equilibrium. At Day 0 of each of these simulations, the TC1 simulation's humidity field (q_v or water vapor mixing ratio) at 700 hPa is perturbed with 0.1 g/kg white noise throughout the entire domain, with no changes to the temperature and wind fields. The perturbations are allowed to grow as the simulations evolve.

The locations and times of TC formation remain similar among these three simulations until Day 10, by which time the domain-mean root-mean-squared perturbation PW reaches 50% of the maximum value. We will use these simulations to investigate the predictability of TCG.

3.3 General Circulation in NGAqua TC1 Simulation

The rest of Figure 3.1 shows zonal-time-mean fields from TC1 simulations during the first eight days. Figures 3.1b and 3.1c show the surface precipitation (Prec) and the liquid water and ice cloud condensates (q_n), respectively. The TC1 simulation produces a single-peaked ITCZ located at 7°N, with some non-precipitating low clouds underneath a dry free troposphere toward the southern side. In the northern hemisphere, the subtropics is slightly more moist even though the liquid cloud water is smaller than in the southern hemisphere.

Figure 3.1d shows the zonal winds (u), with positive values indicating the zonal wind being westerly. The thick solid contours indicates $u = 0$ m/s, thin solid contours indicate

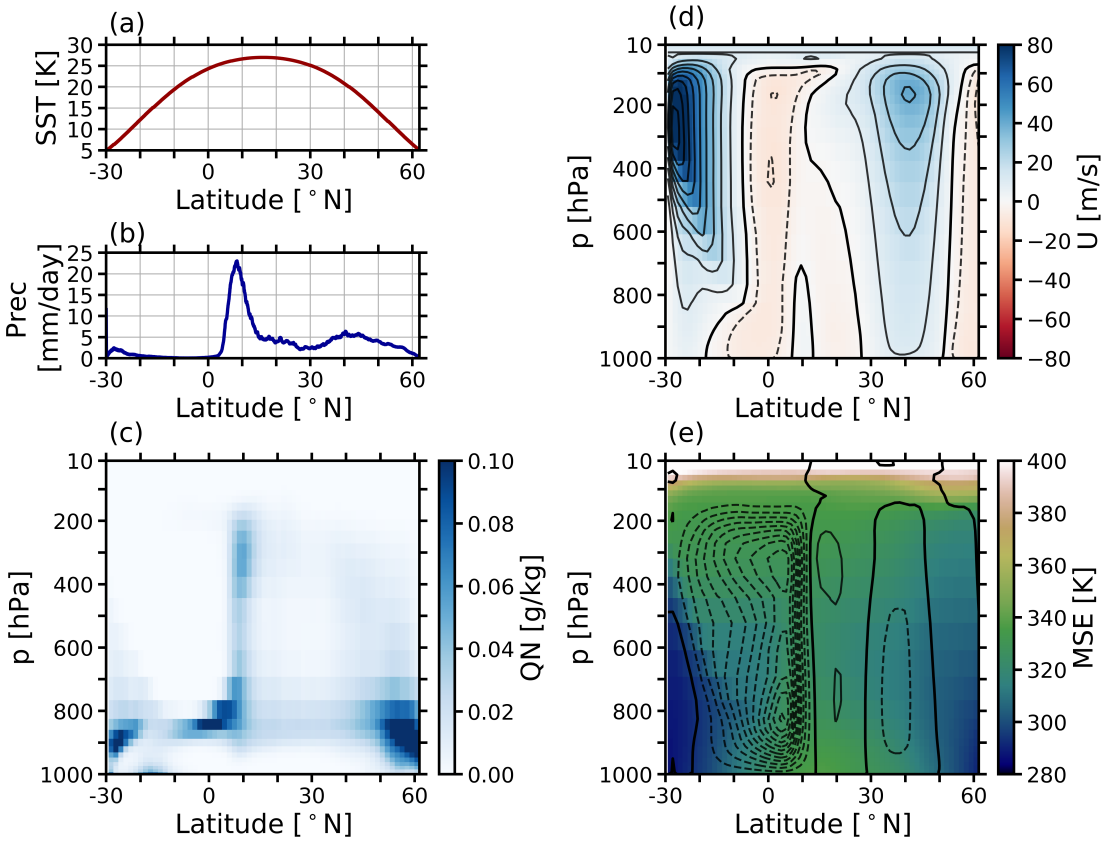

Figure 3.1: Zonal-time mean of the NGAqua 'TC1' simulation

Zonal-time averages of (a) sea surface temperature (SST), (b) surface precipitation (Prec), (c) liquid water and ice cloud condensates (QN), (d) zonal wind (U), and (e) moist static energy in temperature unit (MSE/c_p) and streamfunction from the NGAqua TC1 simulation. For (d), the thick solid contours indicates where U = 0 m/s, the thin solid contours plotted every +10 m/s indicate where the winds are westerly, and the dashed contours plotted every -5 m/s indicate where the winds are easterly. For (e), the thick solid lines indicate zero-streamfunction. The thin solid lines are positive streamfunctions plotted every 1000 m^2/s, while the dashed lines are negative streamfunctions plotted every -1000 m^2/s. The zonal-time averages are from Days 0 to Days 8 of the NGAqua TC1 simulation, during which the simulation has equilibrated and the 3D data are available.

positive values are plotted every 10 m/s, while the dashed contours indicate negative values and are plotted every -5 m/s. Figure 3.1e shows the moist static energy (MSE or $h = c_pT+gz+L_vq_v$) in the temperature unit (colors) and the streamfunction (contours). The thick solid lines indicate zero-streamfunction. The thin solid lines are positive streamfunctions plotted every 1000 m^2/s, while the dashed lines are negative streamfunctions plotted every -1000 m^2/s.

Figures 3.1d - 3.1e show that the general circulation of the TC1 simulation is zonally asymmetric, with the ITCZ being slightly off the equator in the northern hemisphere. The northern hemispheric subtropical jet is located at 40°N with a maximum strength of 40 m/s. The northern Hadley Cell is rather week, extending from 15°N to 30°N. The southern Hadley Cell is very strong; due to the geostrophic balance, this results in a strong westerly flow in the upper troposphere and lower stratosphere at 25°S. This is partly an artifact because the circulation is close to the southern boundary.

In the tropics, the circulations resemble those over the Tropical Eastern Pacific in September [20]. The northeasterly trade winds, with a zonal component of approximately -10 m/s, are found in the subtropics of the northern hemisphere. The southern hemispheric trade winds are slightly stronger. They flow cross-equatorially and recurve at between 5°N and 10°N, converging with the trade winds from the northern hemisphere. By mass continuity, the low-level convergence results in deep convection that produces high clouds and strong precipitation peaked at 10°N, where the low-level zonal winds are weakly westerly. This strong precipitation band of the ITCZ is also evident in Figure 3.2a, a snapshot of cloud fraction (CLD) at Day 4 of the TC1 simulation. To the south of the ITCZ is a stratocumulus cloud regime with cross-equatorial flows. The red box highlights a region with a mature TC that spins up from a zonal band of positive absolute vorticity north of the ITCZ, also called a vorticity filament. The precipitable water (PW) and absolute vorticity at 850 hPa (η_{850}) over this region are shown in Figure 3.2b-c. It is shown in the following section that a TC's initial vortex that axisymmetrizes from a vorticity filament is part of the easterly waves that form north of the ITCZ.

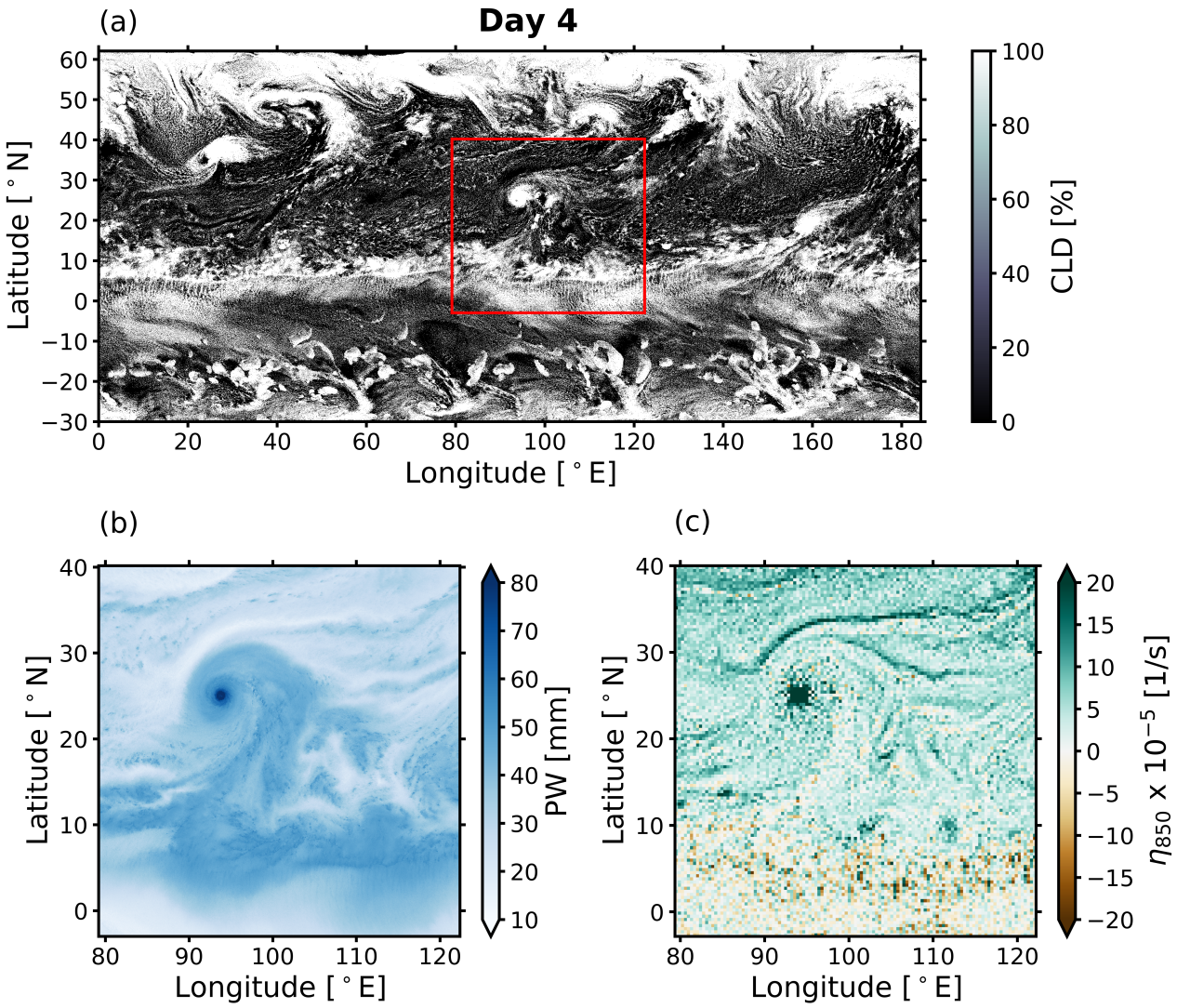

Figure 3.2: Snapshots at Day 4 from NGAqua 'TC1' simulation

(a) An instantaneous snapshot of the cloud fraction (CLD) at Day 2 of the TC1 simulation, at which a well-developed tropical cyclone (TC) is presented at 20°N and 95°E, by the northern edge of the Intertropical Convergence Zone (ITCZ). Panels (b) and (c) show precipitable water (PW) and 850-hPa absolute vorticity (η_{850}) zoomed in over the TC and part of the ITCZ; this region is indicated by a red box in Panel (a). The η_{850} is coarse-averaged to 20-km horizontal resolution.

3.4 Large-Scale Circulations Giving Rise to Pre-TC Vortices

TCs in NGAqua spontaneously spin up between 10°N and 20°N from vorticity filaments, the strongly positive vorticity bands that are a result of the meridional shear in the zonal wind flow. In this region, the SST is warm enough and the PW is sufficiently high to support deep convection. Inside the ITCZ, however, the low-level absolute vorticity is noisy and close to zero when averaged over a large scale (e.g., 40-km resolution or coarser).

As shown in Figure 3.2a, by Day 4 there is a well-developed TC at 20°N and 100°E, with an obvious eye and the minimum surface pressure or PSFC as low as 880 hPa. Figures 3.2b and 3.2c zoom in over the red-boxed region in Figure 3.2a, showing PW and η_{850}, respectively. The TC previously draws its moisture from the ITCZ, and a weak vorticity filament connecting the TC's center to the northern edge of the ITCZ is still visible. It is obvious in Figure 3.2c that to the southeast of the mature TC, there are two cyclonic vortices that just start to organize. But the PW associated with these two vortices are still close to the background PW of the ITCZ and cannot be distinguished at this time. The vortex on the left, at 100°E and 10°N, will later become a TC (PSFC deepens below 980 hPa), while the one on the right, at 110°E and 10°N, remains as a tropical depression until the end of the simulation.

Video S1 in the supplementary information shows the PW and η_{850} of NGAqua TC1 simulation from Day 0 to Day 20. They show examples of pre-TC vortices axisymmetrizing from vorticity filaments, which are found north of the ITCZ. Most of them move northwestward after they spin up between 10°N and 15°N. Here we will show that, an initial vortex originated from a region of high PW north of the ITCZ organizes itself into an axisymmetric flow. The initial formation depends on the large-scale flow associated with the easterly waves. [1] It will be shown in Section 3.5 that, if maintained by sufficient moisture, a cyclonic vortex that is part of an easterly wave will develop a protected warm core. Then, deep convection

[1] Unlike the African Easterly Waves which draw their energy from baroclinic instability due to meridional temperature gradient over Africa [33], the easterly waves in NGAqua draw their energy from barotropic instability associated with the ITCZ breakdown.

helps the vortex spin up into a TC via vertical stretching of absolute vorticity. Since this process occurs in a convective scale, it is helpful to look at the vorticity spin-up following the vortex system. Hence, we will first introduce an algorithm used to track these vortices before further discussing the TCG processes.

3.4.1 Tracking Tropical Cyclones in NGAqua

Figure 3.3 summarizes the steps taken to track the easterly waves and TCs in NGAqua simulations. First the algorithm looks for the grid cells that meet the meteorological criteria for being potential pre-TC vortices and find their centers. Then a machine learning algorithm called the density-based spatial clustering of applications with noise (DBSCAN) is used to regroup the centers of the vortices into tracks of the wave disturbances and TCs, followed by smoothing the track locations. Finally, we classify the tracks whether they become TCs based on the minimum PSFC. If PSFC reaches 980 hPa, the system is considered a TC. Otherwise, it is referred to as a pre-TC or cyclonic vortex.

First, we block-average the instantaneous hourly NGAqua outputs to 80 km $\times$ 80 km and compute the 850-hPa large-scale relative vorticity ($\zeta_{850,\mathrm{LS}}$) using center differencing of the zonal (u) and meridional (v) winds at 850 hPa: $\zeta_{850,\mathrm{LS}} = \frac{\partial v}{\partial x} - \frac{\partial u}{\partial y}$. Since the cyclonic vortices in NGAqua organize themselves from vorticity filaments, where there is strong meridional shear of zonal winds ($-\frac{\partial u}{\partial y}$) due to the ITCZ mean flows, we first ensure that the considered grid cells also have strong zonal shear of meridional winds ($\frac{\partial v}{\partial x}$) that contribute to the overall relative vorticity. The grid columns in NGAqua are considered cyclonic vortices if the following conditions are met, otherwise the grid columns are discarded after each step:

- SST $\geq 25^{\circ}$C
- $\frac{\partial v}{\partial x} \geq 1.5 \times 10^{-5}$ 1/s
- $-\frac{\partial u}{\partial y} \geq 1.5 \times 10^{-5}$ 1/s

Essentially, the second and third conditions combined imply that $\zeta_{850,\mathrm{LS}} \geq 3.0 \times 10^{-5}$ 1/s.

After taking the steps above, we use DBSCAN to locate the vortex clusters at each

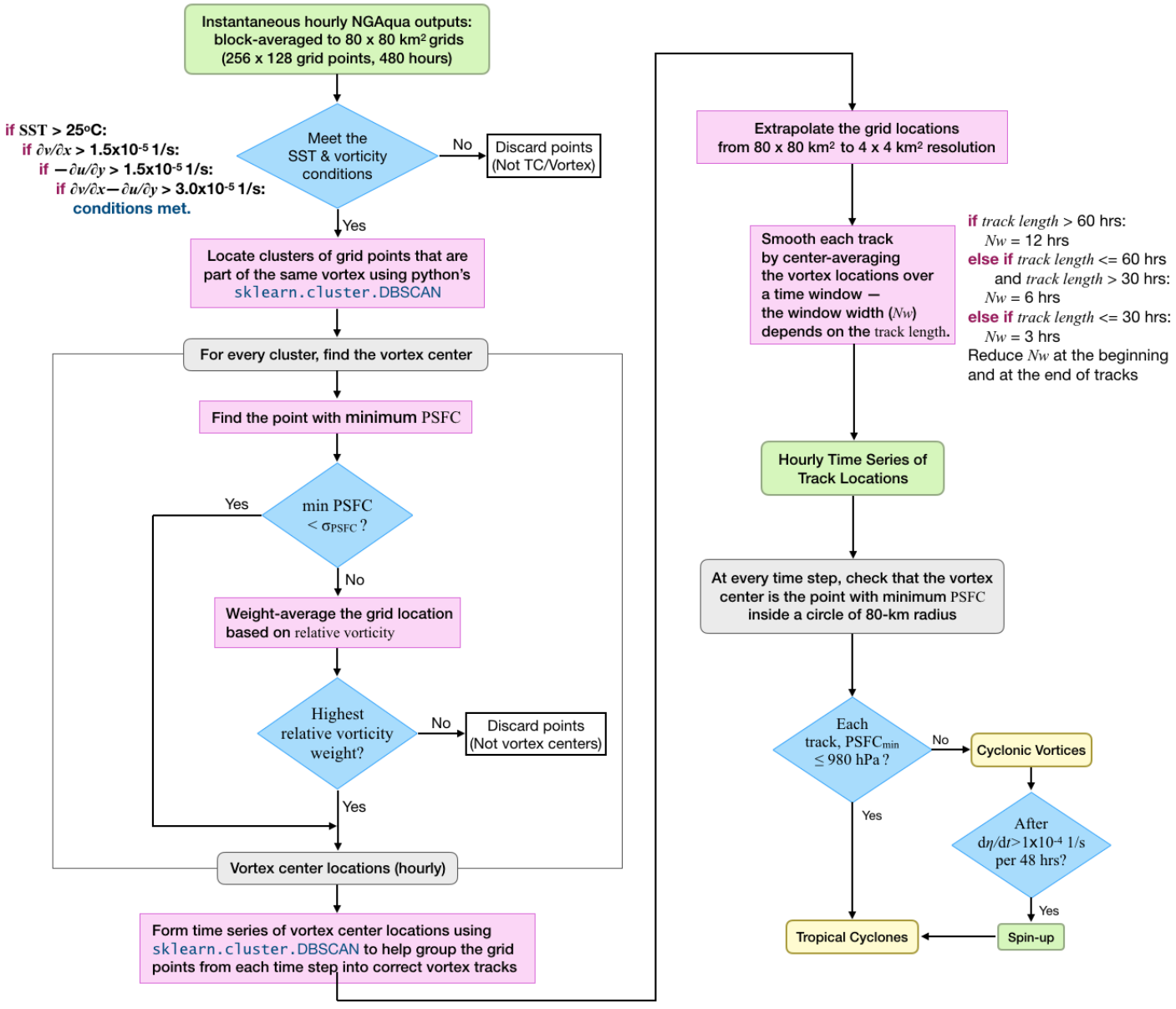

Figure 3.3: A flowchart describing the TC tracking algorithm

time step. The machine learning algorithm is part of Python's scikit-learn machine learning library and is freely available. We choose the DBSCAN clustering algorithm because it discards the noises and effectively groups the adjacent grid points into the same cluster. To find the center, we find the point with minimum PSFC that is smaller than one standard deviation of PSFC in that cluster. If such grid point cannot be found, then the point with highest relative vorticity weight is considered the center of the system.

Once again, we use DBSCAN to help group the grid points from each time step into tracks of cyclonic vortices. For each track, at every time step there is only one 80-km grid point that is considered the center of the vortex. We then extrapolate the grid locations at 80-km resolution back to 4-km resolution, which is the original resolution of NGAqua.

The easterly wave and TC tracks obtained at this step are noisy time series and need further smoothing. Following the tracks, we pick a time window depending on the track lengths and center-average the latitudes and longitudes of the track centers:

- If the track length is longer than 60 hrs, the window width (N_w) is 12 hrs.
- If the track length is between 30 hrs and 60 hrs, N_w is 6 hrs.
- Otherwise, N_w is 3 hrs.

For the beginning and the end of each track, we reduce N_w such that the vortex centers at the first and last time steps of the tracks remain unchanged during the smoothing process. At this step, we have hourly time series of the track locations. We ensure that the vortex center is the point with minimum PSFC inside a circle of 80-km radius at every time step.

Finally, we classify the tracks into pre-TCs vs TCs. If at any point the minimum PSFC goes below 980 hPa, the track is considered a TC. Otherwise, the track remains a cyclonic vortex. An exception is when the 850-hPa absolute vorticity ($\eta_{850} = \zeta_{850} + f$) averaged over a 160×160-km^2 block following the system increases by 1×10^{-4} 1/s within 48 hrs, then after that time the cyclonic vortex becomes a TC.

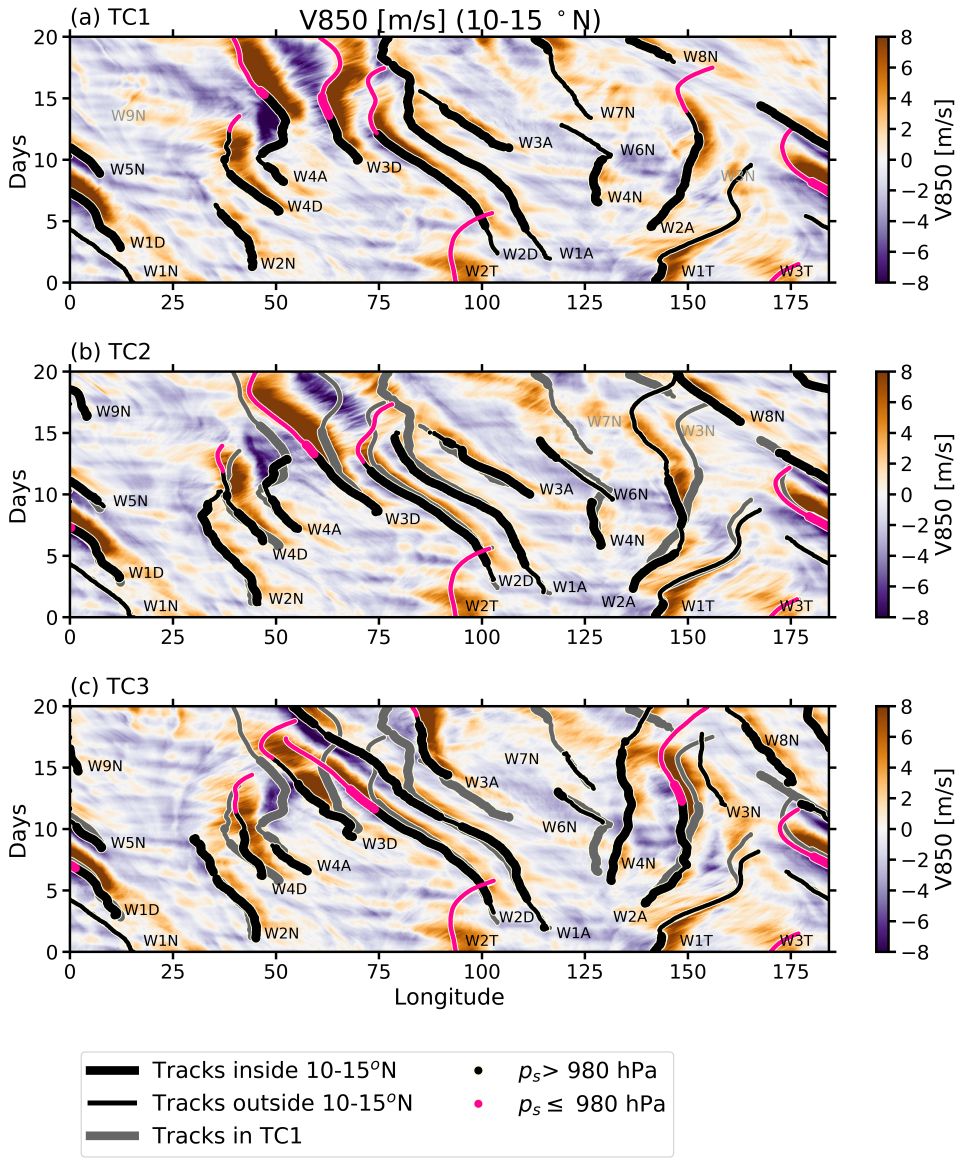

Figure 3.4: Hovmoller diagrams of v_{850} averaged between 10°N and 15°N and TC tracks

Hovmoller diagrams of meridional wind at 850 hPa (V850), overlaid with the tracks of easterly waves and TCs, from the three NGAqua simulations called TC1, TC2, and TC3. The V850 fields are averaged between 10°N and 15°N. The results from Day 0 to Day 20 are presented. Each panel shows the tracks of cyclonic vortices (black) and tracks of developed TCs (central surface pressure below 980 hPa, pink) from each of the corresponding simulations. Also shown in (b) and (c) are the tracks from TC1 (gray). Thicker tracks indicate that the systems are between 10°N and 15°N, where most of the vortices originate, while thinner tracks indicate the systems are outside the region of interest. See texts for the wave nomenclature system.

3.4.2 Naming the Tropical Cyclones

Figure 3.4a shows Hovmoller diagrams of the meridional wind at 850 hPa (v_{850}) from the TC1, TC2, and TC3 simulations averaged between 10-15°N, overlaid with the tracks of the easterly waves and TCs. Because most easterly waves originate in the region between 10°N and 15°N, the v_{850} field shown in the Hovmoller diagram is also averaged over the same latitudinal band. The black thick lines indicate the tracks located between 10°N and 15°N, while the black thin lines indicate the tracks outside region of interest. The pink lines indicate that the minimum PSFC is reduced below 980 hPa, which means the vortices have become TCs.

Figures 3.4b and 3.4c show v_{850} in the TC2 and TC3 simulations, respectively. The black and pink tracks indicate the vortices or the easterly waves in TC2 and TC3 simulations, as in Figure 3.4a, while the gray tracks indicate the vortices in TC1 simulation.

A total of 51 easterly waves (or waves for short) are classified into four categories: developing waves (D), non-developing waves (N), ambiguously developing waves (A), and weakening TCs (T). First, developing waves are those that become TCs in all three NGAqua simulations; there are four of them in each simulation, and thus are called W1D through W4D. Second, non-developing waves are those that do not become TCs in any of the simulations; they are called W1N through W9N. Third, ambiguously developing waves are used for those that become TCs in some but not all NGAqua simulations; they are called W1A through W4A. Finally, the waves that are already well developed TCs at Day 0 and will decay as the simulations go on are called W1T through W3T.

All of the vortices that become TCs (W1D–W4D) propagate northwestward as they intensify, and recurve after they become fully developed TCs. There are also weak initial vortices that propagate east/northeastward in the beginning. In particular, W2A initially move eastward between Days 4 and 10, during which they have a chance to pick up the humidity and wind speed, and then later propagate northwestward and become a TC in TC1 and TC3 simulations.

3.4.3 Pre-TC Vortices Originating From Vorticity Filaments

Figure 3.5 shows snapshots of 40-km block-averaged absolute vorticity at 850 hPa from NGAqua TC1 simulation, over the region in which TCG occurs. At Day 2.5 there exists a large-scale vortex at 8°E and 19°N that propagates northwestward. Because the system does not become a TC but rather remains as a cyclonic vortex for several days, it is considered "Non-Developing" and thus called "W1N." A vorticity filament is found southeast of W1N, between 0°E–30°E and 10°N–15°N. By Day 4.0, a new cyclonic vortex that later becomes a TC starts to organize from the vorticity filament (red circle). This "Developing" wave is called "W1D." It intensifies at Day 5.5 and becomes a tropical cyclone at Day 7.0. We will discuss W1D further in Sections 3.5 and 3.6.1.1.

Similarly between 120°E–160°E and 10°N–20°N, we see another cyclonic vortex organizing within a vorticity filament (purple circle) at Day 5.5. Because this system becomes a TC in TC1 and TC3 simulations but not in TC2, it is classified as "Ambiguously Developing" and called "W2A." It will be discussed further in Section 3.6.1.2.

As shown in Figure 3.5, the detected cyclonic vortices in NGAqua are found within zonal bands with strong absolute vorticity (η_{850}), in contrast with the weak and noisy η_{850} to the south. Comparing this with Figure 3.6 which shows snapshots of PW in the tropics, it is clear that the cyclonic vortices are located in the northern edge of the ITCZ, an area with high PW. The undulation of the ITCZ can be seen between 120°E and 180°E, as an upside-down V shape of high PW. The vorticity filaments axisymmetrize into cyclonic vortices here during the ITCZ breakdown process, as in Ferreira and Schubert (1997) [23]. The group of cyclonic vortices between 100°E and 120°E that are southeast of a developed TC called W2T is another example. In this case, W2T spins up as the ITCZ breaks down and create another upside-down V shape. Later, W2T moves further north allowing the undulated ITCZ to return to its original shape.

Video S2 in the supporting information shows animations of η_{850} in the tropics of TC1, TC2, and TC3 simulations. It shows that the cyclonic vortices in NGAqua all axisymmetrize

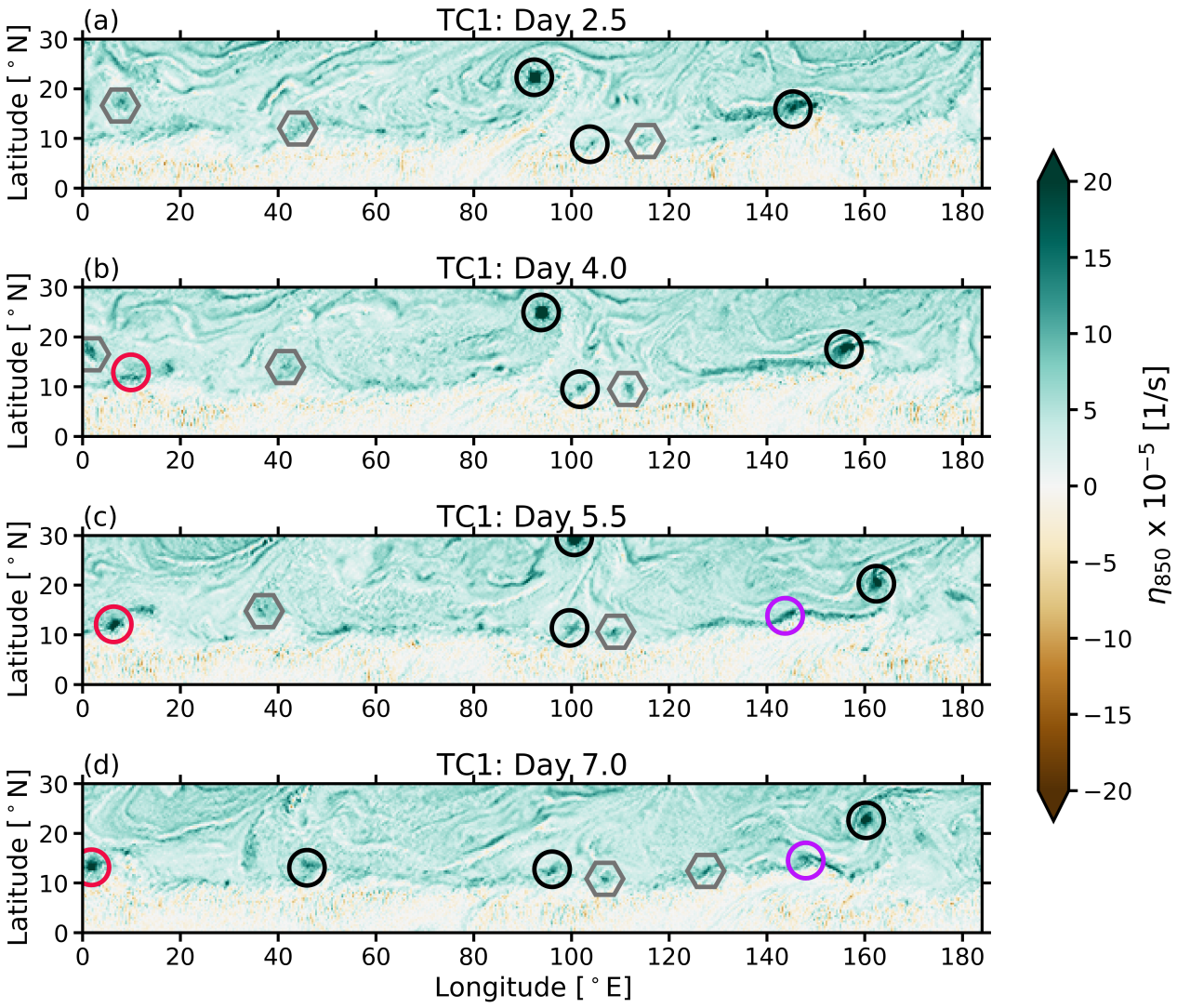

Figure 3.5: Snapshots of 850-hPa absolute vorticity in the tropics of NGAqua TC1 simulation

Instantaneous snapshots of absolute vorticity at 850 hPa (η_{850}) between 0° and 30°N of the NGAqua TC1 simulation, where tropical cyclogenesis (TCG) occurs. They are taken 1.5 days apart, at (a) Day 2.5, (b) Day 4.0, (c) Day 5.5, and (d) Day 7.0. The circles highlight the vortices that are or will become TCs. The hexagons highlight the vortices that persist for several days but remain as cyclonic vortices. The red and purple circles specifically highlight W1D and W2A, respectively. They spin up from vorticity filaments north of the ITCZ and are discussed further in Figures 3.13 and 3.7. The η_{850} is coarse-averaged to 40-km horizontal resolution to reduce the noise.

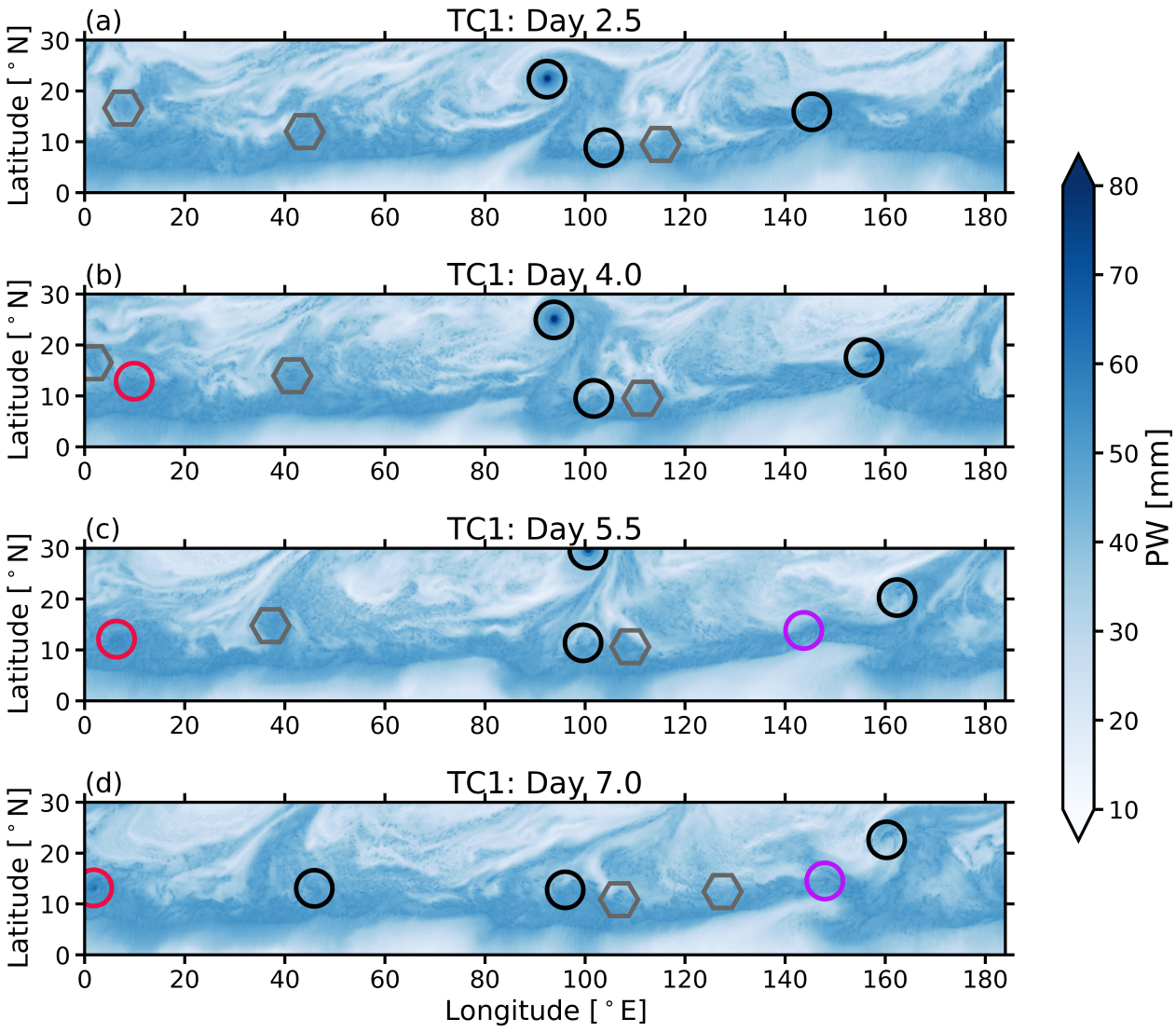

Figure 3.6: Snapshots of precipitable water in the tropics of NGAqua TC1 simulation

As in Figure 3.5 but for instantaneous snapshots of precipitable water (PW). The ITCZ is visible as a zonal band of high PW.

from the vorticity filaments, of which the formations depend on the large-scale barotropic instability associated with the ITCZ. The large-scale flows in three NGAqua simulations start to diverge after Day 10.

This section shows that the large-scale flows give rise to vorticity filaments that axisymmetrize to become cyclonic or pre-TC vortices. The following section analyzes further how the small-scale processes help the pre-TC vortices spin up and become TCs.

3.5 The Role of Convective-Scale Vorticity Spin-Up in Tropical Cyclogenesis

Given an existing low-level vortex that forms from a vorticity filament north of the ITCZ, what is a primary mechanism that leads to TCG? To answer the question, we first consider the vorticity budget equation and then apply it to the TCs in NGAqua.

3.5.1 Vorticity Budget Equation

Our analysis of tropical cyclogenesis is enhanced by an understanding of the vorticity equation. We consider the flux form of vorticity equation derived from equation 4.2 of Haynes and McIntyre (1987) and equation 3 of Raymond and Carrillo (2011) [28, 46]. Let $\vec{u} = (u, v, w)$ be the three dimensional velocity field, $\vec{\Omega}$ be the earth's angular velocity, and $f = \hat{k} \cdot 2\vec{\Omega}$ be the planetary vorticity, it follows that $\vec{\omega} = \nabla \times \vec{u} = (\omega_x, \omega_y, \zeta)$ is the three-dimensional relative vorticity, and $\vec{\omega}_a = \vec{\omega} + 2\vec{\Omega} = (\omega_{xa}, \omega_{ya}, \eta)$ is the three-dimensional absolute vorticity. Also let ρ be the air density, p be the pressure, and $\vec{F}$ be the friction. The three-dimensional vorticity equation in flux form can be written as:

$$\frac{\partial \vec{\omega}_a}{\partial t} + \nabla \times (\vec{\omega}_a \times \vec{u}) = \frac{1}{\rho^2} \nabla\rho \times \nabla p + \nabla \times \vec{F}. \tag{3.1}$$

The first term on the left hand side of equation 3.1, $\frac{\partial \vec{\omega}_a}{\partial t}$, denotes the changes of $\vec{\omega}_a$ at a given location. The second term, $\nabla \times (\vec{\omega}_a \times \vec{u})$, combines the effects that vertical stretching, horizontal advection, vertical advection, and tilting have on $\vec{\omega}_a$ altogether. The terms on the right hand side represent the $\vec{\omega}_a$ changes due to baroclinicity and friction. They are

small and can be neglected.[2] By neglecting these two terms, $\hat{k} \cdot$ Eqn 3.1 leads to a simplified equation of the vertical component of the absolute velocity:

$$\begin{aligned} \frac{\partial \eta}{\partial t} &= -\frac{\partial}{\partial x}\big(u\eta\big) - \frac{\partial}{\partial y}\big(v\eta\big) + \frac{\partial}{\partial x}\big(w\omega_{xa}\big) + \frac{\partial}{\partial y}\big(w\omega_{ya}\big) \\ &= -\nabla_h \cdot \big(\eta \vec{u}_h\big) + \nabla_h \cdot \big(w\vec{\omega}_{ha}\big) \end{aligned} \tag{3.2}$$

where $\frac{\partial \eta}{\partial t}$ represents changes in η at a given location. On the right hand side, $-\nabla_h \cdot (\eta \vec{u}_h)$ is the horizontal convergence of the absolute vertical vorticity flux, and $\nabla_h \cdot (w\vec{\omega}_{ha})$ is the horizontal divergence of absolute horizontal vorticity flux. The first term combines the physical vertical stretching and horizontal advection of η together, while the other term combines the physical tilting and vertical advection of absolute vorticity. They are referred to as the "generalized stretching" and "generalized tilting," respectively. In a vortex-following framework, a vortex-relative horizontal velocity is used, so equation 3.2 becomes:

$$\begin{aligned} \frac{\partial \eta}{\partial t} &= -\frac{\partial}{\partial x}\big((u - U_C)\eta\big) - \frac{\partial}{\partial y}\big((v - V_C)\eta\big) + \frac{\partial}{\partial x}\big(w\omega_{xa}\big) + \frac{\partial}{\partial y}\big(w\omega_{ya}\big) \\ &= -\nabla_h \cdot \big(\eta(\vec{u}_h - \vec{U}_C)\big) + \nabla_h \cdot \big(w\vec{\omega}_{ha}\big) \\ &= \frac{\partial \eta}{\partial t}\Big|_{Stretch} + \frac{\partial \eta}{\partial t}\Big|_{Tilt} \end{aligned} \tag{3.3}$$

where $\vec{U}_C = (U_C, V_C)$ is the steering wind velocity that moves the cyclone.

In the vortex-following framework, the generalized tilting term is small compared to the other two terms. As for the generalized stretching, the physical vertical stretching $-\eta\frac{\partial u}{\partial x} - \eta\frac{\partial v}{\partial y}$ is positive in the region where there is horizontal convergence in the region of positive η, i.e., where there is more precipitation. On the other hand, the physical horizontal advection $-(u - U_C)\frac{\partial \eta}{\partial x} - (v - V_C)\frac{\partial \eta}{\partial y}$ tends to be negative in this situation, since the flow brings lower-η air from the drier region to the vortex center. But for a developing TC, the magnitude of the physical vertical stretching is always greater than that of the physical horizontal advection.

[2] In the tropics of NGAqua, the baroclinic term, which is on the order of $\sim \mathcal{O}(10^{-13}\ 1/\mathrm{s}^2)$, is 3 to 4 orders of magnitude smaller than the terms on the left hand side. The frictional term is also small above the surface.

Integrating equation 3.3 with respect to time, we obtain a time series of absolute vorticity contributed by generalized stretching, and that contributed by generalized tilting. In theory, if the generalized stretching is a major contribution to the absolute vorticity tendency during TCG, then:

$$\eta(t) \approx \eta_{Stretch}(t). \tag{3.4}$$

In the next section, we will show that the approximation above holds true in most pre-TC vortices during the period which they spin up in NGAqua.

3.5.2 Vertical Stretching of Absolute Vorticity as a Convective-Scale Vorticity Source

Figure 3.7 shows the hourly time series of (a) 850-hPa absolute vorticity (η) and absolute vorticity derived from integrating the generalized stretching tendency with respect to time ($\eta_{Stretch}$), (b) surface precipitation (Prec) and precipitable water (PW), and (c) latent heat flux (LHF) and central surface pressure (PSFC) averaged over a 160-km domain following a developing tropical cyclone W1D of the TC1 simulation. The vertical dashed line indicates a point when W1D becomes a TC, which is when the surface pressure deepens below 980 hPa. Figure 3.7a shows that there is a good correlation between $\eta_{Stretch}$ and η during the pre-TC stage. This suggests that the generalized stretching of absolute vorticity contributes positively to the vorticity tendency of the cyclonic vortex system. Figure 3.7b shows that at Days 4.5 and 5.5 where the precipitation peaks, there is strong convection of which the vertical motion stretches the atmospheric column and increases the absolute vorticity. This is in agreement with the 3-dimensional heating profiles following the core of the vortex system (not shown); the mid-tropospheric heating associated with the convection results in vorticity stretching at the lower level.

After Day 7, the $\eta_{Stretch}$ and η do not correlate well. This is because after the spin-up, the TC expands beyond the 160×160-km^2 region. The updrafts and vertical stretching do not concentrate only within the TC center but occur everywhere inside the TC. The

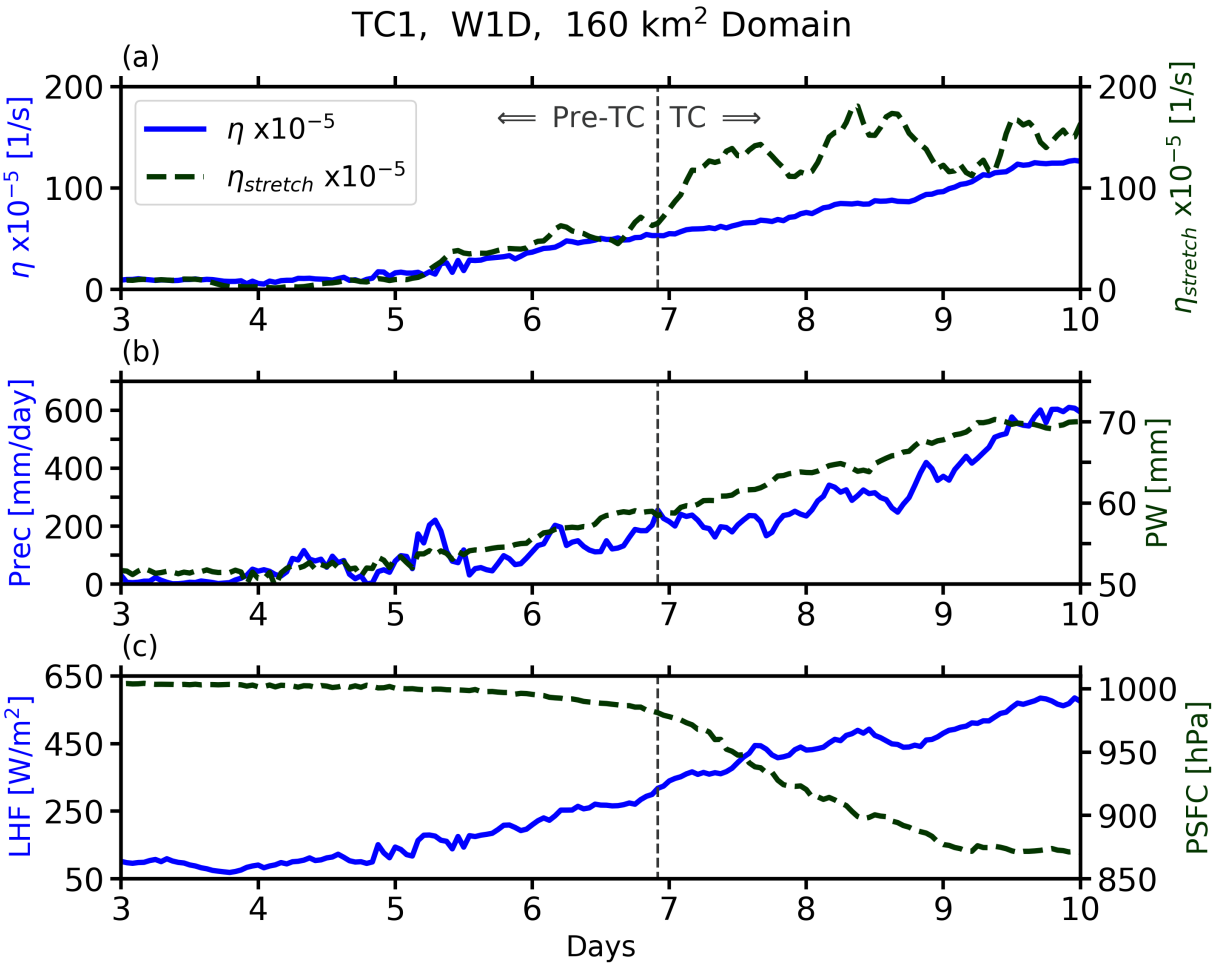

Figure 3.7: Time series from NGAqua TC1 outputs following wave W1D

Time series of various fields averaged within a 160×160-km^2 block of the first developing wave (W1D) from the NGAqua TC1 simulation. (a) Time series of 850-hPa absolute vorticity (η, solid) and absolute vorticity derived from the generalized stretching tendency ($\eta_{stretch}$, dashed). (b) Time series of surface precipitation (Prec, solid) and precipitable water (PW, dashed). (c) Time series of surface latent heat flux (LHF, solid) and central or minimum surface pressure (PSFC, dashed). The vertical dashed line indicates when the vortex system becomes a TC, which is when PSFC reaches 980 hPa.

generalized tilting, which combines both physical tilting and vertical advection of absolute vorticity (to the mid- and upper-troposphere for example), compensates for the excessive amount of generalized stretching during this period. Because the 3-dimensional outputs of the TC1 NGAqua simulation is available up to Day 8 only (because the rest are lost during the storing process), we focus on the 850-hPa $\eta_{Stretch}$ and η time series because they can be computed using the available 2-dimensional outputs. Nonetheless, if the time series are averaged over a larger area, the $\eta_{Stretch}$ and η time series will be in better agreements. But since our focus is on the pre-TC stage during which the vortex system is small, we average the time series over a 160×160-km^2 region.

Figure 3.7b shows that the PW increases as the TC develops, i.e., after Day 5. Figure 3.7c shows that the surface LHF also increases, fluxing more humidity into the atmospheric column and helping moist convection grow. The vertical velocity in turn advects the humidity aloft and simultaneously stretches the vortex in a vertical direction, helping the vortex system spin up. This implies a positive feedback between the vorticity, convection and surface LHF. Finally, a deepening of PSFC is consistent with the nature of a TC that it has a cyclonically rotating warm core.

3.6 The Predictability of Tropical Cyclogenesis

So far we have shown that TCG involves multiscale interactions. TCG in NGAqua depends on the large-scale barotropic instability north of the ITCZ that gives rise to pre-TC vortices and the small-scale convection that intensifies the vortices through vertical stretching. According to Figure 3.4 and Video S2, the large-scale circulations remain similar among the three simulations up to approximately Day 10. So the cyclonic vortices formed within the first ten days of the simulation remain at the same locations and if they intensify, they become TCs at approximately the same time. However, the tracks diverge noticeably after that. Moreover, new formations of cyclonic vortices are no longer predictable beyond Day 12, such as W3N, W7N and W9N which do not appear at all in some of the simulations.

Given vorticity filaments formed in similar areas of NGAqua TC1, TC2, and TC3 sim-

ulations, how predictable is the convective-scale spin-up process? In the first part of this section, we consider two case studies: W1D and W2A. W1D is an example of systems that develop early on in the simulations while both the large-scale circulations and the small-scale convection occur at similar location and time. W2A is an example of systems that form early on as well but remain as cyclonic vortices for many days, and spin up later in only some simulations. Although those that become TCs spin up from the same pre-TC vortices, the precipitation and PW fields already diverge among the NGAqua ensemble members, so the tracks and intensity of the TCs are different. The final part of this section combines all the developing and non-developing waves together and analyzes their composites.

3.6.1 Case Studies

3.6.1.1 Wave W1D

Wave W1D of TC1 simulation is highlighted using red circles in Figures 3.5 and 3.6. In all three NGAqua simulations, the pre-TC vortices axisymmetrize from the vorticity filaments located northeast of waves W1N. Figures 3.4 and 3.8 show that the pre-TC vortices of W1D form at similar times and locations, and the tracks remain similar until the end of their lifetimes. Figure 3.9 shows that the large-scale winds at 850 hPa and PW around waves W1D, indicated by X's, are remarkably similar. Because the large-scale circulations that steer the vortices are still predictable, the tracks of waves W1D are almost identical up to at least Day 9, and diverge slightly afterwards.

Despite the similarity at a large scale, Figure 3.10 shows that there are differences in the convective scale early on, as the accumulated precipitation does not occur at exactly the same place and time. However, in general, precipitation maxima align within the vorticity centers associated with large-scale flows, especially during and after the spin-up or Day 5.

The small-scale spin-up process is evident in Figure 3.11, which shows the time series of a 160×160-km^2 block following wave W1D. At Day 5, the system-following PW starts to increase, providing enough humidity for the deep convection. Precipitation peaks at the

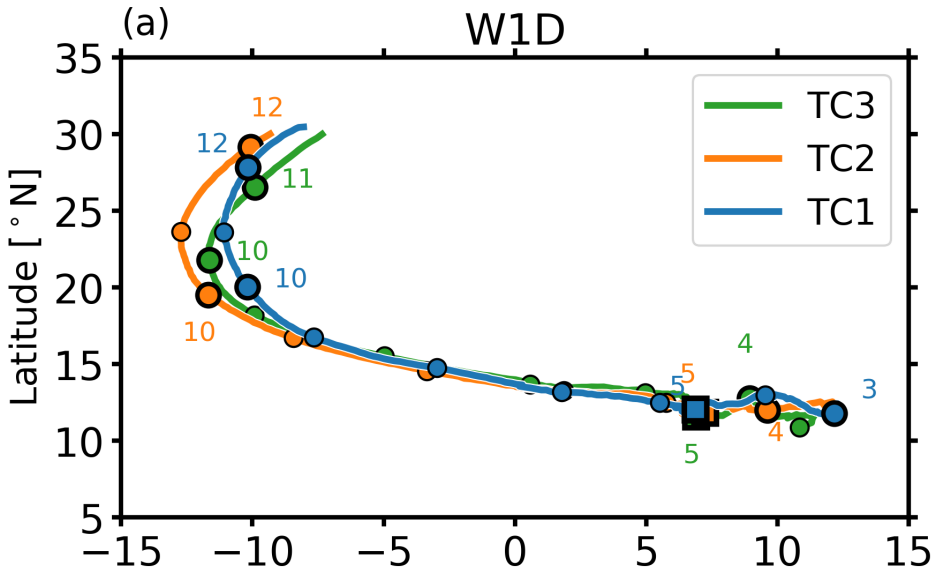

Figure 3.8: Tracks of wave W1D

Tracks of wave W1D in all three NGAqua simulations. The circles show where the vortex systems are at the first hour of each day. The squares indicate when the systems spin up and become TCs.

same time; the vertical velocity stretches the pre-TC vortex, causing η_{850} to intensify. The surface LHF time series suggest that a positive surface flux feedback also takes place as the TC spins up. Panel (c) shows that between Day 5 and Day 8, the rate at which η increases is the same as that of $\eta_{Stretch}$ in all TC1, TC2, and TC3 simulations, suggesting that the generalized stretching contributes positively to the absolute vorticity growth during the early stage. After Day 7, η and $\eta_{Stretch}$ have different slopes for the same reasons mentioned above in Section 3.5.2.

3.6.1.2 Wave W2A

Wave W2A of TC1 simulation is highlighted using purple circles in Figures 3.5 and 3.6. Figures 3.4 and 3.12 show that the pre-TC vortices are formed at the same location. The 850-hPa large-scale wind flows in Figure 3.13 suggest that they axisymmetrize from the

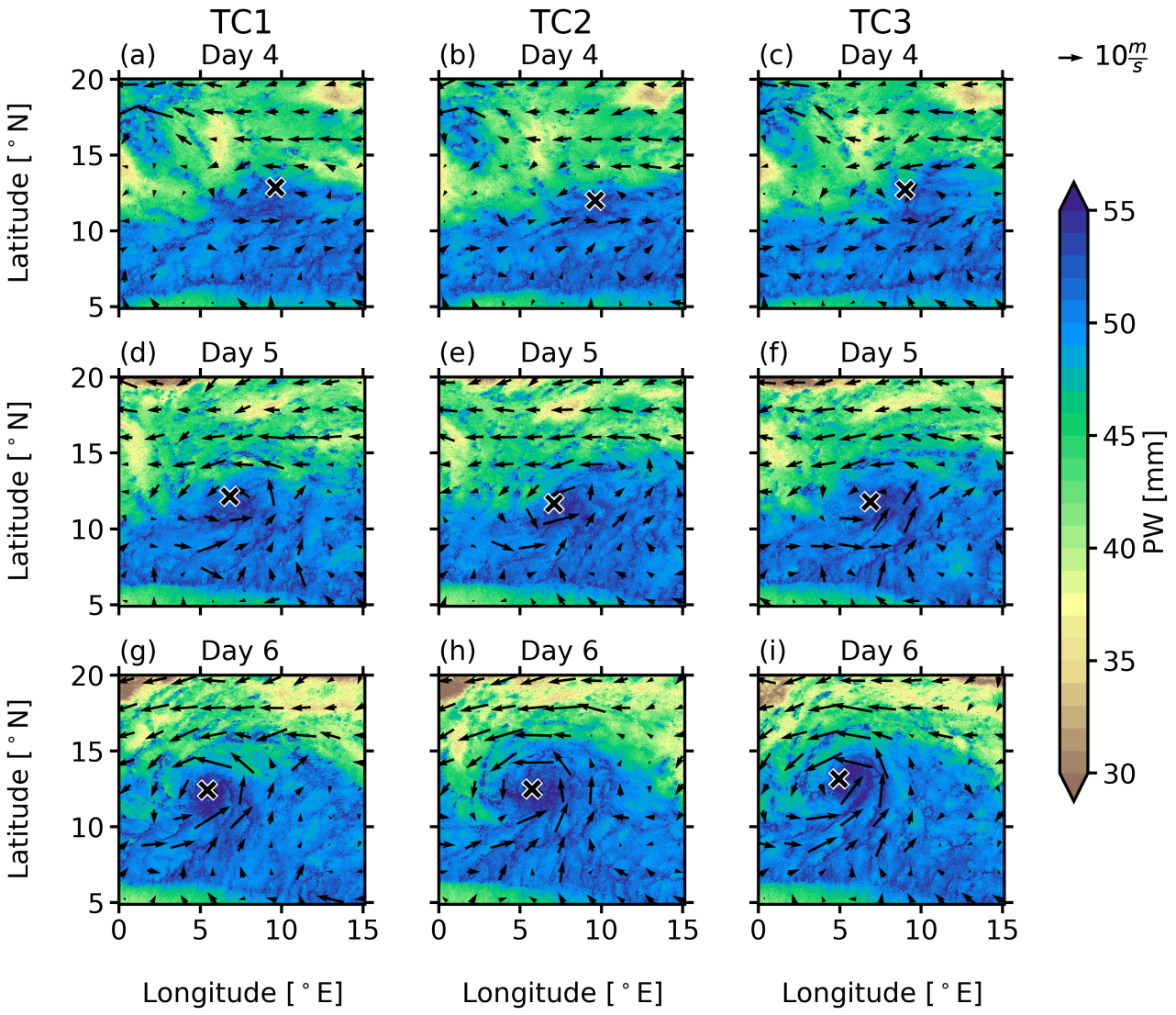

Figure 3.9: Snapshots of precipitable water fields around wave W1D

Snapshots of the precipitable water (PW) at Days 4, 5 and 6 around wave W1D of all three NGAqua simulations. The 850-hPa horizontal wind vectors are also overlaid. The black X's indicate the centers of the vortex systems. The zonal bands of high PW found between 5°N and 10°N are the ITCZ.

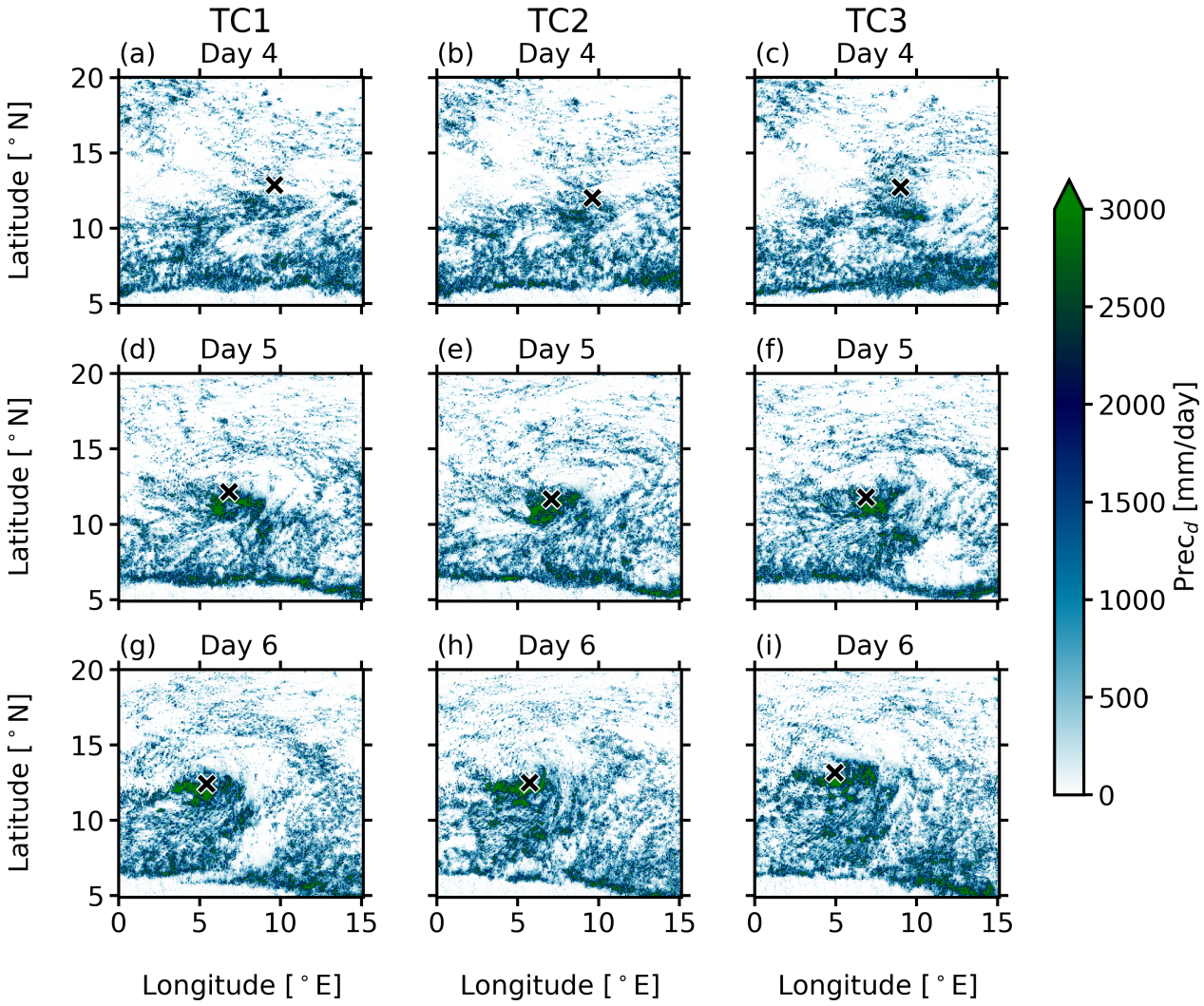

Figure 3.10: Snapshots of precipitation fields around wave W1D

Snapshots of the 24-hour accumulated precipitation (Prec$_d$) at Days 4, 5 and 6 around wave W1D of all three NGAqua simulations. The precipitation is accumulated from 12 hours prior to the indicated time until 12 hours after. The black X's indicate the centers of the vortex systems. The zonal bands of high Prec$_d$ found between 5°N and 10°N are the ITCZ.

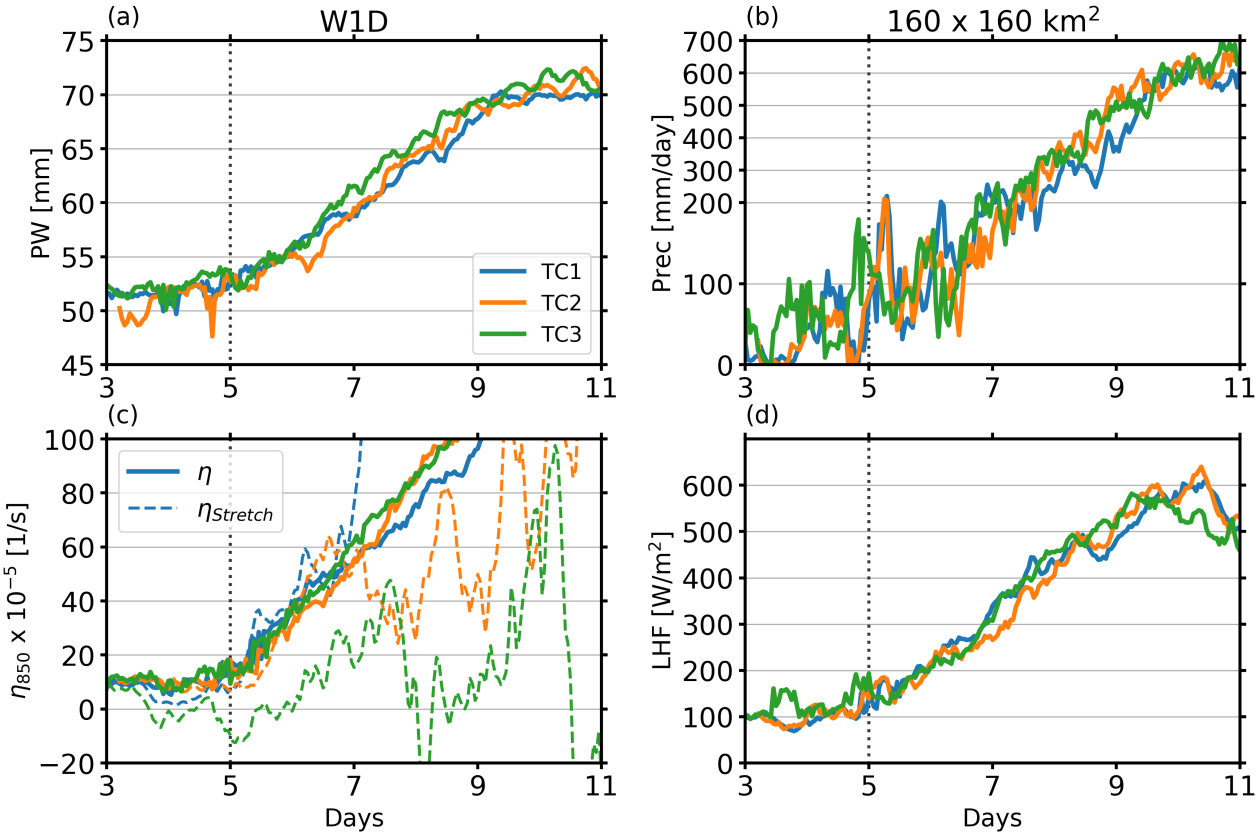

Figure 3.11: Time series from all three NGAqua simulations following wave W1D

Time series of (a) PW, (b) Prec, (c) η_{850}, and (d) LHF averaged over a 160 km $\times$ 160 km region following wave W1D. In panel (c), the 850-hPa vorticity due to generalized stretching ($\eta_{Stretch}$) is also shown in dashed. The vertical dotted lines at Day 5 indicate when the pre-TC vortices spin up due to vertical stretching of vorticity.

same vorticity filaments located west of W1T, which is a TC that is well-developed since the beginning of the simulation. Because of the similar large-scale circulations, the initial vortices all propagate eastward between Day 4 and Day 9 along the northern edge of the ITCZ. Figure 3.12 shows that the vortex in TC2 propagates eastward faster than in TC1 and TC3 simulations. Figure 3.15c shows that η_{850} in TC2 simulation is initially stronger than the rest. The initial vortices in these three simulations propagate northeastward in the beginning. Before Day 9, the vortices move back south to the northern edge of the ITCZ where there is high PW (Figure 3.13a-c). As the vortices pick up the humidity from the ITCZ, they recurve and try to spin up. Figure 3.13 shows that TCG only occurs in the TC1 and TC3 simulations at Day 11, when precipitation peaks and the deep convection aligns with the center of the system. Similar to the W1D case above, vertical stretching contributes positively to the absolute vorticity. The surface LHF feedback plays a role in the convection growth in the two developing TCs as well.

Figure 3.13 shows snapshots of PW, horizontal winds at 850 hPa and the vortex locations of wave W2A in all three simulations. The 24-hour accumulated precipitation is shown in Figure 3.14. At Day 9, the vortices in TC1 and TC3 are located in the northern part of the ITCZ where there are high PW sources from the south. The PW and precipitation fields organize themselves around the vorticity maxima and the systems go through TCG by Day 11. By Day 13, they become TCs with saturated warm cores. The TC in TC3 is stronger than that in TC1 because of higher PW, stronger precipitation, and more positive vorticity stretching tendency. Strong precipitation in TC3 also occurs at an earlier time. This suggests that the TCs in TC1 and TC3 vary in strength and size because of the convective-scale processes, but their locations depend mainly on the large-scale flows.

As for the TC2 simulation, the large-scale configuration at Day 9 is similar to the other two simulations, except there is a dry tongue from the northeast extending southward through the center of the vorticity maximum (Figure 3.13b). This prevents an existing deep convection (Figure 3.14b) from further growing. At Day 11, dry air flows into the vortex center, forming a protected but dry pouch by Day 13 (Figure 3.13e). Although there are still strong

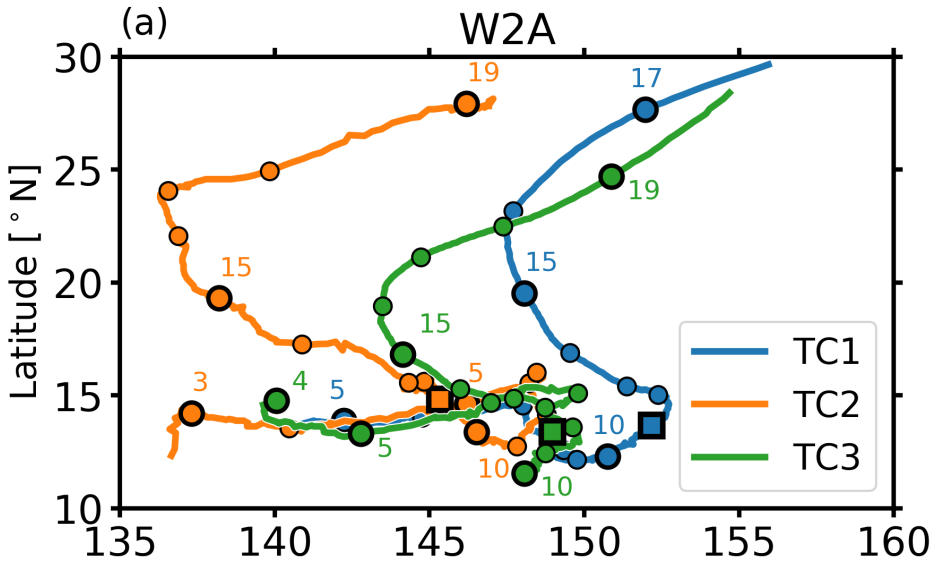

Figure 3.12: Tracks of wave W2A

Tracks of wave W2A in all three NGAqua simulations. The circles show where the vortex systems are at the first hour of each day. The squares indicate the locations of the systems at the first hour of Day 11, approximately when the vortices in TC1 and TC3 simulations become TCs.

precipitation around the vorticity center between Days 11 and 13 (Figures 3.13e and (Figure 3.13h), the vortex does not develop and become a TC because the center of the system is too dry. The cyclonic vortex propagates northwest, bringing along a loosely organized deep convective system. Precipitation and PW increase again at Day 15, but the vortex system is too far from the tropics that the SST is not warm enough to provide energy for TCG.

3.6.2 Composites of the Developing and Non-Developing Waves

We combine the statistics of all wave disturbances that start as initial vortices and become TCs and refer to them as "Developing Waves" (DWs). Those that remain as cyclonic vortices are considered "Non-Developing Waves" (NDWs). DWs consist of the time series from waves W1D through W4D from all three simulations, wave W1A from TC3 simulation, waves W2A

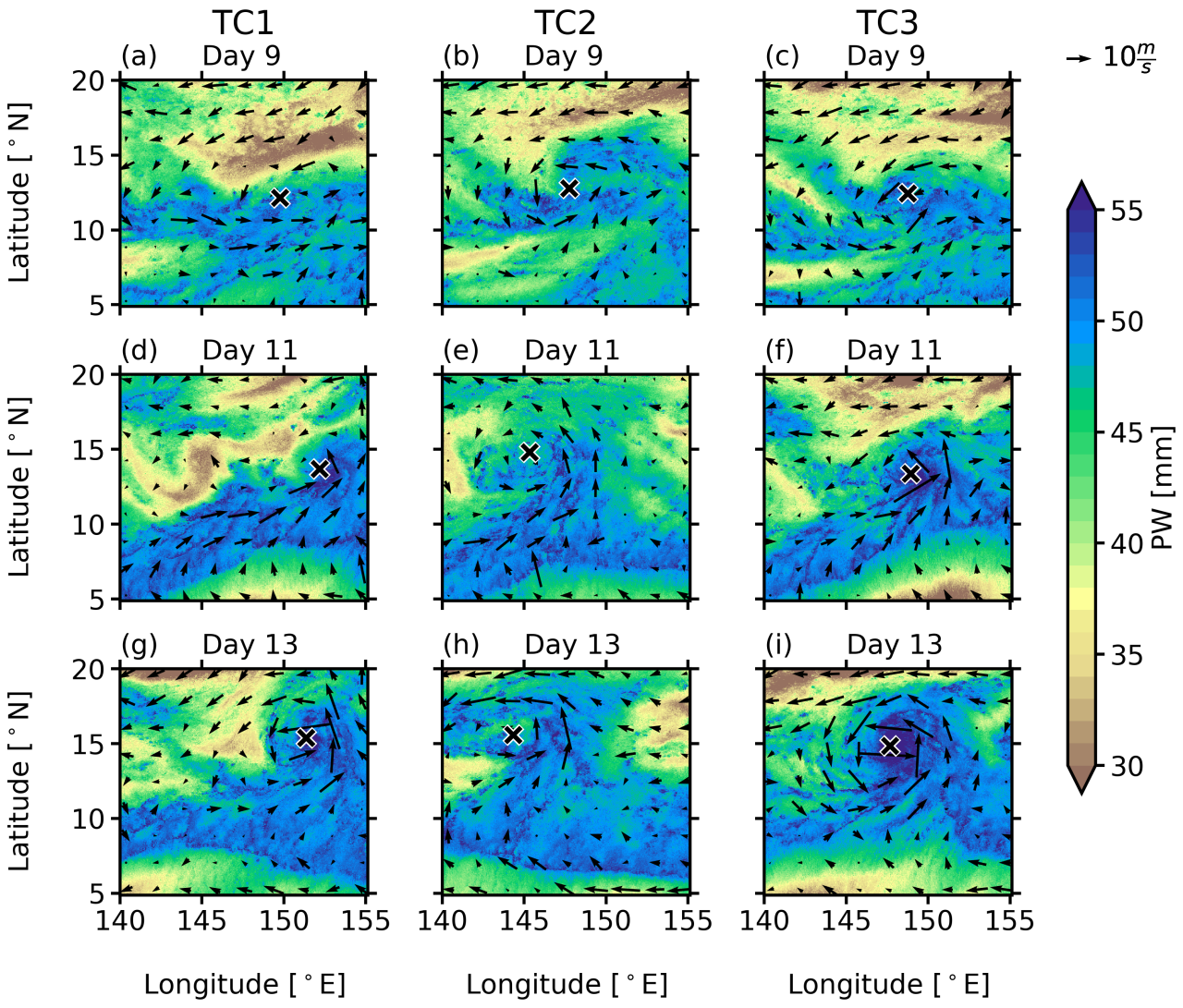

Figure 3.13: Snapshots of precipitable water fields around wave W2A

Snapshots of the precipitable water (PW) at Days 9, 11 and 13 around wave W2A of all three NGAqua simulations. The 850-hPa horiziontal wind vectors are also overlaid. The black X's indicate the centers of the vortex systems.

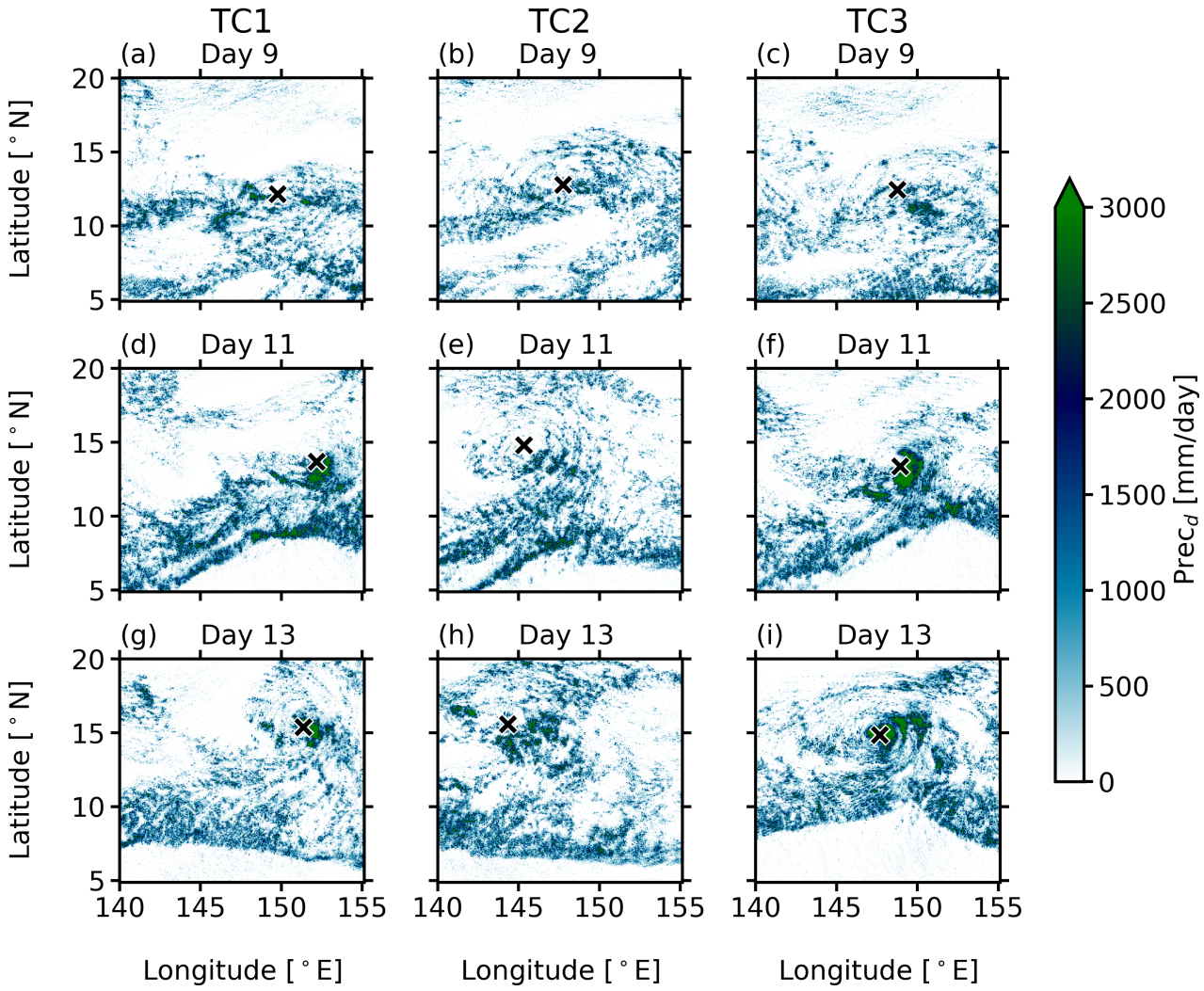

Figure 3.14: Snapshots of precipitation fields around wave W2A

Snapshots of the 24-hour accumulated precipitation (Prec$_d$) at Days 9, 11 and 13 around wave W2A of all three NGAqua simulations. The precipitation is accumulated from 12 hours prior to the indicated time until 12 hours after. The black X's indicate the centers of the vortex systems.

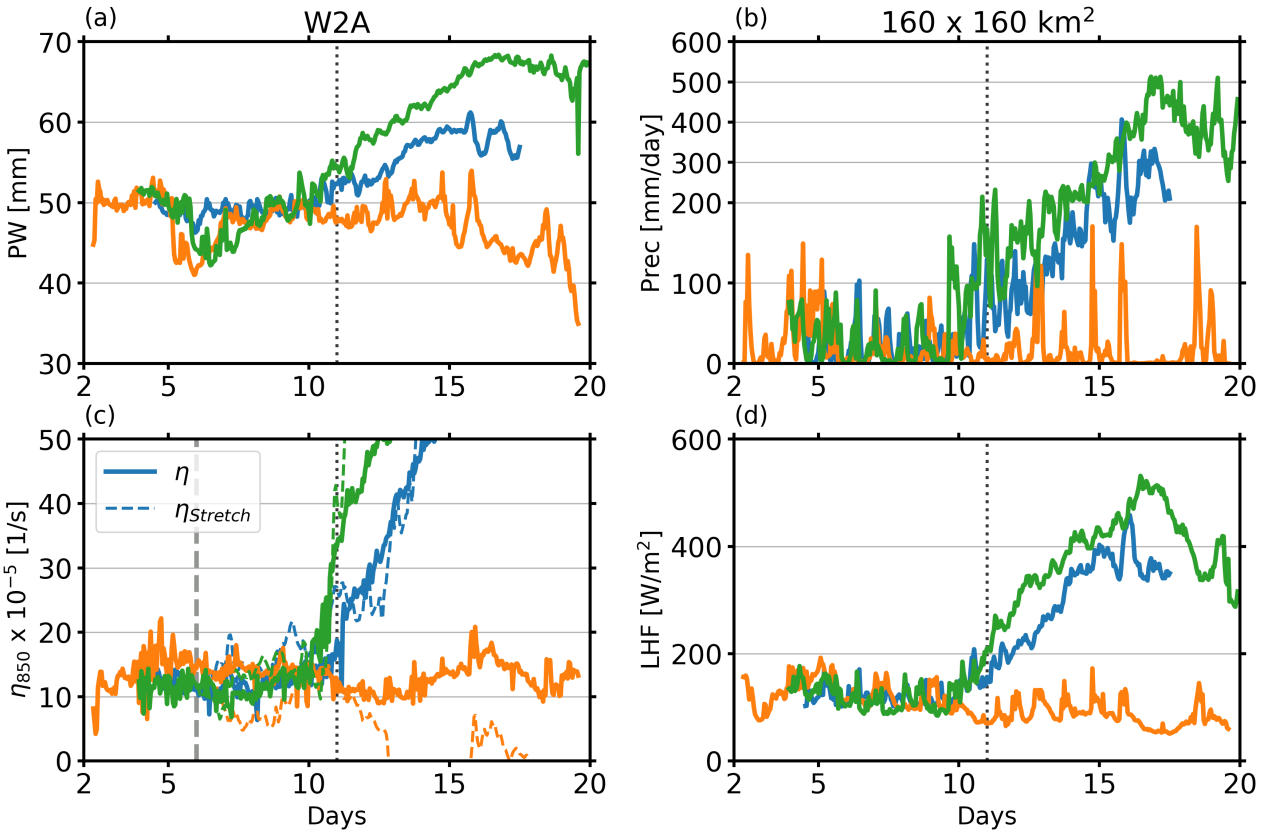

Figure 3.15: Time series from all three NGAqua simulations following wave W2A

Time series of (a) PW, (b) Prec, (c) η_{850}, and (d) LHF averaged over a 160 km $\times$ 160 km region following wave W2A. In panel (c), the 850-hPa vorticity due to generalized stretching ($\eta_{Stretch}$) is also shown in dashed. The vertical dotted lines at Day 11 indicate when the pre-TC vortices in TC1 and TC3 simulations spin up due to vertical stretching of vorticity.

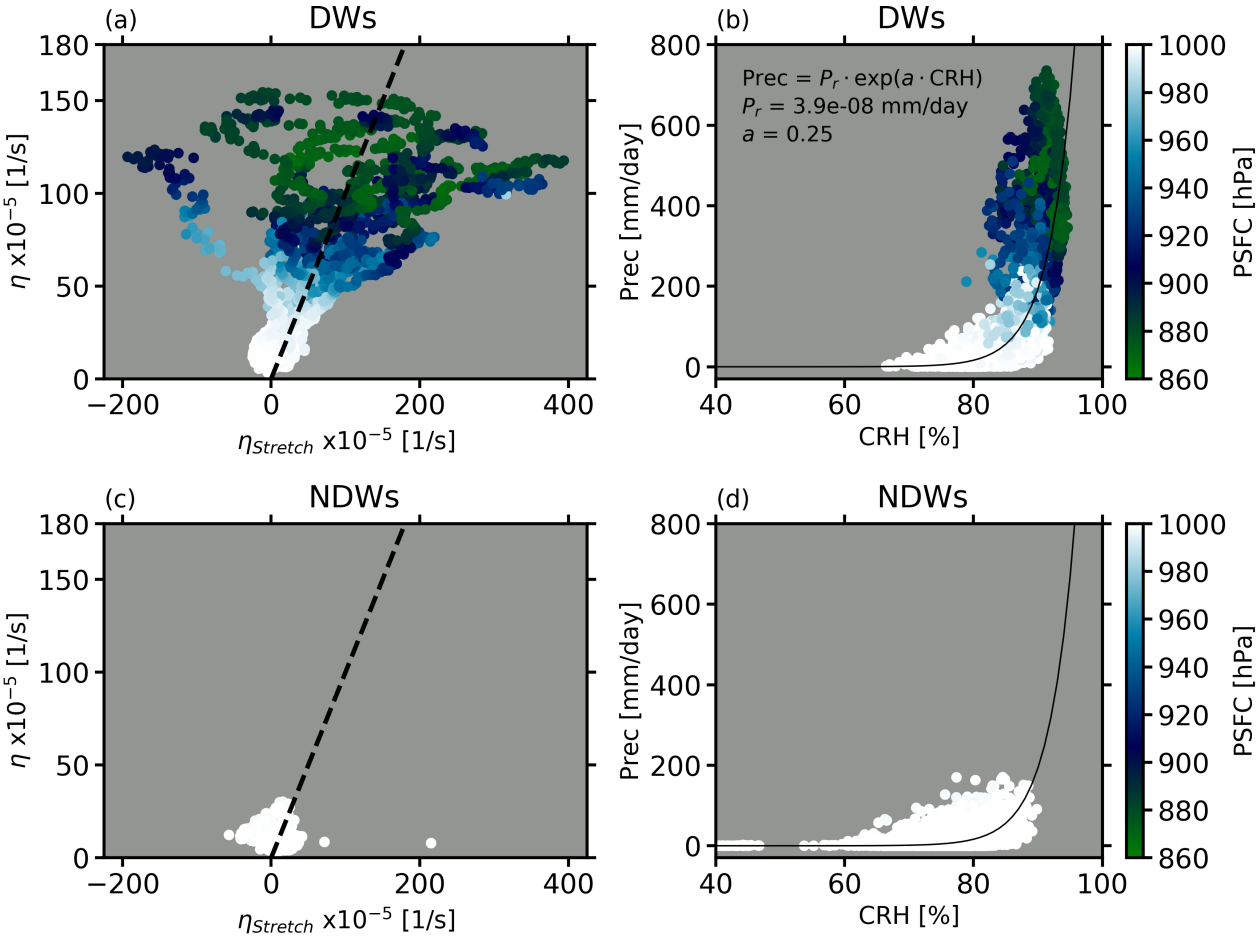

Figure 3.16: Scatterplots of the Developing Waves (DWs) and Non-Developing Waves (NDWs) in all three NGaqua simulations

Scatterplots of all 16 developing waves (DWs) and 35 non-developing waves (NDWs). An ambiguous case is considered a DW if it becomes a TC regardless of what happens to the same waves in the other two simulations. Panels (a) and (c) are scatterplots between the absolute vorticity derived from the generalized stretching tendency ($\eta_{Stretch}$) and the absolute vorticity (η) at 850 hPa. The thick dashed line shows a 1-to-1 relationship between $\eta_{Stretch}$ and η. Colors indicate the central surface pressure (PSFC). Panels (b) and (d) are scatterplots between column relative humidity (CRH) and precipitation (Prec). The thin solid curve is a fitted line of the exponential relationship between CRH and Prec from the DWs. The plotted data are hourly-averaged 160×160-km^2 blocks following the wave disturbances. There are 4,135 samples (hours) in total for the DWs and 5,074 samples for the NDWs.

from TC1 and TC3 simulations, wave W3A from TC3 simulation, and wave W4A from TC1 simulation. Among these, there are a few waves that start out as cyclonic vortices for several days and go through TCG during the end, i.e., waves W2D in all simulations, wave W1A in TC3 simulation, wave W3A in TC3 simulation, and wave W4A in TC1 simulation. All of these waves spin up after Day 15, and for many of them, their counterparts (in the other two simulations) do not become TCs. They are split into both DWs and NDWs; the condition is that after the 850-hPa absolute vorticity increases by 1×10^{-4} 1/s within 48 hours, these waves are considered DWs. The scatterplots of DWs and NDWs are shown in Figure 3.16.

A scatterplot between $\eta_{Stretch}$ and η of all DWs is shown in Figure 3.16a. The colors of the points indicate central surface pressure or PSFC, and the black dashed line shows a 1-to-1 relationship. It shows that the stretching of vorticity can explain the vertical vorticity well during the early stages of the TCs before the vorticity exceeds 50×10^{-5} 1/s (as in Figures 3.7a and 3.11c) or before the PSFC deepens to 980 hPa. Beyond that, the TC expands beyond the 160×160-km^2 block, in which the time series is averaged. The generalized stretching term is also not concentrated at the center of the TC, but rather occurs everywhere even outside the 160×160-km^2 region, as discussed previously. The generalized tilting term has to compensate for the disagreement between η and $\eta_{Stretch}$ as well. Despite that, there still establishes a strong exponential relationship between the column relative humidity (CRH), which is a ratio between the PW and saturated water vapor path, and hourly precipitation (Prec). The exponential relationship is consistent with that in Rushley et al. (2018) and Bretherton et al. (2004) but with different coefficients, as the NGAqua data are hourly while the data used in those papers are daily. The same plots for NDWs are shown in Figures 3.16c and 3.16d. There is neither a 1-to-1 relation between $\eta_{Stretch}$ and η nor an exponential relation between CRH and Prec in NDWs.

We further bin the data by η_{850} over a 160×160-km^2 region every hour following each of the wave systems, and then average them across all of the 17 DW cases and 40 NDW cases. Figure 3.17 shows the box and whisker plots of (a) $\eta_{Stretch}$, (b) PW, (c) Prec and (d) surface LHF binned by η. The η-bin mean CRH and PSFC are also shown in panels

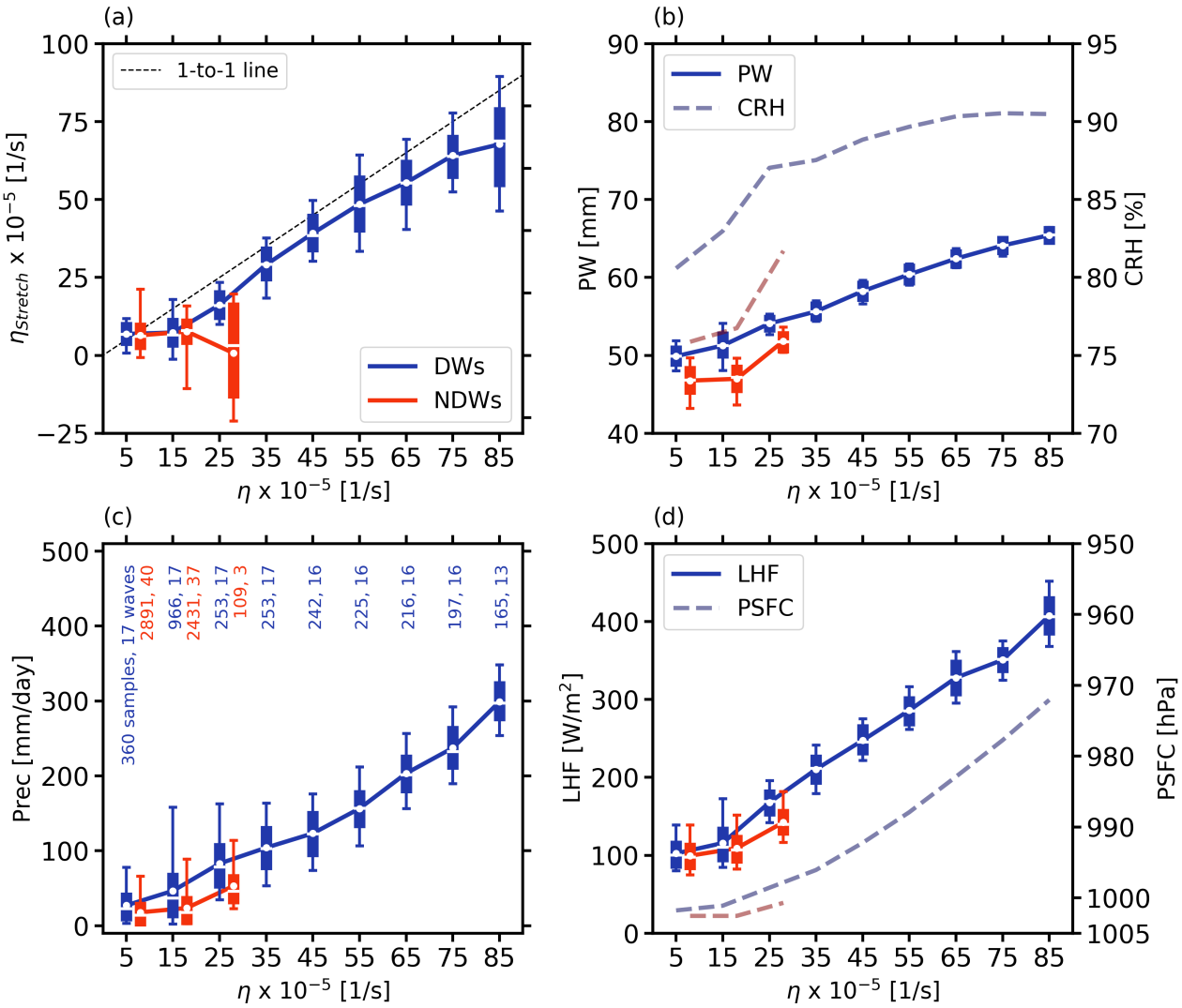

Figure 3.17: Statistics of the DWs and NDWs binned by absolute vorticity at 850 hPa

Box and whisker plots of (a) 850-hPa absolute vorticity derived from the generalized stretching tendency ($\eta_{Stretch}$), (b) precipitable water (PW), (c) surface precipitation (Prec), and (d) surface latent heat flux (LHF) binned by the 850-hPa absolute vorticity (η), hourly averaged over 160×160-km^2 blocks following the vortex systems during the spin-up period. For every η bin, the minimum, 25th percentile, median (white lines), 75th percentile, maximum, and mean (dots) of the fields of interest are averaged within each wave disturbance, and then are averaged again across all the developing waves (DWs) or non-developing waves (NDWs). The numbers of samples (hours) and wave disturbances are shown at the top of Panel (c), and there must be more than one sample within each vorticity bin for the wave to be counted. A thin dashed line in Panel (a) is a 1-to-1 line. For Panels (b) and (d), the means of column relative humidity with respect to water (CRH) and the central surface pressure (PSFC) from all vorticity bins are plotted as thick dashed lines.

(b) and (d) using dashed lines. Figure 3.18 shows the PW composites and the 850-hPa horizontal streamflows of the lower η bins. Figure 3.19 similarly shows the precipitation composites and the generalized stretching tendency at 850 hPa. The highest η bin of the DWs is 150–160$\times 10^{-5}$ 1/s, but we focus on the lower bins in which TCG takes place.

For the DWs, generalized stretching can explain the increase of absolute vorticity at 850-hPa. The vorticity due to generalized stretching also correlates well with the increasing PW, precipitation, and surface LHF. Figure 3.18a-c suggests that during the early stage of cyclogenesis, or the lower-η bins, the cyclonic flow brings high PW air into the center of the system and forms a protective pouch keeping the moist air that is necessary for deep convection to grow, suggestive of a Marsupial paradigm as in Dunkerton et al. (2009) [21]. As the vorticity spins up, the PW keeps increasing while the CRH reaches an asymptote (Figure 3.17b), suggesting that the deep convection has a saturated warm core, hence a lower PSFC (Figure 3.17d). The updraft also generates a secondary circulation that creates a large surface LHF which feedbacks positively to the convection growth. The low-level horizontal convergence associated with the updraft leads to a vertical stretching of the absolute vorticity that further leads to a TC spin-up. This is evident in Figure 3.19a-c, which shows that for the developing cyclones, the low-level vertical stretching of vorticity occurs at the center of the vortex where the precipitation is strongest.

The NDWs go through a different process. Although precipitation, PW and surface LHF all correlate well, and they all increase with the η-bins, the generalized stretching or $\eta_{Stretch}$ does not correlate well with η. Another difference between the DWs and the NDWs is that, the PW and CRH of the NDWs are much lower than those of the DWs. We note that in many cases of the NDWs, the easterly waves remain as large-scale cyclonic vortices with η below 20$\times 10^{-5}$ 1/s. For those in the 20-30$\times 10^{-5}$-1/s η bin, the surface flux feedback still applies. However, Figure 3.18d-e suggests that the vortex center of the NDWs stays at a region of strong PW gradient, which prevents it from developing a moist protected core. Figure 3.19d-e also shows that the positive generalized stretching does not occur at the center of the vorticity maximum. The convective system is slightly more elongated rather

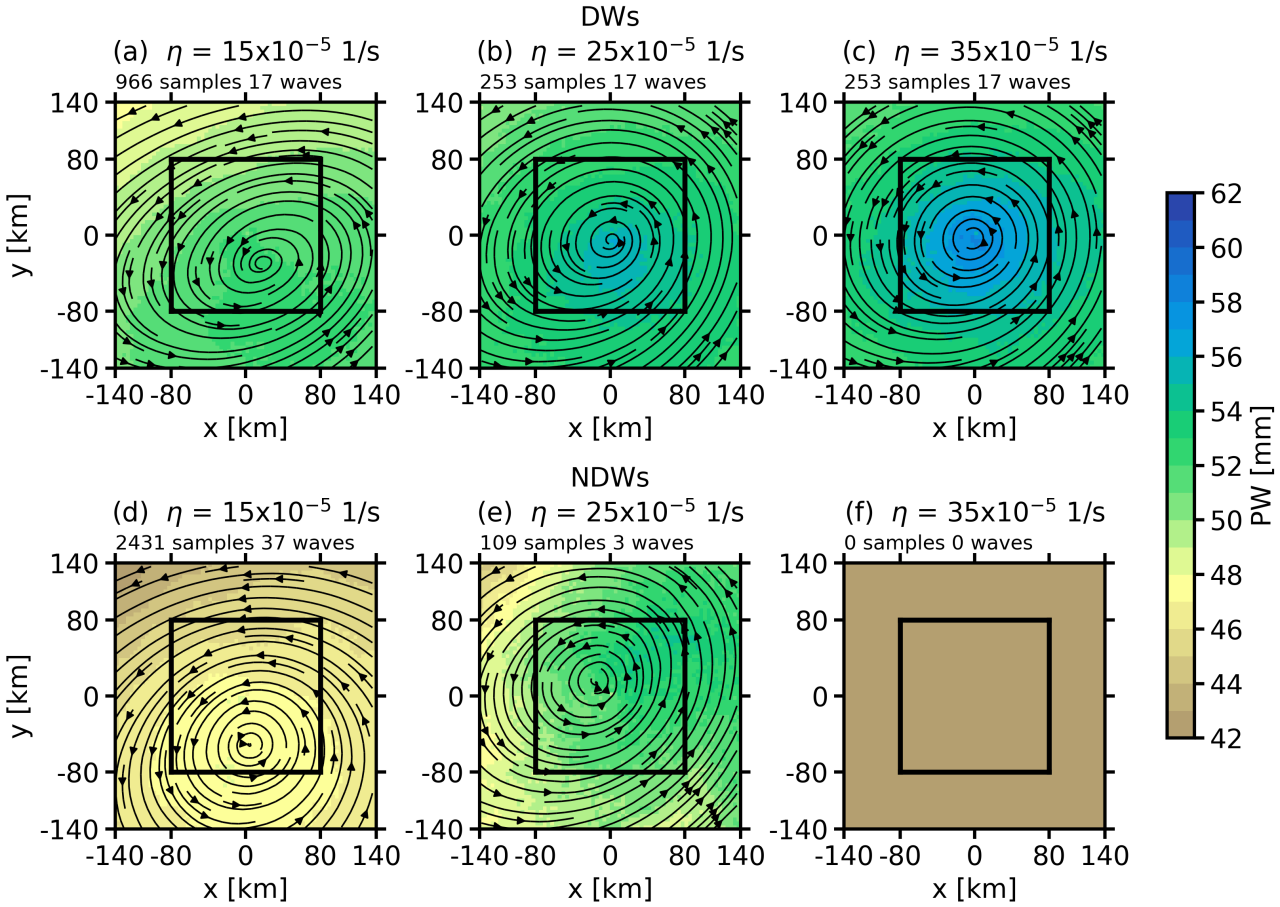

Figure 3.18: Precipitable water composites of the DWs and NDWs overlaid with streamflows at 850 hPa

Composites of hourly precipitable water (PW) binned by hourly-averaged 160×160-km^2 blocks of 850-hPa absolute vorticity (η) following the vortex systems, with the same binning approach as in Figure 6. The composites are from the second to fourth η bins of Figure 6a, i.e. the centers of the η bins are 15, 25, and 35 $\times$ 10^{-5} 1/s. Panels (a)-(c) show the PW composites of the developing waves (DWs), and panels (d)-(f) the non-developing waves (NDWs). The thin black lines with arrows indicate the streamflows of 850-hPa horizontal winds. The thick black lines indicate the 160 km $\times$ 160 km domain.

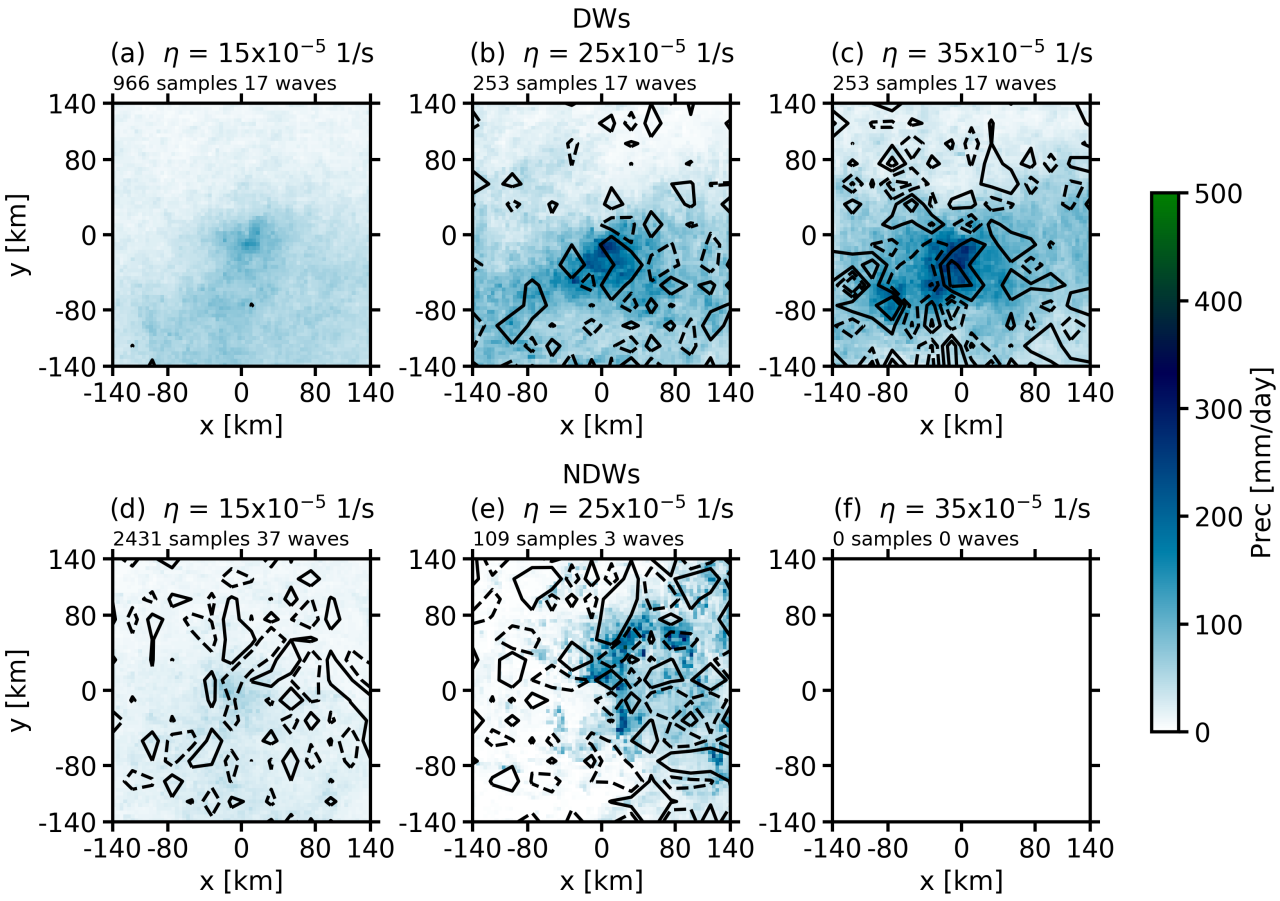

Figure 3.19: Precipitation composites of the DWs and NDWs overlaid with generalized stretching tendency at 850 hPa

Composites of hourly surface precipitation (Prec) binned by 850-hPa absolute vorticity (η) as in Figure 7. The contours in Panels (b)-(c) represent the generalized stretching of absolute vorticity at 850 hPa of the corresponding bins. The solid (dashed) lines indicate positive (negative) generalized stretching tendency at ± 1 and $\pm 3 \times 10^{-8}$ 1/s^2.

than circular, and thus the PSFC remains above 1000 hPa for the NDWs (Figure 3.17d).

3.7 Conclusions

Tropical cyclogenesis is a multiscale process in which convective-scale activities are intertwined with large-scale circulations. We have used near-global aquaplanet cloud-resolving models or NGAqua to examine the process and its predictability. NGAqua is a tropical channel simulation with fixed SST and Coriolis parameters that depend on latitudes. With the SST distribution maximized at 15°N, the off-equatorial ocean surface in NGAqua's northern hemisphere is warm enough for TCs to develop. The TC1, TC2 and TC3 simulations presented in this chapter resemble the East Pacific Ocean in September, when the ITCZ is situated north of the equator. The westerly flow in the ITCZ and northeasterly trade winds in the subtropics provide meridional shear of zonal flows that result in zonal bands of positive vorticity anomalies, regions that are called vorticity filaments. The meridional reversal of absolute vorticity gradient and deep convection in the ITCZ altogether provide a necessary condition for barotropic instability. This means any moist disturbance has a tendency to grow and become deep convection.

TCs in NGAqua spin up spontaneously from the northern edge of the ITCZ. During this process, the ITCZ undulates and breaks down, while the large-scale zonal vorticity anomalies axisymmetrize and become cyclonic vortices. The humidity and deep convection are wrapped around the cyclonic vorticity anomalies. Small-scale processes are then responsible for the TC spin up. As the cyclonically organized vortex moves away from the tropics, the ITCZ returns to its original shape and allows new vorticity filaments to form.

With a 4-km horizontal grid spacing, NGAqua produces realistic tropical convection. Diabatic heating in the deep convection stretches the atmospheric column, resulting in the adjustment of pressure surfaces. Due to hydrostatic balance, low (high) pressure anomalies are obtained below (aloft). The gradient wind balance leads to absolute vorticity spin-up in the lower part of the atmosphere. In a vortex-following framework, we have shown that generalized stretching of absolute vorticity is responsible for most of the absolute vorticity

spin up at 850 hPa during the initial stage of the TC (when η_{850} is below 50 $\times 10^{-5}$ 1/s in NGAqua).

Case studies and the composites of developing TCs have shown that sufficient moisture, i.e., precipitable water, is crucial for deep convective growth, which is indicated by precipitation rates. If vertical stretching of vorticity occurs at the center of the cyclonic vorticity anomaly, the system can grow and develop into a moist-protected warm core that spins up and becomes TCs. The positive surface latent heat flux feedback helps intensify the TCs further. However, if the vortex center is situated over regions of strong precipitable water gradients, dry air can flow into the center of the system, preventing it from growing further. Cyclonic vortices in NGAqua can last for several days even though they do not become TCs.

Based on the analysis of the three ensemble members of NGAqua which initially differ by white-noise humidity perturbations, the predictability of TCG is up to ten days. This is because the pre-TC or cyclonic vortices develop out of vorticity filaments, which are results of large-scale circulation that is more predictable. Convective processes are more random and diverge within a few days' time. However, as long as there is sufficient humidity in a large-scale cyclonic vortex, deep convection can grow and vorticity stretching still leads to TC spin-up.

A few follow-on questions for future studies are the following: what happens if the initial white-noise humidity perturbations are only imposed inside the cyclonic vortex? If the timing of the deep convection differs, this may cause the simulations to diverge sooner than ten days. Additionally, what happens if the initial humidity perturbations are prescribed with the same magnitude but at a larger scale (i.e., 160 km or greater)? This is equivalent to imposing horizontal humidity gradients to the cyclonic vortices in NGAqua. Based on our results, this would hypothetically reduce the predictability of TCG as well.

In addition, what would happen if the SST is allowed to respond to the atmospheric circulations? In particular, on a global average the SST cools down by 0.9°C in response to TC passages, and it takes between 5 and 30 days for the SST to return to its pre-TC temperature [18]. This SST response may help prevent a new formation or intensification of

TCs in the same region for a while. However, because the SST in NGAqua is fixed based on latitudes, new pre-TC vortices have a higher chance to intensify once the undulated ITCZ returns to its original position and a new vorticity filament is formed. Although TCs in NGAqua may occur more frequently than in the real world, the processes which they go through are still realistic and useful for the TCG studies.

Finally, a study of TCG would benefit further from using simulations of a global cloud-resolving model (GCRM) with realistic geography. This is because although TCG in the real world involves multiscale interactions as in NGAqua, it may experience other processes that are not mentioned in this study. For example, in addition to large-scale barotropic instability, baroclinic instability from the meridional temperature gradient over Africa and the monsoon troughs can also lead to easterly waves and cyclonic vortices. One could also add initial humidity perturbations and run an ensemble of GCRM simulations as in NGAqua. If computationally feasible, it would be beneficial to use a larger ensemble of perturbations.

Chapter 4

CONCLUSIONS

In Chapter 2, limited-area cloud-resolving and large-eddy simulations are used to reproduce and understand a negative subtropical shallow cumulus cloud feedback found in near-global aquaplanet simulations. Subtropical low cloud cover change plays a big role in climate feedback. Many state-of-the-art global climate models predict that subtropical low cloud cover will decrease with a warming of SST. However, in a recent study using near-global cloud-resolving models of an aquaplanet, also called NGAqua, subtropical trade cumulus cloud cover increases with 4 K SST warming [39]. NGAqua is based on the System of Atmospheric Modeling or SAM, uses 4-km horizontal grid spacing with latitudinally dependent SST, and is able to produce realistic cloud and circulation in the tropics and subtropics.

In this study, limited-area cloud-resolving and large-eddy simulations based on SAM, or LASAM, are configured to reproduce the trade cumulus cloud cover increase found in NGAqua. LASAM is able to capture the subtropical low cloud fraction increase with SST warming observed in NGAqua, both with the 4-km and 100-m horizontal grid spacing. It broadly supports the hypothesis proposed by Narenpitak et al. (2017) that the enhanced clear-sky BL radiative cooling observed in the +4K SST warming scenario contributes to the increase in subtropical low cloud fraction [39]. The response to the enhanced BL radiative cooling is robust across all model resolution and the choice of advection scheme. A boundary-layer energy budget shows that the downward entrainment heat flux strengthens to balance enhanced radiative cooling, carried by a stronger updraft cloud mass flux from a larger cumulus cloud fraction. In deeper trade cumulus layers, the enhanced radiative cooling in a warming climate may be balanced by increased precipitation warming, leaving the cloud

coverage area almost unchanged. With larger domain sizes, shallow cumulus self-aggregates, especially with higher SST, marginally increasing domain-mean cloud fraction, but this is a secondary contributor to the cloud feedback.

In Chapter 3, we analyze tropical cyclogenesis using NGAqua simulations with fixed latitudinally varying SST maximized at 15°N and latitudinally dependent planetary vorticity. Because of the large domain size and fine resolution, NGAqua provides a realistic global framework and does not rely on any convective parameterizations. Twenty days of simulation outputs show that numerous TCs develop spontaneously north of the Intertropical Convergence Zone or the ITCZ. Large-scale zonal flows and deep convection within the ITCZ altogether provide a necessary condition for barotropic instability. This favors developments of vorticity filaments which tend organize into large-scale cyclonic vortices. The vortices can later become TCs if provided with sufficient humidity that aids the development of small-scale convection.

A new algorithm has been developed to track the initial vortices and TCs. A Lagrangian framework analysis of the 850-hPa vorticity budget confirms that with a pre-existing large-scale cyclonic vortex, the convergence of absolute vorticity in the region of strong updrafts stretches the air column vertically. This contributes positively to the vorticity budget, and helps the vortex spin up to become a TC.

To investigate the predictability of tropical cyclogenesis, two other 20-day simulations are run from the beginning of the equilibrated control simulation. The 700-hPa humidity field is perturbed with 0.1 g kg^{-1} white noise throughout the domain. Results show that the locations and times of TC formations remain similar among all three simulations for over ten days, after which the large-scale winds diverge significantly. The large-scale winds help maintain predictability of the initial vortices. Although the tropical cyclogenesis in all three simulations undergoes the same series of interactions, the small-scale interactions between convection and vorticity occur at different places. Therefore, the exact locations that TCs spin up are not exactly the same even though the locations and characteristics of initial vortices are similar.

BIBLIOGRAPHY

[1] Marja Bister and Kerry A. Emanuel. The genesis of hurricane guillermo: Texmex analyses and a modeling study. *Monthly Weather Review*, 125(10):2662–2682, 1997.

[2] Peter N. Blossey, Christopher S. Bretherton, and Matthew C. Wyant. Subtropical low cloud response to a warmer climate in a superparameterized climate model. part ii: Column modeling with a cloud resolving model. *Journal of Advances in Modeling Earth Systems*, 1(3), 2009.

[3] Peter N. Blossey, Christopher S. Bretherton, Minghua Zhang, Anning Cheng, Satoshi Endo, Thijs Heus, Yangang Liu, Adrian P. Lock, Stephan R. De Roode, and Kuan Man Xu. Marine low cloud sensitivity to an idealized climate change: The CGILS les intercomparison. *Journal of Advances in Modeling Earth Systems*, 5(2):234–258, 2013.

[4] Sandrine Bony and Jean Louis Dufresne. Marine boundary layer clouds at the heart of tropical cloud feedback uncertainties in climate models. *Geophysical Research Letters*, 32(20):1–4, 2005.

[5] O. Boucher, D. Randall, P. Artaxo, C. Bretherton, G. Feingold, P. Forster, V.-M. Kerminen, Y. Kondo, H. Liao, U. Lohmann, P. Rasch, S. K. Satheesh, S. Sherwood, B. Stevens, and X. Y. Zhang. *Clouds and aerosols*, pages 571–657. Cambridge University Press, Cambridge, UK, 2013.

[6] Christopher S. Bretherton, Philli Austin, and Steven T. Siems. Cloudiness and marine boundary layer dynamics in the ASTEX Lagrangian experiments. Part II: cloudiness, drizzle, surface fluxes, and entrainment. *Journal of the Atmospheric Sciences*, 52(16):2724–2735, 1995.

[7] Christopher S. Bretherton and Peter N. Blossey. Low cloud reduction in a greenhouse-warmed climate: Results from Lagrangian les of a subtropical marine cloudiness transition. *Journal of Advances in Modeling Earth Systems*, 6(1):91–114, 2014.

[8] Christopher S. Bretherton and Peter N. Blossey. Understanding Mesoscale Aggregation of Shallow Cumulus Convection Using Large-Eddy Simulation. *Journal of Advances in Modeling Earth Systems*, 9(8):2798–2821, 2017.

[9] Christopher S. Bretherton, Peter N. Blossey, and Christopher R. Jones. Mechanisms of marine low cloud sensitivity to idealized climate perturbations: A single-LES exploration extending the CGILS cases. *Journal of Advances in Modeling Earth Systems*, 5(2):316–337, 2013.

[10] Christopher S. Bretherton, Peter N. Blossey, and Marat Khairoutdinov. An Energy-Balance Analysis of Deep Convective Self-Aggregation above Uniform SST. *Journal of the Atmospheric Sciences*, 62(12):4273–4292, 2005.

[11] Christopher S. Bretherton and Marat F. Khairoutdinov. Convective self-aggregation feedbacks in near-global cloud-resolving simulations of an aquaplanet. *Journal of Advances in Modeling Earth Systems*, 7(4):1–23, 2015.

[12] Christopher S. Bretherton, Matthew E. Peters, and Larissa E. Back. Relationships between water vapor path and precipitation over the tropical oceans. *Journal of Climate*, 17(7):1517–1528, 2004.

[13] Christopher S Bretherton, Martin Widmann, Valentin P Dymnikov, John M Wallace, and Ileana Blade. Effective number of degrees of freedom of a spatial field. *Journal of Climate*, 12(1969):1990–2009, 1999.

[14] Francis. P. Bretherton. Critical layer instability in baroclinic flows. *Quarterly Journal of the Royal Meteorological Society*, 92(393):325–334, 1966.

[15] Florent Brient, Tapio Schneider, Zhihong Tan, Sandrine Bony, Xin Qu, and Alex Hall. Shallowness of tropical low clouds as a predictor of climate models' response to warming. *Climate Dynamics*, 47(1-2):433–449, 2016.

[16] Shuyi S. Chen and William M. Frank. A numerical study of the genesis of extratropical convective mesovortices. part i: Evolution and dynamics. *Journal of the Atmospheric Sciences*, 50(15):2401–2426, 1993.

[17] William D. Collins, Philip J. Rasch, Byron A. Boville, James J. Hack, James R. McCaa, David L. Williamson, Bruce P. Briegleb, Cecilia M. Bitz, Shian Jiann Lin, and Minghua Zhang. The formulation and atmospheric simulation of the Community Atmosphere Model version 3 (CAM3). *Journal of Climate*, 19(11):2144–2161, 2006.

[18] Richard A. Dare and John L. McBride. Sea surface temperature response to tropical cyclones. *Monthly Weather Review*, 139(12):3798–3808, December 2011.

[19] Christopher A. Davis. The formation of moist vortices and tropical cyclones in idealized simulations. *Journal of the Atmospheric Sciences*, 72(9):3499–3516, 2015.

[20] Simon P. de Szoeke, Shang-Ping Xie, Toru Miyama, Kelvin J. Richards, and R. Justin O. Small. What maintains the sst front north of the eastern pacific equatorial cold tongue? *Journal of Climate*, 20(11):2500–2514, 2007.

[21] Timothy J. Dunkerton, Michael T. Montgomery, and Zhuo Wang. Tropical cyclogenesis in a tropical wave critical layer: Easterly waves. *Atmospheric Chemistry and Physics*, 9(15):5587–5646, 2009.

[22] Ryan Eastman and Robert Wood. The Competing Effects of Stability and Humidity on Subtropical Stratocumulus Entrainment and Cloud Evolution from a Lagrangian Perspective. *Journal of the Atmospheric Sciences*, 75(8):2563–2578, 2018.

[23] Rosana Nieto Ferreira and Wayne H. Schubert. Barotropic aspects of itcz breakdown. *Journal of the Atmospheric Sciences*, 54(2):261–285, 1997.

[24] Hironori Fudeyasu, Yuqing Wang, Masaki Satoh, Tomoe Nasuno, Hiroaki Miura, and Wataru Yanase. Global cloud-system-resolving model nicam successfully simulated the lifecycles of two real tropical cyclones. *Geophysical Research Letters*, 35(22), 2008.

[25] Saska Gjorgjievska and David J. Raymond. Interaction between dynamics and thermodynamics during tropical cyclogenesis. *Atmospheric Chemistry and Physics*, 14(6):3065–3082, 2014.

[26] William M. Gray. Global view of the origin of tropical disturbances and storms. *Monthly Weather Review*, 96(10):669–700, 1968.

[27] William M. Gray. *Hurricanes: Their formation, structure and likely role in the tropical circulation.* Royal Meteorological Society, James Glaisher House, Grenville Place, Bracknell, Berkshire, RG12 1BX, 1979.

[28] Peter H. Haynes and Michael E. McIntyre. On the evolution of vorticity and potential vorticity in the presence of diabatic heating and frictional or other forces. *Journal of the Atmospheric Sciences*, 44(5):828–841, 1987.

[29] Eric A. Hendricks, Michael T. Montgomery, and Christopher A. Davis. The role of "vortical" hot towers in the formation of tropical cyclone diana (1984). *Journal of the Atmospheric Sciences*, 61(11):1209–1232, 2004.

[30] Marat F. Khairoutdinov and David a. Randall. Cloud Resolving Modeling of the ARM Summer 1997 IOP: Model Formulation, Results, Uncertainties, and Sensitivities. *Journal of the Atmospheric Sciences*, 60(4):607–625, 2003.

[31] Stephen A. Klein. Synoptic variability of low-cloud properties and meteorological parameters in the subtropical trade wind boundary layer. *Journal of Climate*, 10(8):2018–2039, 1997.

[32] Stephen A. Klein, Dennis L. Hartmann, and Joel R. Norris. On the relationships among low-cloud structure, sea surface temperature, and atmospheric circulation in the summertime northeast Pacific. *Journal of Climate*, 8(5):1140–1155, 1995.

[33] Kenneth D. Leppert, Daniel J. Cecil, and Walter A. Petersen. Relation between tropical easterly waves, convection, and tropical cyclogenesis: A lagrangian perspective. *Monthly Weather Review*, 141(8):2649–2668, 2013.

[34] Brian Medeiros, Bjorn Stevens, and Sandrine Bony. Using aquaplanets to understand the robust responses of comprehensive climate models to forcing. *Climate Dynamics*, 44(7-8):1957–1977, 2015.

[35] Hiroaki Miura, Hirofumi Tomita, Tomoe Nasuno, Shin-ichi Iga, Masaki Satoh, and Taroh Matsuno. A climate sensitivity test using a global cloud resolving model under an aqua planet condition. *Geophysical Research Letters*, 32(19), 2005.

[36] Michael T. Montgomery, M. E. Nicholls, Thomas A. Cram, and A. B. Saunders. A vortical hot tower route to tropical cyclogenesis. *Journal of the Atmospheric Sciences*, 63(1):355–386, 2006.

[37] Caroline J. Muller and David M. Romps. Acceleration of tropical cyclogenesis by self-aggregation feedbacks. *Proceedings of the National Academy of Sciences*, 115(12):2930–2935, 2018.

[38] Pornampai Narenpitak and Christopher S. Bretherton. Understanding negative subtropical shallow cumulus cloud feedbacks in a near-global aquaplanet model using limited area cloud-resolving simulations. *Journal of Advances in Modeling Earth Systems*, 11(6):1600–1626, 2019.

[39] Pornampai Narenpitak, Christopher S. Bretherton, and Marat F. Khairoutdinov. Cloud and circulation feedbacks in a near-global aquaplanet cloud-resolving model. *Journal of Advances in Modeling Earth Systems*, 9(2):1069–1090, 2017.

[40] R B Neale and B J Hoskins. A standard test for AGCMs including their physical parametrizations: I: The proposal. *Atmospheric Science Letters*, 1(2):101–107, 2000.

[41] David S Nolan. Evaluating environmental favorableness for tropical cyclone development with the method of point-downscaling. *Journal of Advances in Modeling Earth Systems*, 3(3), 2011.

[42] Garth W. Paltridge. Cloud-radiation feedback to climate. *Quarterly Journal of the Royal Meteorological Society*, 106(450):895–899, 1980.

[43] Hossein Parishani, Michael S. Pritchard, Christopher S. Bretherton, Christopher R. Terai, Matthew C. Wyant, Marat Khairoutdinov, and Balwinder Singh. Insensitivity of the cloud response to surface warming under radical changes to boundary layer turbulence and cloud microphysics: Results from the ultraparameterized cam. *Journal of Advances in Modeling Earth Systems*, 10(12):3139–3158, 2018.

[44] Hossein Parishani, Michael S. Pritchard, Christopher S. Bretherton, Matthew C. Wyant, and Marat Khairoutdinov. Toward low-cloud-permitting cloud superparameterization with explicit boundary layer turbulence. *Journal of Advances in Modeling Earth Systems*, 9(3):1542–1571, 2017.

[45] David Raymond, Zeljka Fuchs, Saska Gjorgjievska, and Sharon Sessions. Balanced dynamics and convection in the tropical troposphere. *Journal of Advances in Modeling Earth Systems*, 7(3):1093–1116, 2015.

[46] David J. Raymond and Lopez C. Carrillo. The vorticity budget of developing typhoon nuri. *Atmospheric Chemistry and Physics*, 11(1):147–163, 2008.

[47] Malte Rieck, Louise Nuijens, and Bjorn Stevens. Marine Boundary Layer Cloud Feedbacks in a Constant Relative Humidity Atmosphere. *Journal of the Atmospheric Sciences*, 69(8):2538–2550, 2012.

[48] Axel Seifert and Thijs Heus. Large-eddy simulation of organized precipitating trade wind cumulus clouds. *Atmospheric Chemistry and Physics*, 13(11):5631–5645, 2013.

[49] Pier Siebesma, Christopher S. Bretherton, Andrew Brown, Andreas Chlond, Joan Cuxart, Peter G. Duynkerke, Hongli Jiang, Marat Khairoutdinov, David Lewellen, Chin-Hoh Moeng, Enrique Sanchez, Bjorn Stevens, and David E. Stevens. A Large Eddy Simulation Intercomparison Study of Shallow Cumulus Convection. *Journal of the Atmospheric Sciences*, 60(10):1201–1219, 2003.

[50] Piotr K. Smolarkiewicz and Wojciech W. Grabowski. The multidimensional positive definite advection transport algorithm: nonoscillatory option. *Journal of Computational Physics*, 86(2):355–375, 1990.

[51] Richard. C. J. Somerville and Lorraine A. Remer. Cloud optical thickness feedbacks in the CO2 climate problem. *Advances in Space Research*, 5(6):209–212, 1985.

[52] Hirofumi Tomita, Hiroaki Miura, Shin-ichi Iga, Tomoe Nasuno, and Masaki Satoh. A global cloud-resolving simulation: Preliminary results from an aqua planet experiment. *Geophysical Research Letters*, 32(8), 2005.

[53] Bryce Tyner and Anantha Aiyyer. Evolution of african easterly waves in potential vorticity fields. *Monthly Weather Review*, 140(11):3634–3652, 2012.

[54] Nguyen Van Sang, Roger K. Smith, and Michael T. Montgomery. Tropical-cyclone intensification and predictability in three dimensions. *Quarterly Journal of the Royal Meteorological Society*, 134(632):563–582, 2008.

[55] Jessica Vial, Sandrine Bony, Bjorn Stevens, and Raphaela Vogel. Mechanisms and Model Diversity of Trade-Wind Shallow Cumulus Cloud Feedbacks: A Review. *Surveys in Geophysics*, 38(6):1331–1353, 2017.

[56] Raphaela Vogel, Louise Nuijens, and Bjorn Stevens. The role of precipitation and spatial organization in the response of trade-wind clouds to warming. *Journal of Advances in Modeling Earth Systems*, 8(2):843–862, 2016.

[57] J. Warner. The water content of cumuliform cloud. *Tellus*, 7(4):449–457, 1955.

[58] Allison A. Wing, Suzana J. Camargo, and Adam H. Sobel. Role of radiative–convective feedbacks in spontaneous tropical cyclogenesis in idealized numerical simulations. *Journal of the Atmospheric Sciences*, 73(7):2633–2642, 2016.

[59] Allison A. Wing, Kerry Emanuel, Christopher E. Holloway, and Caroline Muller. Convective Self-Aggregation in Numerical Simulations: A Review. *Surveys in Geophysics*, 38(6):1173–1197, 2017.

[60] Allison A. Wing, Kerry Emanuel, Christopher E. Holloway, and Caroline Muller. Convective Self-Aggregation in Numerical Simulations: A Review. *Surveys in Geophysics*, 38(6):1173–1197, 2017.

[61] Robert Wood and Christopher S. Bretherton. On the relationship between stratiform low cloud cover and lower-tropospheric stability. *Journal of Climate*, 19(24):6425–6432, 2006.

[62] Matthew C. Wyant, Christopher S. Bretherton, and Peter N. Blossey. Subtropical Low Cloud Response to a Warmer Climate in a Superparameterized Climate Model. Part I: Regime Sorting and Physical Mechanisms. *Journal of Advances in Modeling Earth Systems*, 1(3):7, 2009.

[63] Takanobu Yamaguchi, David A. Randall, and Marat F. Khairoutdinov. Cloud Modeling Tests of the ULTIMATE–MACHO Scalar Advection Scheme. *Monthly Weather Review*, 139(10):3248–3264, 2011.

[64] Mark D. Zelinka, Stephen A. Klein, Karl E. Taylor, Timothy Andrews, Mark J. Webb, Jonathan M. Gregory, and Piers M. Forster. Contributions of different cloud types

to feedbacks and rapid adjustments in CMIP5. *Journal of Climate*, 26(14):5007–5027, 2013.

[65] Mark D. Zelinka, Chen Zhou, and Stephen A. Klein. Insights from a refined decomposition of cloud feedbacks. *Geophysical Research Letters*, 43(17):9259–9269, 2016.

Appendix A

SUPPLEMENTARY VIDEOS

Below are descriptions of the supplementary videos, which can be found on the University of Washington ResearchWorks Archive for Dissertations and Theses.

Video S1 Hourly snapshots of precipitable water (PW) and absolute vorticity at 850 hPa (η_{850}) from NGAqua TC1 simulation, during the next 20 days after the simulation has equilibrated. The PW field is at 4-km horizontal resolution, which is the original resolution of NGAqua. The η_{850} field is coarse-averaged to 40-km horizontal resolution to reduce the noise.

Video S2 Hourly snapshots of η_{850} from NGAqua TC1, TC2, and TC3 simulations, focused between 0° and 30°N, where vorticity filaments organize and TCs spin up. The η_{850} field is coarse-averaged to 20-km horizontal resolution.